Title
Alternative Feedstock for Sustainable Metal Additive Manufacturing: from Powder to Builds

Author
Kiani, Parnian

Publication Date
2020

UNIVERSITY OF CALIFORNIA,
IRVINE

Alternative Feedstock for Sustainable Metal Additive Manufacturing: from Powder to Builds

DISSERTATION

submitted in partial satisfaction of the requirements
for the degree of

DOCTOR OF PHILOSOPHY

in Materials Science and Engineering

by

Parnian Kiani

Dissertation Committee:
Professor Julie M. Schoenung, Chair
Professor Lorenzo Valdevit
Associate Professor Timothy Rupert

2020

DEDICATION

Lovingly dedicated to

my wonderful husband, Matin, for his endless love, support, and patience,
my loving parents Fariba and Majid for their unconditional love, support, and encouragement throughout my life,
and my kind sister, Pardis, who has always had my back in life

TABLE OF CONTENTS

Page

LIST OF FIGURES

Page

LIST OF TABLES

Page

ACKNOWLEDGEMENTS

I would like to express my deepest appreciation to my advisor, Professor Julie M. Schoenung, for giving me the opportunity to be part of her research group. I met Professor Schoenung when she just moved back to Irvine, and I was a master’s student, and I was fortunate that our paths have crossed. She has mentored me not only in research but also in life. She showed me how to be a humble boss, a great researcher, and a considerate colleague. Her insight and guidance were always clear and well-considered. During the ups and downs of my Ph.D. life, I always knew that she finds a way to help and support me, either with a great plan or with the most heartwarming words.

I would like to thank my committee members, Professor Lorenzo Valdevit and Professor Timothy Rupert, whose work and appreciation in Materials Science and Engineering field have been inspiring for me throughout my Ph.D. life.

I owe Darryl Mack so much for his great work in the lab. When I started my Ph.D. in 2015, we did not have an equipped lab space yet, and throughout the years, I saw how hard he worked to provide a safe and functioning lab for us. I have learned so much from him, and I greatly appreciate how he always was ready to make another research idea into reality.

I would also like to thank my co-advisor and mentor, Professor Kaka Ma. Although she left our group for her new job at the Colorado State University early in my journey, I was always grateful for her mentorship in those months, her insight in my work, and her friendship.

During the last five years, I have been incredibly lucky to have the opportunity and privilege of working with a great team of researchers that I am fortunate to call them my friends. I would like to thank Dr. James Haley for his patience and guidance during my struggles with

LENS. I would like to thank our intelligent, caring, and hard-working postdoctoral scholar, Dr. Alexander Dupuy, for his patience, guidance, and insight in my work. I have also learned a lot from my dear lab mates, Dr. Umberto Scipioni Bertoli, Kathrine Acord, Kathrine Terrassa, and Benjamin MacDonald. They have played a significant role in making me the researcher and the team-player that I am today. My amazing friends at UCI made the Ph.D. journey not only very productive but also very fun; their friendship is one of the highlights of my time. I am looking forward to many more years of friendship and hopefully making many more memories together. I would also like to thank other members of our excellent research group, Dr. Baolong Zhou, Dr. Thale Smith, Dr. Xin Wang, Aleksandra Vyatskikh, and many others. I cannot even begin to thank you enough for your time and companionship.

I had the chance to work with different undergraduate researchers that were passionate about research. I have learned a lot from them. I want to thank Jessica Bui and Inkiad Ahmed for their help in data collection and analysis of some of my primary work on milling the waste materials and reusability of Al powder in LENS®. I specially want to thank Al Jonathan Medrano for his help in data collection for the powder reusability project.

I was lucky to see the birth of our Materials Science and Engineering department, and I saw how much work went into making our department grow. I appreciate the great leadership at the department provided by Prof. Schoenung and our fantastic staff, especially Amy Ricks. I wish them success and hope our department continues to flourish as it has been in the last few years. I would also like to express my appreciation to Ephie Bakou for not just having all the answers but also for her friendship.

Most importantly, I would like to thank my family for their unconditional love, support, and kindness. My parents support made this journey possible, and I am so thankful for all their

sacrifices throughout these years. Deciding to continue my education in the U.S. was not an easy decision and if it was not for my wonderful family, I would not be able to even start this journey. I hope to see them again soon. Since the day I met my sister, I knew I found my best friend. She always has her own unique way to inspire me and help me to be strong. I would also like to thank my wonderful cousins and amazing in-laws who encouraged and supported me throughout this journey. Last but not least, I would like to thank my best friend, my soulmate, and my husband; Matin. We met when we were both freshmen in college and not a single day has passed without me feeling the luckiest woman on earth. He has always been a great source of encouragement for me and I would not be here today if it wasn't for him. He always has my back and inspires me. Thank you.

I would like to acknowledge the financial support provided by the National Science Foundation (NSF) through grant CBET-1605392. I also thank the Broadcom Foundation for their support through "UCI Engineering Graduate Fellowship Program" that supported me for two years. In addition, I would like to thank UCI Henry Samueli School of Engineering for their fellowship program supporting student switching from masters' program to Ph.D. I would also like to acknowledge the Henry Samueli School of Engineering and the helpful staff at IMRI that facilitate our research activities. In addition, I would like to thank Morf3D Aerospace Company for generously providing the waste support structure for my sustainability project and Professor Ogunseitan for generously allowing me to use the cutting mill in his lab.

CURRICULUM VITAE

Parnian Kiani

Department of Materials Science and Engineering

University of California, Irvine

EDUCATION

Ph.D., Materials Science and Engineering Sep.2020
M.S., Materials Science and Engineering 2018
University of California, Irvine
B.Sc., Materials Science and Engineering (Specialization: Ceramic Engineering) 2014
Iran University of Science and Technology

EXPERIENCE

Teaching Assistant, University of California, Irvine Su.- 2020
Evaluate students work for the Mechanical behavior and principal design course

Graduate Research Assistant, University of California, Irvine Sep. 2015-Present
Advisor: Prof. Julie, M. Schoenung

- Worked on deposition of AlSi10Mg single tracks and blocks using directed energy deposition
- Conducted research on the mechanical and microstructural properties of AlSi10Mg AM samples
- Worked on understanding the relationship between powder reuse and final part properties in AM
- Designed novel feedstock from machine chips and scraps for AM
- Conducted research on relationship between powder characteristic and flowability

Teaching Assistant, University of California, Irvine

- Evaluated student work for Green Engineering course F- 2017
- Evalate student work for C language for Software Engineering course W- 2016

Research Assistant, Iran University of Science and Technology (Tehran- Iran) 2012-2014
Advisors: Prof. Farhad Golestani Fard

- Developed the methodology to prepare porous monolithic carbon aerogel by sol-gel processing
- Conducted research on using Carbon Nanotubes as drug delivery vehicles

Inspection Intern, 2R inspection and quality services (Tehran-Iran) Su. 2013

- Implemented the international standards (ASTM, ISO, DIN) to be used by different clients

PEER-REVIEWED PUBLICATIONS

- Kiani, P., et. al., Fabrication and microstructure evolution of aluminum matrix composites processed in powder bed fusion**. (In progress).**
- Kiani, P., Dupuy, A.D., Ma, K. and Schoenung, J.M., 2020. *Directed energy deposition of AlSi10Mg: Single track nonscalability and bulk properties.* Materials & Design, p.108847.
- Kiani, P., Scipioni Bertoli, U., Dupuy, A.D., Ma, K. and Schoenung, J.M., *A Statistical Analysis of Powder Flowability in Metal Additive Manufacturing*. Advanced Engineering Materials.

- Fullenwider, B., Kiani, P., Schoenung, J.M. and Ma, K., 2019. *Two-stage ball milling of recycled machining chips to create an alternative feedstock powder for metal additive manufacturing*. Powder technology, 342, pp.562-571.
- Karimi, M., Solati, N., Amiri, M., Mirshekari, H., Mohamed, E., Taheri, M., Hashemkhani, M., Saeidi, A., Estiar, M.A., Kiani, P. et. al., 2015. Carbon nanotubes part I: preparation of a novel and versatile drug-delivery vehicle. Expert Opin. Drug Deliv, 12(7), pp.1071-1087.
- Karimi, M., Solati, N., Ghasemi, A., Estiar, M.A., Hashemkhani, M., Kiani, P., et al., 2015. Carbon nanotubes part II: a remarkable carrier for drug and gene delivery. Expert Opin. Drug Deliv, 12(7), pp.1089-1105.

CONFERENCE PUBLICATION

- Fullenwider, B., Kiani, P., Schoenung, J.M. and Ma, K., 2019. *From Recycled Machining Waste to Useful Powders for Metal Additive Manufacturing*. REWAS 2019 (pp. 3-7). Springer, Cham.
- Kiani, P., Fard, F.G., 2015. *Synthesis of meso porous carbon monolithic via ambient drying*. Glob. J. Adv. Pure & Appl. Sci., 6(0).

CONFERENCE PRESENTATIONS (Presenting author underlined)

- **Kiani, P.**, Dupuy, A.D., Ma, K., Schoenung, J.M., *Directed Energy Deposition of AlSi10Mg: Single Track Non-scalability and Bulk Properties*, 149th annual TMS meeting 2020. **(Oral Presentation)**
- **Kiani, P.**, Scipioni Bertoli, U., Dupuy, A.D., Ma, K., Schoenung, J.M., *Powder Flowability Measurements: Statistical Correlations Between Powder Characteristics and Flowability Behavior*, 149th annual TMS meeting 2020. **(Poster Presentation)**
- **Kiani. P**., Ma, K., Schoenung, J.M., *Parametric Study on Directed Energy Deposition of Aluminum Alloys*, 147th annual TMS meeting 2018. **(Oral Presentation)**
- **Kiani, P.**, Bui, J., Ma, K., Schoenung, J.M., *Ball Milling of Metal Scrap as an Alternative Feedstock for Additive Manufacturing,* 147th annual TMS meeting 2018. **(Poster Presentation)**
- **Kiani, P**., Ma, K., Schoenung, J.M., *Investigating the Influence of Powder Morphology on Metal Additive Manufactured Parts*, Annual AMPM meeting 2017. **(Oral Presentation)**
- **Kiani, P.,** Ma, K., Schoenung, J.M., *Investigating the Use of Recycled Machining Waste as an Alternative Feedstock for Metal Additive Manufacturing*, 146th annual TMS meeting 2017. (Oral Presentation)

TECHNICAL and COMPUTATIONAL SKILLS

Characterization Techniques: Microscopy (Expert in SEM (BSE and EDS), OM, Experienced in EBSD, FIB, and TEM (TEM, BF, HAADF, Diffraction Pattern)), competent in XRD, Experienced in XPS/ESCA and powder flowability analysis (Hall method, FT4, and Revolution)

Mechanical Testing: Competent in tensile, microhardness, and compression tests, Experienced in 3-point and 4-point bending and nanoindentation

Materials Processing Techniques: Expert in using metal powder fed AM systems (LENS), Experienced in powder bed AM systems (SLM), Competent in Cryomilling, Ball milling, Wire EDM, Band saw blade, and Wet saw, and Experienced in Lathe, Endmill, Ion-milling, and Heat treatment

Programming: Working knowledge with MATLAB, C++, HTML, JavaScript, and CSS

Applications: Working knowledge with ImageJ, COMSOL, Gulp, CrystalMaker, OnShape, and SketchUp

CERTIFICATES and PROFESSIONAL ACTIVITIES

Certificates by UCI: Course Design in Teaching, Improv in Teaching, Excellence in Engineering Communication, Public Speaking, Communication Skills for Academics	2018-present
Manuscript reviewer for: Journal of Materials Science and Engineering A, Journal of Metallurgical and Materials Transactions A, Journal of Sustainable Metallurgy, Journal of The Minerals, Metals & Materials Society (JOM)	2016-present

HONORS

• Co-Recipient of TMS light metals/extraction & processing subject award-Recycling	Nov. 2019
• UCI Engineering Graduate Fellowship Program Sponsored by Broadcom Foundation	2018, 2019
• Ph.D. Bridge Fellowship Award by UCI for students converting from masters to Ph.D.	Fall 2017
• NSF (National Science Foundation) travel grant for POWDERMT 2017 Conference	June 2017

OUTREACH and MENTORSHIP ACTIVITIES

• **STEM panel for college students interested in graduate programs** (Orange County College)	Nov. 2019
• **STEM workshops for high school students in underrepresented regions** (Rancho Santa Margarita Public library)	2018-2019
• **International Officer at Materials Science and Engineering Graduate Student Association (GSA)** (University of California, Irvine)	2019
• **Mentored undergraduate and graduate students in research: Jessica Bui, Inkiad Ahmed, Al Jonathan Medrano, Nithya Ramesh** (University of California, Irvine)	2015-2019

ABSTRACT OF THE DISSERTATION

Alternative Feedstock for Sustainable Metal Additive Manufacturing: from Powder to Builds

by

Parnian Kiani

Doctor of Philosophy in Materials Science and Engineering

University of California, Irvine, 2020

Professor Julie M. Schoenung, Chair

Interest in additive manufacturing (AM) has grown exponentially in recent decades and is now being used in many different industries, such as the aerospace, automotive, and biomedical device industries. Unfortunately, the high cost of feedstock powder material, the need for high energy lasers, and a low rate of production have limited the use of this powerful technique on a large scale. Among all the parameters that are crucial in the quality of the parts, the relationship between starting feedstock powder and the quality of the part is not well explored. The common feedstock used in AM, gas atomized powder, requires a high amount of energy and inert gas to be produced. Therefore, gas atomized powder production is costly and not environmentally desirable. AM is believed to produce lower waste compared to the conventional manufacturing process due to minimal required post-processing; however, unless more sustainable starting materials and continuous powder reuse are implemented, the process is very wasteful. The primary focus of this dissertation is on understanding the role of the starting powder on the AM process sustainability in addition to the properties of additively manufactured parts. Powder size and morphology strongly influence powder flow and powder packing density, both of which are critical to successful AM processing. Therefore, the relationship between powder morphological features and flowability was explored and concluded that flowability of powders are heavily influenced by the particles size and shape. In order to reduce the amount of waste produced in laser directed energy deposition (L-DED) process, gas atomized powder was reused, and the reused powders and manufactured parts were characterized. The results indicate that although particles undergo severe changes as they are being reused in AM, the mechanical properties of the manufactured parts show minimal changes.

The production of powder from waste material for AM was explored. High energy milling and cryomilling were employed to recycle waste materials to be used as a starting material in AM. The results show that the size and morphology of the produced powder are significantly influenced by the production method, which was modified by tailoring the processing parameters. In addition, the feasibility of depositing aluminum matrix composites has been investigated as a way to improve the mechanical properties of parts manufactured with milled powder. The composite single tracks deposited in L-DED showed comparable morphologies to the single tracks deposited with gas atomized powder. Understanding the effects of using milled powder prepared as composite or recycled powder on the mechanical and microstructural properties of AM parts will be investigated in future work.

Chapter 1: Introduction to Additive Manufacturing and Powder Processing Techniques

1.1. Additive Manufacturing

Additive manufacturing (AM), which is one of the great innovations of the 20th century, uses a computer aided design (CAD) model to fabricate 3D parts in a layer-by-layer manner. AM is used in many industries and has been developed and modified to process a wide range of materials, from polymers to metals and ceramics. Metal AM has attracted a lot of attention in the past couple of decades due to the ability to deposit complicated geometries [1]. Conventional manufacturing (forging, molding, casting, etc.) faces limitations in fabricating complex geometries. Traditionally, manufacturing complicated geometries required assembling different parts with extensive and time-consuming post-processing machining steps; however, AM is able to fabricate complicated parts with almost no post-processing steps required [1]. In addition, the need for expensive tools such as dies and molds is minimized in AM. As can be seen in Figure 1.1, AM is capable of manufacturing one uniform part whereas conventional manufacturing requires fabrication of many smaller parts and assembly of those parts [2].

Figure 1.1. a) design used in conventional manufacturing consisting of many smaller parts; b) design used in AM consisting of one part [2].

Most metal AM systems use an energy source to melt the feedstock in the desired location in each layer. The fusion of hundreds of layers produces the 3D shaped part according to the CAD file. There are specific software packages that produce the machine-readable code based on the CAD file, the layer size, the track size, the overlap of the tracks, and the hatch rotation (the change in the direction of each track based on the previous layer). However, the feedstock, energy source, and the feedstock delivery mechanism distinguish the metal AM systems from each other. In metal AM, energy sources are usually laser or electron beam, while the feedstock is wire or powder. Higher resolution can be achieved in metal AM when powder is used compared to wire [3]. Among all the laser-based metal AM systems developed in recent years, powder-fed and powder bed fusion (PBF) systems have attracted significant attention. PBF systems, also called selective laser melting (SLM) systems, use a platform that moves in the z direction in a controlled environment. Powder is transferred to the chamber and a coater or blade is used to spread a thin layer of powder on the platform. The laser, which moves in the x and y direction, is used to melt the powder in the desired shape, before another layer of powder is spread. A schematic of PBF is displayed in Figure 1.2. On the other hand, powder-fed systems, commonly called laser directed energy deposition (L-DED) systems, use a set of nozzles to spray the powder into the focal point of the laser to produce the part in a layer-by-layer manner (Figure 1.2). In L-DED systems the stage moves in the x and y directions and the laser moves in the z direction. In addition, usually SLM systems offer smaller laser spot size and powder size, which result in higher resolution and cooling rates. However, L-DED systems provide unique capabilities such as fabrication of gradient materials or repair due to the freedom in moving the parts’ orientation and location. Due to the short interaction between the laser and powder particles in AM, the cooling rate in the melt pool is higher than in conventional manufacturing; this produces unique properties with altered microstructure. The microstructure is also affected by the heat generated in the melt pool that tends to precipitate through the previously deposited layers and eventually reaches the platform. Although many processing parameters are involved in the AM process that influence the quality of the parts, not all of them are easily controlled. For instance, in L-DED the laser power, laser velocity, powder feedrate, hatch overlap, and layer thickness can be easily controlled by the user. However, there are other factors that can significantly affect the processing of metal powders in L-DED such as the powder characteristics, the oxygen concentration in the chamber, and the shield gas delivery rate. Powder characteristics are among the most important factors in the AM process and are discussed more extensively in the following sections of this dissertation.

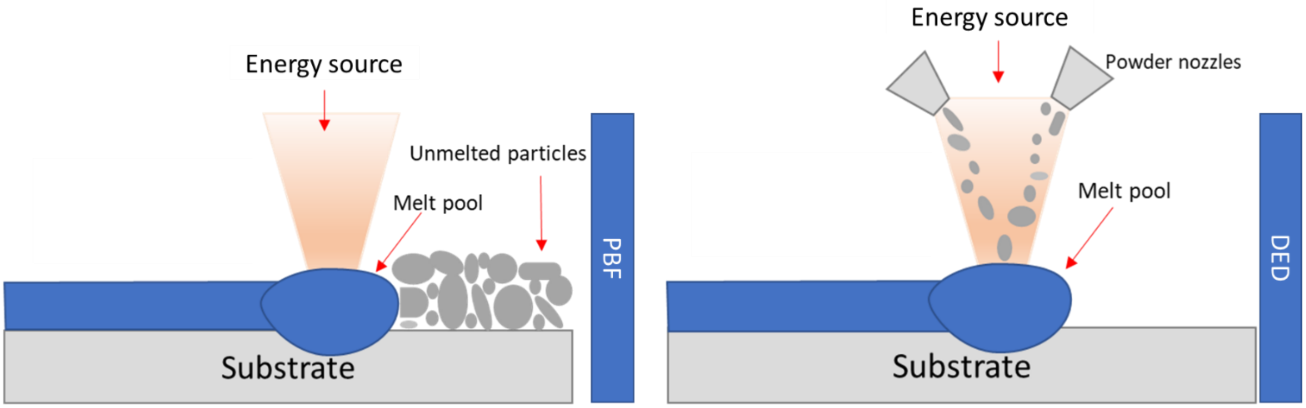

Figure 1.2. Schematic presentation of L-DED and PBF systems.

As AM systems have become more popular, the number of materials that have been processed has increased. Today a wide range of materials has been used in metal AM from stainless steel to Al alloys and nickel-based super alloys [4]. These alloys are used in different industries and applications, as shown in Table 1.1. Although the use of these alloys has been adopted in many industries, AM is still facing challenges in producing repeatable and reliable parts for industries such as aerospace [5]. As shown in Table 1.1, Al alloys have been adopted by aerospace and automobile industries due to Al alloys high specific strength. However, the composition of these Al alloys is very limited. The limited composition is due to unique physical properties of Al alloys that makes them more challenging to be processed in AM. Al alloys usually have a low melting point, high heat conductivity, high laser reflectivity, and poor flowability [6]. In addition, Al alloys are prone to hot cracking which results in limited use of high strength Al alloys in AM [7].

Table 1.1. Common alloys and industries in AM [8].

	Al	***Stainless steel***	***Ti***	***Co-Cr***	***Ni super alloys***	***Precious metals***
Aerospace	x	x	x	x	x	
Medical		x	x	x		x
Energy, oil & gas		x				
Automotive	x	x	x			
Marine		x	x		x	
Machinability and weldability	x	x	x		x	
Corrosion resistance		x	x	x	x	
High temperature		x	x		x	
Tools and molds		x				
Consumer products	x	x				x

AlSi10Mg is one of the most used Al alloys in metal AM. Numerous groups have studied the behavior of this alloy in AM [8]. AlSi10Mg shows medium strength and good corrosion resistance that makes this alloy a good candidate for automobile and aerospace industries. AlSi10Mg is a hypoeutectic alloy that shows good wettability and castability (the chemical composition is shown in Table 1.2 [9]). On the other hand, this alloy can be aged and hardened through formation of Mg_2Si precipitates that can improve the mechanical properties of the alloy without compromising other properties [10]. The solubility of Si in Al is very limited (below 2 wt.%), which can be seen in the phase diagram shown in Figure 1.3 [11]. When the alloy is melted in the melt pool, Al matrix starts to solidify first and as the melt pool is cooling down the Si is ejected by the solidified front into the liquid. However, the high cooling rate associated with AM increases the local solubility of Si in Al and an increased amount of Si in the Al matrix forms a super-saturated matrix. As the liquid is solidifying, the amount of Si in the liquid phase increases, and ultimately the eutectic structure forms [12].

Table 1.2. Chemical composition of AlSi10Mg [9].

	Al	Si	Fe	Cu	Mg	Mn	Ni	Zn	Pb	Sn	Ti
Wt.%	Bal.	9-11	<0.55	<0.45	0.2-0.45	<0.05	<0.1	<0.10	<0.05	<0.05	<0.15

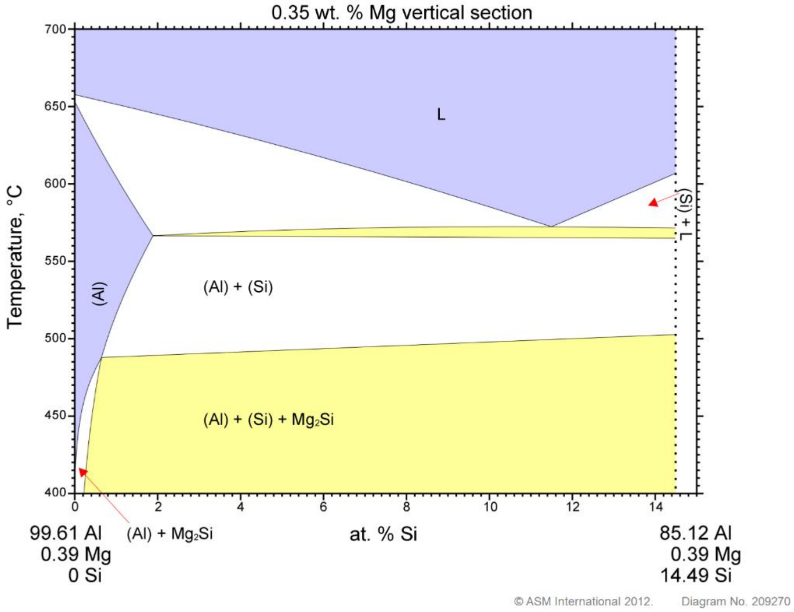

Figure 1.3. Vertical section of AlSi10Mg phase diagram [11].

1.1.1. Sustainability of additive manufacturing

AM has been adopted by different industries around the world, and the net worth of the industry has increased significantly [13]. It is predicted that the global worth and the compound annual growth rate will increase significantly in the future as well (Figure 1.4) [14]. The AM market has been continuing to grow as hundreds of millions of dollars are invested and new products are designed and built using AM [15]. AM shows great potential to decrease the overall cost of production by minimizing the need for large manufacturing facilities and highly skills workers. In addition, producing complicated parts through AM can decrease the production rate compared to the conventional manufacturing. Therefore, in expanding the use of AM in the future it is important to take advantage of AM's unique capabilities such as complex geometry design [16]. The increase in the adaptation of this novel technique in different industries will result in significant increase in the demand for raw materials.

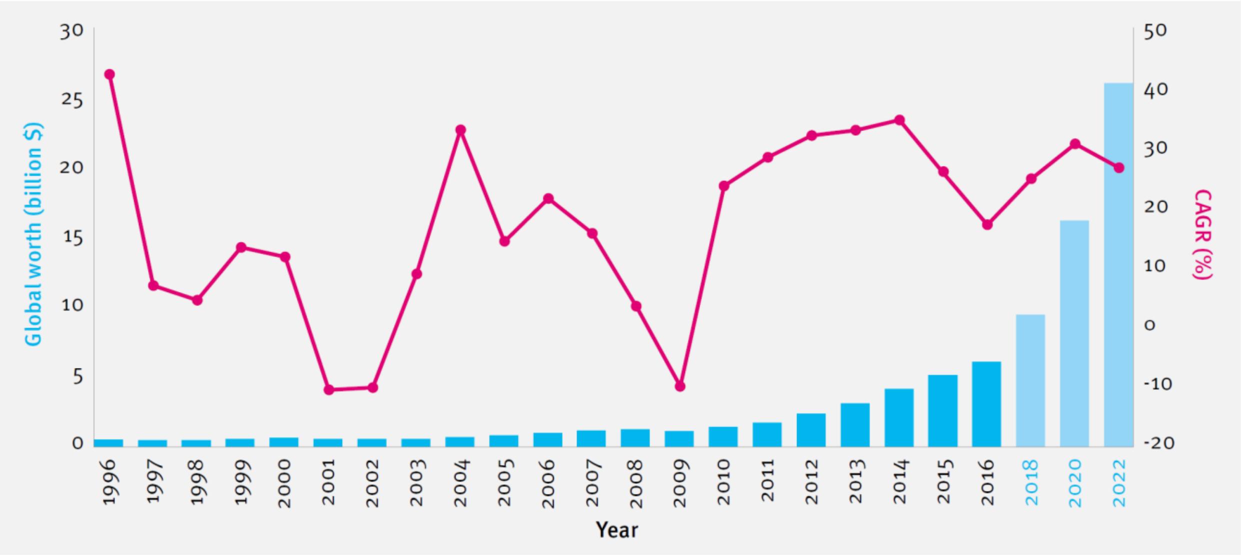

Figure 1.4. Estimated growth of the global AM industry. The global growth and compound annual growth rate are shown on the figure as well [14].

Early studies on AM considered this processing method an effective way to decrease the waste production and consequently reduce the production cost [17]. A study published in 2017 reported that when all the powder used in AM is recycled, this will result in almost 50% reduction in negative impact on potential ozone layer depletion and 40% improvement in potential fossil fuel resource depletion compared to other conventional manufacturing processes [18]. AM, with the promise of limited post-processing and deposition of the metal powder where it is needed, seemed the solution to sustainability concerns. Many studies showed that the environmental impact of fabricating parts with AM is lower; however, other studies showed that unless the powder is fully recycled this statement is not accurate. Other studies showed that if all the powder used in AM is reused, AM produces 90% less waste compared to subtractive manufacturing [19]. Ma et al.

suggested using powder capture efficiency to show what portion of the powder used in the deposition process is actually fused to form the final parts [20]. The powder capture efficiency can vary depending on the AM system and processing parameters, but usually it is between 3-25%. This means that a great portion of powder that is used during the process is going to end up unfused to the final parts. Kellens et al. showed that in depositing polymers such as PA 2200 in selective laser sintering, the greatest environmental impact is associated with the powder, as shown in Figure 1.5 [21]. The common practice is to recycle these powders for a known number of cycles or send them back to the powder manufacturer to remelt and produce fresh powder. However, as some of the AM applications require a repeatable and reliable quality such as the aerospace industry, more investigation into powder recycling is required.

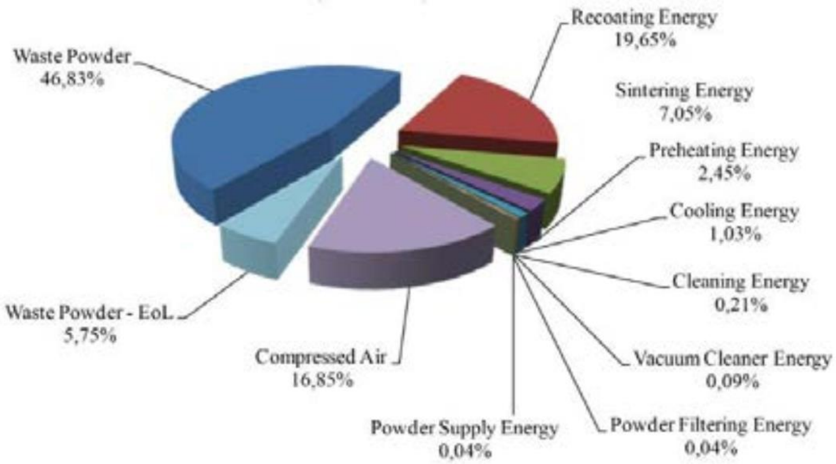

Figure 1.5. Environmental impact of depositing PA2200 in selective laser sintering [21].

Some studies reported that in comparison between AM and conventional manufacturing, environmental impact and economic assessment is highly dependent on the design and functionality of the part [16]. The orientation of the parts with respect to the laser, the need for depositing support structures, and the number of parts deposited at the same time can change how much powder and time is required. It is noteworthy to mention that the energy consumption of the AM process is one of the parts of the process with the greatest environmental and economic impact.

However, if the whole lifetime of the parts manufactured in AM is considered, the AM parts can be highly desirable. Due to the freedom in design, there is a great potential to reduce the weight of the parts used in the aerospace and automobile industries. It is estimated that the current practical range can be almost doubled [22]. As the AM industry continues to grow, the amount of powder needed for this process increases as well. On the other hand, the energy consumption and environmental impact of powder production to respond to the increased powder demand in the AM field is increased. Therefore, an investigation into more sustainable feedstock for AM is crucial.

1.1.2. Additive manufacturing feedstock

Different AM technologies are able to use a variety of feedstocks from sheets and wires to powder [8]. Metal powder is one of the most used feedstocks in the AM field. Powder that has a different size and shape depending on the manufacturing process plays an important role in the AM process. The quality of AM parts is influenced by the characteristics of the alloy powder used as the feedstock. These characteristics include but are not limited to the particle shape, size, true density, surface roughness, particle size distribution, and impurities [23]. In the literature, it is reported that spherical particles, with smooth surfaces and narrow particle size distribution, are more desirable for use in AM [23]. Spherical particles tend to occupy the space more efficiently, which is important in PBF technologies, and finer particles can occupy the space between the larger particles. In the L-DED system, powder morphology and size also play an essential role. They determine how easily particles interact with each other and flow in the system [24]. Powders that are typically used in AM are produced by: gas atomized (GA), water atomized (WA), rotary atomization, and plasma rotating electrode process. However, less common powders, such as milled powder, have been produced by other methods. Each of these processes produces powders with different morphologies and surface finishes. The micrographs of the particles produced by each method are displayed in Figure 1.6 [8,25]. The plasma rotating electrode process produces the most uniform and perfectly spherical particles with smooth surfaces, although it is the most expensive powder. The focus of our work is on GA and milled powder, and each method is explained in the following sections.

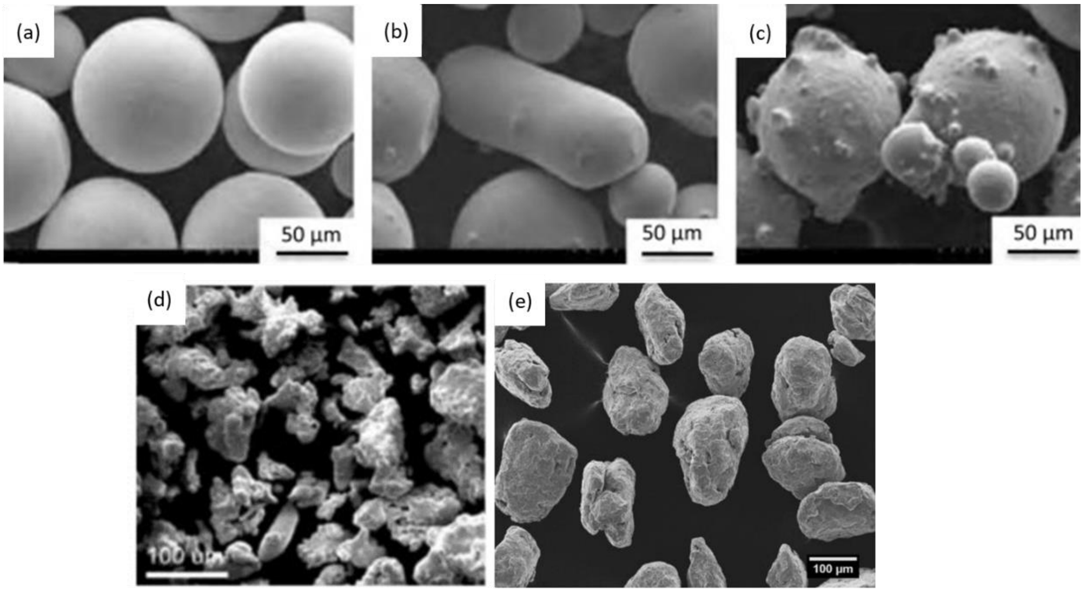

Figure 1.6. SEM micrographs of alloys produced by a) plasma rotating electrode process b) rotary atomization c) gas atomization process d) water atomization, [8], and e) milled powder [25].

1.1.2.1. Gas atomization

Gas atomization (GA) is a process that melts the metal alloy ingots and uses a high-pressure stream of inert gas to create the fine spherical particles; a schematic of this process shown in Figure 1.7 (a). This process has been used for many years to produce powder for different applications through powder metallurgy. GA requires a significant amount of energy to melt the metal ingot and keep the temperature high enough for the molten metal to flow out of the nozzle with the desired consistency. The GA process usually produces powder with spherical morphology and a controllable size range. Although most of the particles produced through GA have spherical shapes, some of the particle have elongated shapes, satellites on the surfaces, and porosity inside the particles (Figure 1.7). Besides energy consumption, inert gas and other consumables make this process very expensive [26]. Although the yield of the atomization process can be improved [27], oversize and undersize particles in each batch increase the cost and waste of the process [23]. In order to overcome these challenges, many researchers have explored the fabrication and processing of alternative powders with lower environmental impact and that are more economically profitable. For instance, WA and milled powder have been used in AM [25,28]. However, more work on alternative feedstocks in AM is required.

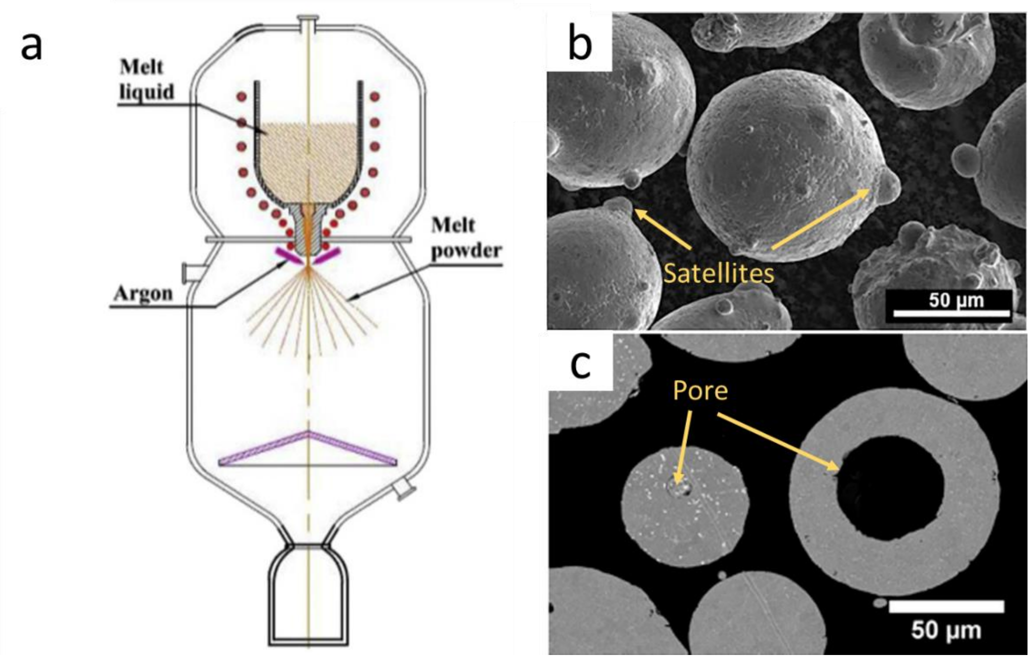

Figure 1.7. a) schematic of the gas atomization process [29], b) the satellites observed on the surface of the GA particles, c) the pores observed inside the GA particles [23].

1.1.2.2. Milled powder

Ball milling usually uses a specific amount of small balls (stainless steel in a specific size) that moves with high energy in a vessel [30]. The balls are either moved with the movement of the vessel, similar to systems such as planetary ball mill, or by the rotation of an attritor in the vessel. The media of the milling process can play a very important role on the yield of the process, size, and the microstructure of the particles. Usually milling is performed in an inert atmosphere to prevent the oxidation of powders [30]. A cryogenic liquid such as liquid nitrogen can also be used as the milling medium to perform cryomilling [31]. In conventional manufacturing, a large portion of the raw material will end up as machine chips or other forms of waste. For instance, in Ti industry almost 80% of materials consumption ends up as a form of machine chips which later needs to be recycled [32]. However, milling has not been extensively used to produce powder for AM. The powder that is produced through milling normally does not have spherical shape and could be contaminated during the machining and milling process. In one study published in 2019, the single tracks deposited with 304L GA and milled powder showed minimal differences in the morphology and microstructure [25]. Another group investigated the differences in the microstructure and mechanical properties of parts manufactured in L-DED using two different 316L feedstocks: GA and ball milled powder. They showed that the parts have very similar mechanical and microstructural properties regardless of power processing technique [33]. Furthermore, the use of other high energy milling techniques on other metallic alloys has not been investigated.

1.2. Research scope

As AM gains more popularity, understanding the relationship between the powder characteristics and bulk properties becomes more important. Besides powder properties, the effect of other processing parameters on the physical, microstructural, and mechanical properties of the AM parts plays a vital role in introducing more sustainable AM life cycles and improvement in the properties of the parts. This work aims to gain a deeper understanding of the processing and deposition of Al alloys in different AM processes, improving our knowledge of how different processing parameters can affect the parts and powders. We tackle this task by experimental work covering different stages of the powder journey from fabrication to deposition. The framework of this work tries to target two main aspects of the AM process: the powder processing and characterization are explored in Chapters 2 and 3, and AM processing of Al alloys and understanding the effect of the process on the parts themselves and the feedstock particles are described in Chapters 4 to 6.

Chapter 2 focuses on the relationship between the physical properties of the powder particles such as size and morphology, and the flowability. In this work, different stainless steel and AlSi10Mg powders with different size ranges and morphology were used. In addition, the state-of-the-art powder flowability systems along with a high-speed camera were used to analyze the particles and their behavior.

Chapter 3 focuses on using milling (planetary ball milling and cryomilling) on the processing of AlSi10Mg waste products to produce the powder necessary for AM. A thorough investigation is conducted to understand the relationship between the processing parameters and powder characteristics.

The deposition of AlSi10Mg in L-DED faces significant challenges. Without a deep understanding of the interaction between the powder and the laser during the deposition of single tracks and bulk samples, it is impossible to overcome these challenges. Chapter 4 investigates the scalability of the single tracks to bulk deposition of AlSi10Mg in L-DED.

Due to low powder capture efficiency in L-DED, there is a significant amount of powder that needs to be reused. However, the effect of reusing AlSi10Mg powder in L-DED on the powder properties and mechanical properties of the parts is not clear. Chapter 5 focuses on understanding the effect of reusing the powder in L-DED on the powder and properties of the final parts.

In order to improve the mechanical properties of Al alloys in AM, the feasibility of deposition of aluminum matrix composites single tracks is investigated. Chapter 6 analyzes the effect of the addition of the ceramic reinforcement on the morphology of the single tracks and their microstructure.

Chapter 2: A Statistical Analysis of Powder Flowability in Metal Additive Manufacturing

Abstract

The quality of parts fabricated with additive manufacturing is influenced by the flowability of the feedstock particles, which is the result of many factors, including chemistry (e.g., true density, the presence of surface oxides, impurities), morphology (e.g., particle shape, presence of satellites), and particle size distribution. This work investigates the relationship between powder characteristics and flow behavior of different powders by using three flowability testing methods. Six powders of two compositions (316L stainless steel and AlSi10Mg), made using two different methods (gas- and water-atomization), were investigated to rationalize the effect of powder chemistry and morphology on flow behavior. The results show that the true density of the powders can influence several flowability metrics. Additionally, aspect ratio strongly influences the initiation of flow from a static condition, while average particle size strongly dictates the ease of maintaining that flow.

2.1. Introduction

Despite being a growing industrial manufacturing processes, additive manufacturing (AM) currently struggles with repeatability of final part quality. One cause of this inconsistency is the large number of process parameters involved [35], with powder feedstock quality being among the most important ones. Gas atomized (GA) powder is the most common feedstock in metal additive manufacturing and typically corresponds to spherical particles with normal particle size distributions [36]. However, the shape, size, surface roughness, and particle size distribution of GA particles can impact the powder's flowability, and therefore the AM process. Studies have shown that both bulk density (i.e., lack of porosity) and mechanical properties of the final parts, as well as temperature and laser absorption of the melt pool are affected by powder properties [37,38].

Although powders obtained with different methods have different flow characteristics [39], even powders produced by similar techniques also show differences that will impact processability [40]. While the relationship between flowability and part quality has been documented [39], the relationship between powder characteristics and flow behavior is not completely understood. Powder flow behavior is often characterized with simple techniques, each of which produce unique and quantifiable metrics such as angle of repose, Hausner ratio [41], and Hall flowrate [8]. However, these methods are often unreliable, as they do not accurately represent actual powder behavior in AM [42]. For example, Hall flow measurements show no trend in the flow of recycled powders despite changes in particle size distribution and sphericity after several reuse cycles [43]. New powder flow measurement techniques have been introduced that are able to quantify flow behavior from relatively simple tests [42]. Unfortunately, little evidence is currently present on how relevant these methods are to different additive manufacturing processes (e.g., powder-fed vs powder-bed based), as well as the overlap/agreement between the information acquired from different techniques. Although different laser based AM techniques operate on similar principals, the powder delivery systems can be quite different between the various techniques. In both systems, powder is stored in a hopper and then transferred to the chamber. The discharge of powder from the hopper requires overcoming a static condition to initiate the flow. Once initiated, a consistent sustained flow is required in order to have a homogenous part in both AM techniques.

To overcome some of the challenges limiting the successful application of AM, such as inconsistent part quality and poor surface finish, it is vital to understand the relationships between powder characteristics and flowability. In this work, I compare the results obtained from a variety of powder flowability measurement techniques to gain a deeper understanding of how powder characteristics influence flow behavior related to metal additive manufacturing processes.

2.2. Materials and method

Six powders with two compositions (316L stainless steel (true density: 7.95 g/cm^3 [44]) and AlSi10Mg (true density: 2.68 g/cm^3 [45]) and different particle size ranges were tested; the composition, manufacturing process, reported particle size range, particle size distribution parameters (D_{10}, D_{50}, D_{90}), span, average aspect ratio, and manufacturer for each powder are provided in Table 2.1. The two compositions also introduce the variable of 'true density', which is also considered in this study.

Table 2.1. Details on the powders used in this study. SS = stainless steel.

Composition	Manufacturing Process	Reported Particle Size (μm)	D_{10}, D_{50}, D_{90} (μm)	Span	AR_{50}	Manufacturer
316L-SS	GA	16-45	27, 38, 48	0.56	0.82	Carpenter
316L-SS	WA	25-45	40, 55, 74	0.63	0.68	Hoeganas
316L-SS	GA	46-105	67, 94, 126	0.62	0.85	Carpenter
316L-SS	GA	25-60	34, 47, 59	0.52	0.80	SLM Solutions
AlSi10Mg	GA	46-150	75, 101,145	0.70	0.81	Valimet
AlSi10Mg	GA	26-66	27, 45, 66	0.85	0.79	SLM Solutions

Two laser diffraction systems, a Microtrac (S3500) and Sympatec (Helos), were employed to acquire particle size distribution, average particle size (D_{50}), and the average aspect ratio (AR_{50}). Particle size was calculated as the diameter of the equivalent projected circle of the particle. AR_{50}, which ranges from 0-1, was calculated using $\frac{minimim\ diameter}{maximum\ diameter}$ of the particle. The span of the particle size distribution was calculated using $Span = \frac{D_{90}-D_{10}}{D_{50}}$.

Flowability of the particles was measured using three different techniques: an FT4 powder rheometer from Freeman Technology [46], a Revolution powder analyzer from Mercury Scientific, Inc. [47], and a custom-built modified funnel method, with each experiment repeated at least three times and averaged. The schematic of three powder flowability technique used in this study are shown in Figure 2.1. The FT4 operates by moving an impeller through 25 ml of powder and measuring the resistance to flow. Parameters that can be quantified with the FT4 powder rheometer include basic flowability energy, specific energy, aerated energy, pressure drop, permeability, compressibility, shear stress, flow function, and wall friction angle. The Revolution powder analyzer visually analyzes the behavior of 100 ml of powder while it is rotating. Parameters that can be quantified with the Revolution powder analyzer include avalanche angle, avalanche energy, SL ratio, break energy, energy slope, rest curvature, surface fractal, maximum break point, maximum break energy, maximum break angle, and apparent density increase [47]. The funnel method can measure flow rate. Not all measured parameters were analyzed, since not all correspond to the process conditions associated with additive manufacturing. For instance, the compressibility index would be more relevant to consolidation methods that require the application of pressure before or during densification. Thus, the following six parameters were selected for detailed analysis in this study: specific energy (SE), shear stress (τ), avalanche angle (AA), apparent density increase (ADI), maximum break angle (MBA), and flow rate (FR). Specific energy [mJ/g] is the energy required to maintain unconfined (low stress) flow, and is calculated using the average of the energy required for the blade to displace the powder in an upward motion divided by the conditioned powder mass [48], and can provide insight on gravity-induced flow, like hopper discharge. Powder conditioning refers to the powder being gently displaced in order to loosen it and prepare it for flow. Higher values of specific energy correspond to a greater resistance to sustained flow. Shear stress, τ, [kPa] is measured by applying 7 kPa of stress to the powder and then a rotational torque to determine the stress at which flow initiates. Higher values of τ suggest more resistance to initiating flow [39]. Avalanche angle [deg] is a linear regression of the surface of the powder in its highest potential before the avalanche occurs. Apparent density increase [%] is the increase in apparent density of the powder particles, measured by observing the reduction in powder volume, after vibrating the drum for a known time. Maximum break angle [deg], which is measured after vibrating the drum, is the maximum angle the powder exhibits before the avalanche event that initiated the flow. Higher values for maximum break angle and avalanche angle indicate greater resistance to flow [47]. Flow rate was measured with a modified funnel method using a glass funnel with an inner diameter of 4 mm, placed 30 cm above a collection dish. Three batches of 50 g each were tested for each powder. The flow rate [g/s] was determined by measuring the time required for the powder to be completely expelled from the funnel. A high-speed camera (Photron SA-Z) using 500 fps (frames per second) was used to improve the resolution of the measurement.

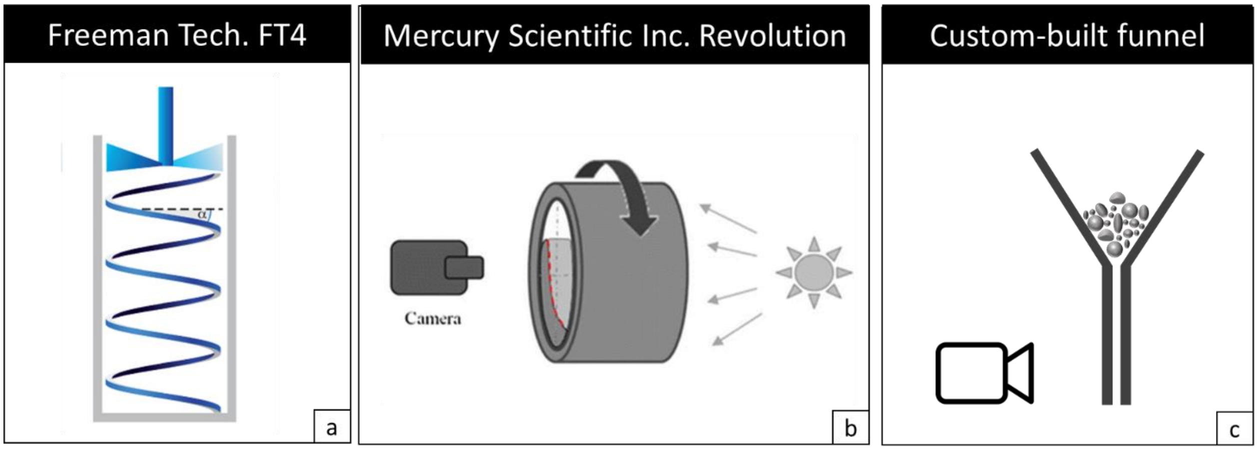

Figure 2.1. The schematic presentation of a) FT4 from freeman Technology, b) Revolution powder analyzer by Mercury Scientific Inc. c) custom build funnel flow rate.

2.3. Results and discussion

The correlation among the six flowability parameters noted above and the three powder particle characteristics were evaluated statistically. The Pearson correlation coefficients (R-value) between the analyzed quantities were visualized using Corrplot, as shown in Figure 2.2 (the raw data are provided in Figures 2.3-2.4, as described below) [49]. The colored circles represent the R-values; larger circles show stronger correlations. The colormap displays the distribution of R-values from negative (red) to positive (blue). The lower left of the matrix includes only 316L stainless steel powders while the upper right considers both AlSi10Mg and 316L stainless steel powders (All). Three observations can be made from Figure 2.2: (1) Some flowability parameters are correlated with other parameters, indicating that different techniques can yield similar information. (2) Every flowability metric has a strong correlation (defined here as $R>0.7$) with at least one powder particle characteristic. (3) The stainless steel dataset displays higher R-values overall (average R-value=0.59) compared to the 'All' powders dataset (average R-value=0.46). The inclusion of the AlSi10Mg dataset reduces the R-values, implying that material composition and density could influence flowability. The above observations, along with several parameter correlations, are explored in more detail below.

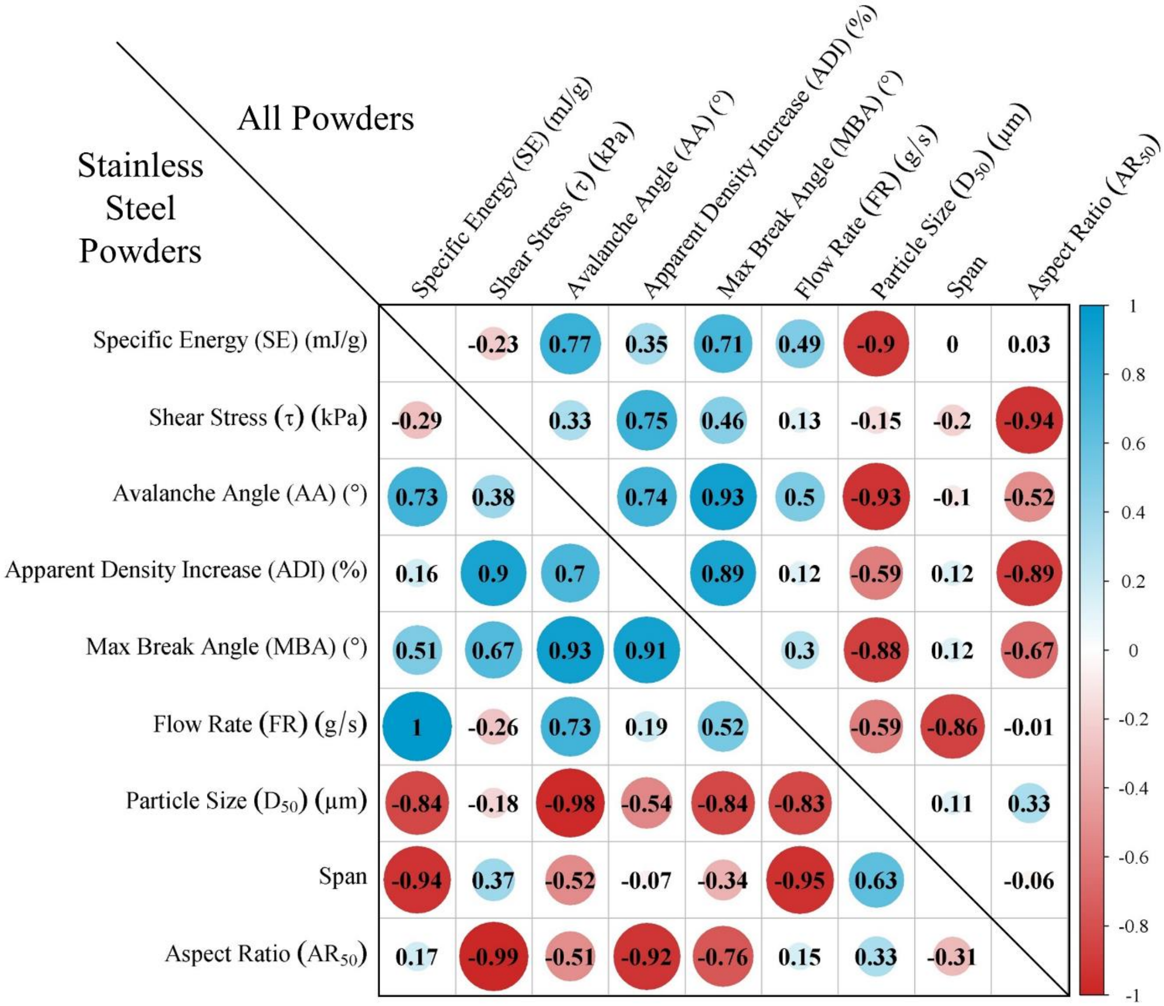

Figure 2.2. R-values correlating parameters used in this study. The lower left of the matrix displays R-values for stainless steel powders, while the upper right is for all powders. The size of the circles shows the intensity of the correlation, while the positive /negative numbers and the blue/red colors indicate direct/inverse correlations, respectively.

During additive manufacturing, powders often sit in hoppers before flow is initiated. Understanding how this static condition is overcome is critical for understanding flowability. Both the FT4 and the Revolution powder analyzer have several measurements available that quantify the ease with which powder flow is initiated. In this work maximum break angle (MBA), apparent density increase (ADI), and shear stress (τ) were used to assess this flowability scenario. The well-correlated MBA-ADI (Figure 2.3 (a)) and τ-ADI (Figure 2.3 (b)) relationships suggest that powders that can pack more densely will stick to each other more and resist the initiation of flow, i.e., higher values of apparent density increase indicate poor flow. A modest MBA-τ correlation is observed (Figure 2.3 (c)), indicating that measurements of packed powder flow in the FT4 and the Revolution powder analyzer do not describe the exact same scenario. Measurement of shear stress, τ, (using the FT4) involves breaking a compacted powder with a mechanical force, which is a different scenario than the gravity-initiated maximum break angle measurement from the Revolution powder analyzer.

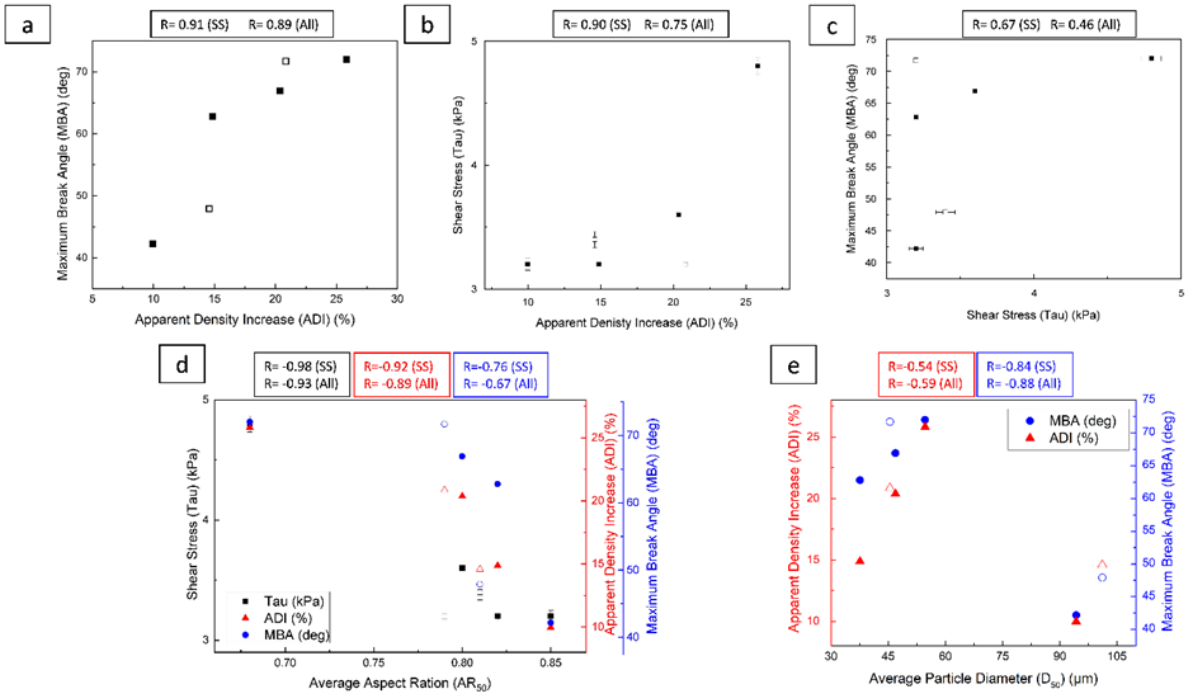

Figure 2.3. a) MBA vs. ADI b) τ vs. ADI c) MBA vs. τ. d) ADI, τ and MBA vs. AR_{50}.e) ADI and MBA vs. D_{50}. Hollow points signify AlSi10Mg, and filled points signify SS. (MBA=maximum break angle; ADI=apparent density increase, τ=shear stress; AR_{50}=average aspect ratio; D_{50}=average particle diameter; SS=stainless steel).

The shear stress values for gas atomized powders fall in a narrow range (3.2-3.6 kPa), indicating that there is a lower limit to the force required to move gas atomized particles regardless of composition. The outlier in the shear stress dataset is the water atomized powder, which has irregularly shaped particles with rougher surfaces compared to the gas atomized powders. Apparent density increase, maximum break angle and shear stress show mostly strong negative correlations with average aspect ratio (AR_{50}) (Figure 2.3 (d)). Higher AR_{50} values indicate that the particles are more spherical, leading to lower apparent density increase, maximum break angle, and shear stress values, i.e., particles move past one another and flow more easily. Spherical particles tend to pack more efficiently compared to irregularly shaped particles that have low AR_{50} [50]. However, a powder made of irregularly shaped particles that is initially loosely packed will produce a greater apparent density increase after conditioning, since there is more space available to be occupied after particle re-orientation, explaining why higher apparent density increase values are observed for the water atomized powder following mechanical agitation.

Although a strong correlation exists for the MBA-AR_{50} and ADI-AR_{50} relationships (Figure 2.3 (d)), Figure 2.3 (e) shows that maximum break angle and apparent density increase are also dependent on D_{50} (average particle size), highlighting how two powder characteristics (D_{50}, AR_{50}) both manifest their effect on the same quantity (maximum break angle and apparent density increase), making it difficult to de-convolute each contribution. The strong negative MBA-D_{50} correlation occurs because finer particles have an increased tendency to agglomerate and experience interparticle friction compared to larger particles [51]. For similar reasons, the modest negative ADI-D_{50} correlation (R= -0.54 and -0.59) indicates that larger particles will pack more efficiently, although aspect ratio will have a greater influence than particle size. Finally, the correlations in Figure 2.3 are mostly independent of powder composition, indicating that initiation of flow might not be influenced by true density. Initiation of powder flow from a static condition will depend primarily on the packing and interaction between the particles and not on the mass of the powders themselves, explaining why true density does not strongly influence these flowability parameters.

Apparent density increase, maximum break angle, and shear stress are important parameters for understanding the behavior of particles during hopper discharge in both powder-fed and powder-bed additive manufacturing systems. Powders that resist the initiation of flow will result in inconsistencies in what is sent to the powder delivery system, leading to porosity in the final parts. Apparent density increase can also be indicative of compaction behavior in powder-bed systems. The packing density of the powder after being spread on the bed plays an important role in the density and properties of the final parts. The results of this study show that lower AR_{50} values result in lower initial powder packing, which can lead to increased porosity in the final parts. Therefore, powders with lower AR_{50} or finer particles can hinder the quality of the processed parts.

All three flow analysis techniques use different quantities to describe how well flow is maintained after being initiated. These quantities are more consequential in powder-fed systems, which maintain powder flow throughout deposition. Inconsistent flow during deposition will lead to an inhomogeneous concentration of powder, which will lead to porosity in the final part. Here, flow rate (FR), avalanche angle (AA), and specific energy (SE) are used to quantify continuous flowability. The correlations between these quantities are depicted in Figure 2.4. A strong composition-independent SE-AA correlation can be observed in Figure 2.4 (a), demonstrating that both the FT4 and the Revolution powder analyzer convey similar information about unconstrained flow. Composition-dependent SE-FR and FR-AA relationships can also be observed (Figure 2.4 (b), (c), respectively). However, this correlation is misleading, as discussed below.

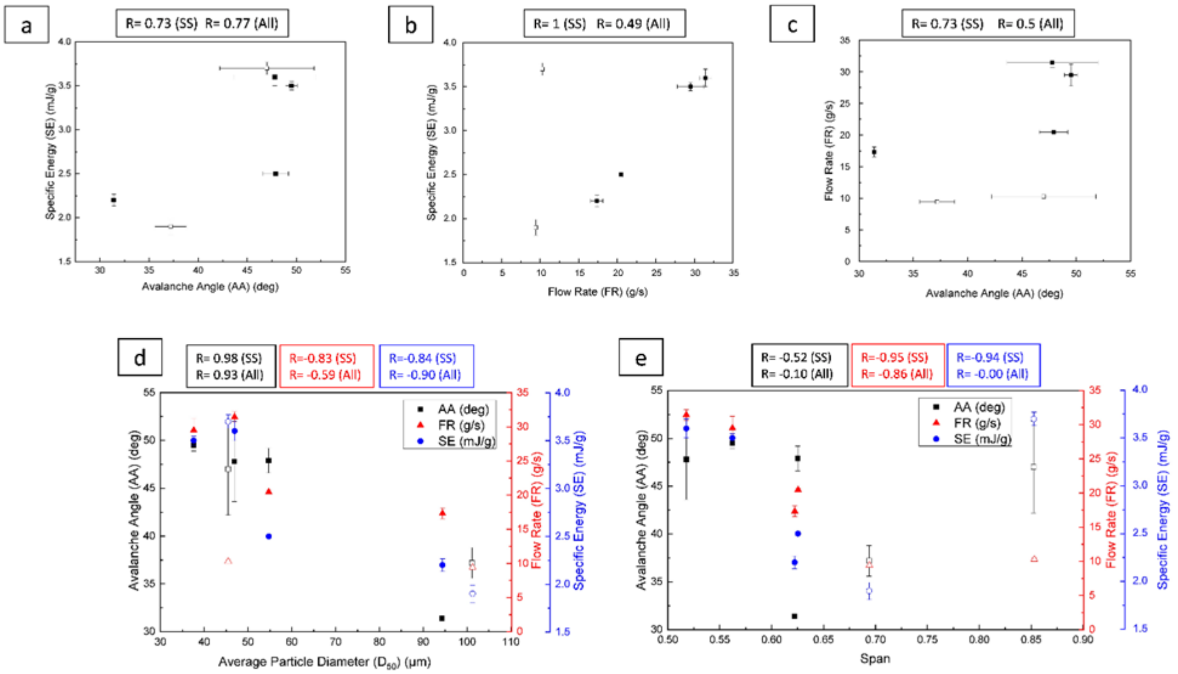

Figure 2.4. a) SE vs. AA b) SE vs. FR c) FR vs. AA. d) FR, AA, SE vs. D50 e) FR, AA, SE vs. span. Hollow points signify AlSi10Mg, and filled points signify SS. (SE=specific energy; AA=avalanche angle; FR=flow rate; AR_{50}=average aspect ratio; D_{50}=average particle diameter; SS=stainless steel).

Flow rate, avalanche angle, and specific energy have a strong negative correlation with D_{50} (Figure 2.4 (d)). Finer particles increase agglomeration and inter-particle friction leading to increased resistance to flow [51], which is consistent with the composition-independent AA-D_{50} and SE-D_{50} relationships. Strong SE-Span and FR-Span correlations are observed when only stainless steel powders are considered (Figure 2.4 (e)). Powders with greater spans have more fine particles that can fit between coarser particles, increasing the number of particle-particle contact points and making flow more difficult. Contradicting this, specific energy and avalanche angle measurements are inversely correlated with span and become independent of span when all powders are considered due to a single outlier AlSi10Mg powder with an unusually large span. The non-intuitive results and sensitivity to outliers indicates that span may not meaningfully contribute to specific energy and avalanche angle. There is a modest correlation between span and D_{50} when considering only the stainless steel powders (R=0.63), indicating that any correlations with span will be convoluted by the influence of the D_{50} values. Conversely, there is no correlation between span and D_{50} when all the powders are considered (R=0.11). Given the composition independence of the AA-D_{50} and SE-D_{50} relationships, it can be surmised that D_{50} plays a larger role in the avalanche angle and specific energy measurements than composition, which plays a larger role than span. Although specific energy and avalanche angle are two parameters that can describe flow in powder-fed systems, these two parameters are also important in understanding the behavior of the particles in powder-bed system. Lower specific energy and avalanche angle values indicate that particles are less likely to interact with each other and restrict flow, resulting in more homogenous powder spreading.

The flow rate measurements in this study contradict the trends seen in the avalanche angle and specific energy measurements. Flow rate increases as specific energy and avalanche angle increases (Figure 2.4 (b), (c)), which is contradictory given that lower specific energy and avalanche angle values suggest lower resistance to flow. However, the three methods fundamentally measure different things and the contradictions in flow rate can be explained by considering the limitations of the funnel method. The negative FR-D_{50} correlation means more time is needed for larger particles to exit the funnel, resulting in a reduced flow rate and behavior that contradicts the avalanche angle and specific energy measurements. The contradiction arises from the flow being constrained by the funnel diameter. Large particles become confined in the narrow funnel, leading to restricted flow [52]. Additionally, the low true density of the Al alloy powders causes the FR-D_{50} correlation to decrease significantly, which is consistent with the gravity driven nature of the funnel method. The inverse FR-Span correlation means that as the particle size distribution gets wider the flow rate decreases. A larger span should translate into higher internal friction during flow, explaining the reduction in flow rate.

2.4. Conclusions

The flowability of powders in additive manufacturing, which can affect the quality of the final parts, is not completely understood in the literature. Using two commercially available powder flow analysis techniques (a Revolution powder analyzer and a FT4 powder rheometer), and a modified funnel method, we have analyzed the flow behavior of six different powders under conditions relevant to additive manufacturing. The following results have been observed:

- The FT4 powder rheometer, the Revolution powder analyzer, and the modified funnel method show some correlation between their various measured parameters. For example, avalanche angle measured using the Revolution powder analyzer and specific energy from the FT4 powder rheometer show a strong correlation regardless of the powder composition. However, these correlations are not always meaningful as each method measures a distinct flow scenario, and desirable flow behavior for one method may not apply to the others.
- Average aspect ratio (AR_{50}) is the most consequential powder characteristic with respect to initiating flow from a static condition. Maximum break angle from the Revolution powder analyzer and specific energy from the FT4 powder rheometer confirm that non-spherical powders tend to pack with lower apparent density but exhibit significant apparent density increases after settling.
- The most consequential characteristic for maintaining flow is average particle size (D_{50}), with larger values granting easier flow according to the Revolution powder analyzer and FT4 powder rheometer. Larger particles exhibit a reduced flow rate in the modified funnel method due to its gravity-driven nature.

- Parameters such as shear stress, maximum break angle, and apparent density increase are not influenced by powder composition, indicating that true density does not play a role in the initiation of flow; whereas the true density of the powders could play a significant role in sustaining consistent powder flow.

Chapter 3: Using Waste Material to Fabricate Powder Feedstock for Additive Manufacturing

Abstract:

As additive manufacturing (AM) is gaining more popularity, the demand for its feedstock increases as well. The typical powder used in AM, gas atomized (GA) powder, is produced using a very energy-intensive and consequently expensive process. GA powder used in AM has spherical shape and is usually smaller than 150 μm to be used in different AM technologies. Novel feedstock for AM can be produced through milling waste materials. The support structures that are a side product of selective laser melting were used as a starting material to produce the feedstock for AM. This study investigated the feasibility of using planetary ball milling and cryomilling to produce AlSi10Mg powder smaller than 150 μm. The ball size, process control agent, and milling duration were optimized to achieve the highest yield. Process parameter optimization in the planetary ball mill resulted in over 75% yield. Similarly, using cryomilling, more than 80% of the particles were smaller than 150 μm after process parameters optimization. The yield, particle size, and morphological features of the particles were investigated. Preliminary attempts to deposit the cryomilled powder were explored.

3.1. Introduction

Throughout history, many manufacturing processes have been improved, and new techniques have been developed. However, these processes each have their own limitations and disadvantages. For instance, in many conventional subtractive manufacturing systems, different forms of machine chips or other kinds of waste are produced. In the stainless steel industry, almost 2/3 of the raw material ends up as a kind of waste. Depending on the cutting condition, tool geometry, and workpiece material, the machine chips may have different sizes and morphologies [53]. These waste materials usually need to be recycled, mostly through conventional melting. However, collecting and purifying machine chips are challenging processes and make the recycling process less profitable. One of the main challenges in recycling machine chips is the separation and removal of machining oils. Additionally, contamination from the cutting tool or other cross-contaminations makes the remelting process more challenging [54]. In order to overcome some of the challenges in the remelting process and reduce the cost, some studies have focused on developing solid-state methods to recycle waste materials. Compared to conventional remelting, solid-state recycling paths can lead to saving 40% in materials, 26-31% in energy, and 16-60% in labor [55].

The solid-state recycling of Al scrap is generally based on severe plastic deformation and powder metallurgy techniques. Severe plastic deformation techniques included: 1) hot extrusion, 2) equal channel angular pressing, 3) cyclic extrusion compression, 4) friction stir extrusion, 5) high press torsion, and 6) screw extrusion [56]. The powder produced through powder metallurgy can be used in a variety of techniques, such as forging and injection molding. In addition, many researchers focused on developing other novel solid-state technologies. There are studies that focused on using waste Al cans to produce powder for different powder metallurgy techniques, and they showed that Al waste from different sources show different machinability and surface roughness [57]. Canakci et al. introduced mechanical milling to produce powder from machine chips with morphology comparable to powder manufactured in the atomization process [58]. Mahmood et al. used laser metal deposition to deposit machine chips without any further processing. They reported that no significant porosity or solidification defects were observed [59].

Additive manufacturing (AM) is known as a process that can potentially minimize the amount of waste produced. The powder used in AM can be reused several times [60]; however, there are other wastes produced during the selective laser melting (SLM) process whose recyclability is yet to be investigated. Support structures are one of the essential components in printing parts in SLM, which that usually are sent to conventional recycling facilities. The support structure is composed of two main functional areas: the main support and the teeth [61]. The teeth connect the main part of the support to the build and the platform. The variation in the geometry of support structures commonly used in SLM is displayed in Figure 3.1 [61]. The support structures are essential in printing parts in SLM to prevent distortion and deformation during printing and connecting different components to the main body. More importantly, support structures facilitate dissipation of heat from the melt pool to the platform. The heat dissipation plays a significant role in the temperature and thermal history of the part and, consequently, their properties. Support structures should be strong yet easy to remove from the final parts. After deposition, the support structure can be broken off from the main parts or be cut using systems such as wire electric discharge machining (EDM). Since the support structures are printed with the same highly pure powder that is used to print the main parts in the controlled environment, the amount of contamination introduced is minimal. Support structures are another waste stream, similar to machine chips, that can be converted into a usable, low cost, and environmentally friendly alternative feedstock for AM.

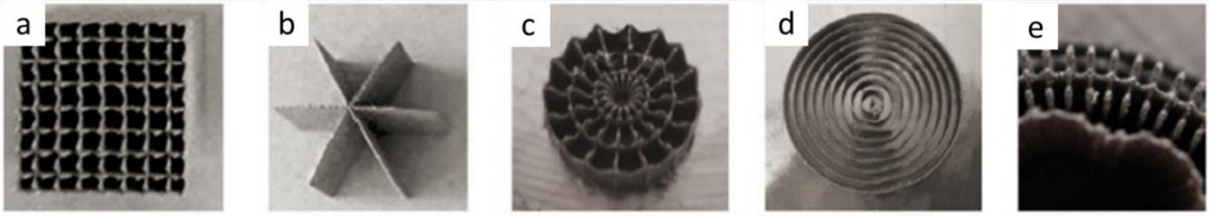

Figure 3.1. Different types of support structure printed in PBF a) block, b) point, c) web, d) contour, e) line [61].

As mentioned previously, mechanical milling has been used as a solid-state process to recycle machine chips [62]. High energy milling processes such as planetary ball mill (PBM) apply a much larger energy density to the particles during the milling duration. Fullenwider et al. used PBM to produce semi-spherical stainless steel particles to be used in AM [63]. They showed that single tracks deposited with the milled powder have very similar properties and microstructure compared to the single tracks deposited with gas atomized (GA) powder. GA is the most common powder used in AM and typically has a spherical morphology. During the milling process, kinetic energy is transferred to the powder particles as balls continuously collide with each other. Usually, the particles that are located between the balls will undergo continuous fracture and welding. Cold welding that is observed in the milling of Al and other ductile alloys is obtained by the joint plastic deformation of two metals, in this case, two metal particles [64]. In order to overcome the excessive cold welding, surface-active substances (process control agents, PCAs) are used. Although PCAs introduce contamination to the powders, they improve the mechanical alloying and the duration of the milling process. Stearic acid ($C_{17}H_{35}CO_2H$) has been widely used as a PCA in milling Al alloys [65]. In addition, the size of the balls and the ball-to-powder ratio can play essential roles in the yield and morphology of the particles. As the size of the ball used in milling increases, the depth of the impact into a particle increases, as does the possibility of overcoming the ultimate tensile strength of the particles [25]. In addition, using larger balls in the milling process decreases the contact frequency, which can affect the yield of the process. In the current study, we investigated the effect of PCA, ball size, and duration of milling on the morphology and yield powders produced from support structures, using PBM. In addition, the effect of PCA and ball size on cryomilled support structures was also investigated.

3.2. Materials and methods

The AlSi10Mg support structures were provided by the Morf3D company [66]. The AlSi10Mg support structures, shown in Figure 3.2, were kept separate from the rest of the waste produced in the facility. Depending on the design and functionality of the support structure, the support structures had different sizes and shapes. Most of the support structures printed in Morf3D were larger than 10 cm long and could not be directly used in any milling process. To reduce the size of the support structures, a cutting mill (Retsch 2000) was used to shred the support structures into particles smaller than 1 mm. Support structures usually have a porous structure, and fine feedstock particles can be trapped in them. To separate these fine GA particles from the shredded particles, shredded particles were sieved to remove particles smaller than 150 μm in diameter. The larger particles were used for milling.

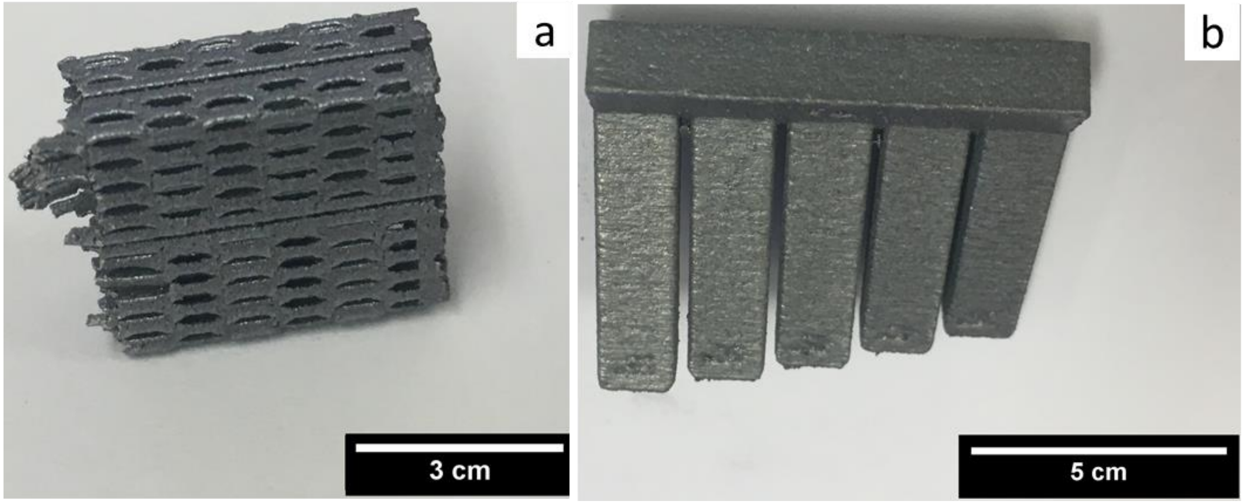

Figure 3.2. Support structures collected from Morf3D printed in different shapes.

3.2.1. Planetary ball milling (PBM)

To understand the effect of PCA on the morphology and yield of the milling process, PBM was used. The shredded support structures were milled in the PBM with 10 minutes of work, alternating with 5 minutes of rest, for 24 hours. The PCA content was varied with values of 0, 1, and 1.5 wt.%. The powders were sieved after 24 hours of milling to evaluate the yield of the process. The yield of the process was the ratio of powder smaller than 150 μm to the total powder. The morphology of the particles was investigated using scanning electron microscopy (SEM) using a FEI Quanta 3D microscope. To examine the effect of the ball size on the morphology, size, and yield of the process, three stainless steel ball sizes (1/4-inch, 3/8-inch, and 5/8 inch) were used. All experiments were performed under an argon atmosphere to prevent any oxidation during the milling process. The ball-to-powder (BPR) weight ratio was kept constant at 10 to 1. After understanding the effect of the ball size on yield, the larger ball size was chosen to continue the milling process. The milling process was continued for 42 hours. After each milling run a sieving process was performed to measure the yield of the process, and SEM micrographs were acquired. The aspect ratio (AR) and the particle size were calculated using the SEM micrographs. The AR is measured by dividing the smallest diameter of the particles by the largest diameter. The size of the particle is the diameter of a spherical particle that has the equivalent area as the particle observed in the micrograph.

3.2.2. Cryomilling

Although, high energy balls are used to break down the particles in both PBM and cryomilling, there are significant differences between these processes. The volume of the cryomilling jar in our study is larger than the jar used for PBM, which makes it more desirable to prepare powder in sufficient quantities for AM. For the cryomilling process, the BPR was increased to 30 to 1, which increased the probability of impacting particles in the process to increase the yield. Although the effect of PCA and ball size were determined in the PBM study, they could not be directly used in the cryomilling experiment. The diameter of the jars and whether an attritor is used change the kinetic energy of the balls. In this work, ¼ - and 3/8- inch balls were cryomilled for 10 hours. After each run, the particles were sieved, and the yield of particles in the range of 45-150 μm was calculated. Similarly, the morphology of the particles was investigated using SEM micrographs. To understand the effect of PCA on the process using 3/8-inch balls, PCA amount was varied, with values of 0.2 or 0.8 wt. %. The morphology and yield of the process were investigated. In addition, an X-ray diffraction pattern was acquired with a Rigaku SmartLab using a Cu kα filter to analyze the phases in the cryomilled powder compared with GA powder.

3.3. Results

3.3.1. Planetary ball milling (PBM)

PCA can prevent the excessive cold welding of the particles, limiting the formation of the larger particles. In Table 3.1, the processing parameters used to understand the influence of PCA on the size reduction and morphology of the particles are displayed. The results show that the increase in the amount of PCA increases the yield of the process significantly.

Table 3.1. The parameters used in the PBM of the support structures: RPM=Revolution per minute, BPR=ball to powder ratio, PCA=process control agent.

Sample ID	RPM	BPR	Run time (hr)	Ball size (inch)	PCA (wt. %)	Yield (<150 μm) (%)
P-1	300	10:1	24	¼	0	2.5
P-2	300	10:1	24	¼	1	18
P-3	300	10:1	24	¼	1.5	30

In addition to an increase in production of the amount of powder in the desired range, a change in the morphology of the particles was observed. As the amount of PCA increased, the number of fine and faceted particles increased. The SEM micrographs of particle morphology are shown in Figure 3.3, indicating the formation of enormous particles in the absence of PCA and an overabundance of fine particles when 1.5 wt.% PCA was used. Considering the yield of the process, 1.0 wt.% PCA was selected for further investigation.

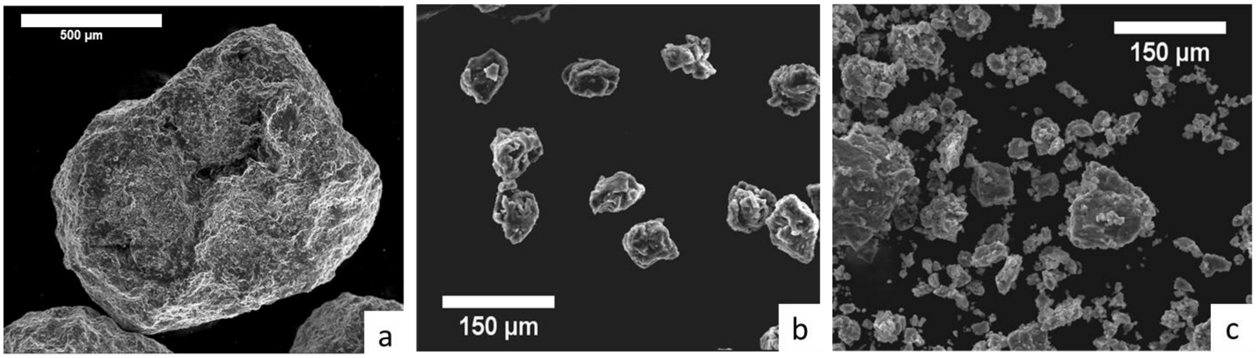

Figure 3.3. SEM micrographs of particles milled for twenty-four hours using a) zero percent PCA, b) one percent PCA, and c) 1.5 percent PCA.

The effect of the ball size was investigated by using three different stainless steel ball sizes (1/4-inch, 3/8-inch, and 5/8-inch). The amount of PCA and other processing parameters were kept constant, as displayed in Table 3.2.

Table 3.2. The parameters used in the PBM of the support structures with the focus on the influence of ball size on the yield: RPM=Revolution per minute, BPR=ball to powder ratio, PCA=process control agent.

Sample ID	RPM	BPR	Run time (hr)	Ball size (inch)	PCA (wt. %)	Yield (<150 µm) (%)
P-2	300	10:1	24	¼	1	18
P-4	300	10:1	24	3/8	1	24
P-5	300	10:1	18	5/8	1	30
P-6	300	10:1	42	5/8	1	75

The ball size has a definite impact on both the amount of powder produced in the desired size range and the morphology of the particles (Figure 3.4). The morphology of the particles was rock-like when milled with ¼-in balls and plate-like when milled with 5/8-inch balls. However, minimal differences were observed between the morphology of particles milled with ¼-inch balls and 3/8-inch balls as shown in Figure 3.4 (a) and (b).

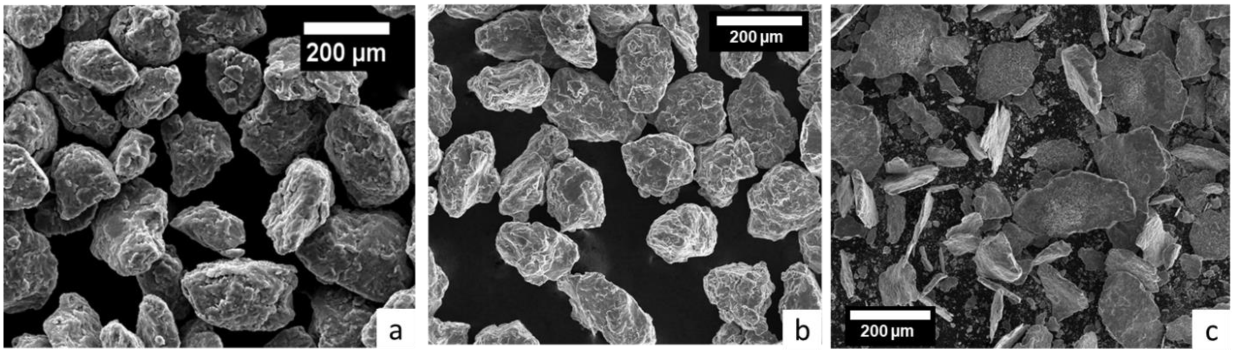

Figure 3.4. SEM micrograph of the particles milled with a) ¼-inch balls, b) 3/8-inch balls, and c) 5/8-inch balls.

In addition to the ball size and PCA, the milling duration has a significant impact on the yield and morphology. As displayed in Table 3.2, when the milling continues to 42 hours using 5/8-inch balls (Sample P-6), the yield of the process increases significantly. In fact, after milling for 42 hours, almost no large particles (larger than 500 μm) were observed in the powder. The change in the size of the particles during 42 hours of milling is illustrated in Figure 3.5. The results of particle size versus milling time show that in the first 6 hours of the milling process, a significant change in the size of the particles occurs. However, for the next 24 hours, almost half of the particles remained within the size of 150 – 500 μm, and the rest of the particles were larger than 500 μm. After 30 hours of milling, change in the size was again observed, with a significant decrease in the mass percentage of particles larger than 500 μm. After 42 hours of milling, approximately 75% of the particles were smaller than 150 μm. Another observation on the size evolution of the particles is that after 36 hours, the number of the particles in the range of 150-500 μm sharply increased, and after continued milling, the particles are broken down to finer particles. In addition to the high yield, particles milled for 42 hours showed a rock-like morphology (Figure 3.6 (a)). The higher magnification of the particles milled for 42 hours (Figure 3.6 (b)) shows that these particles are formed from a number of smaller particles welded together.

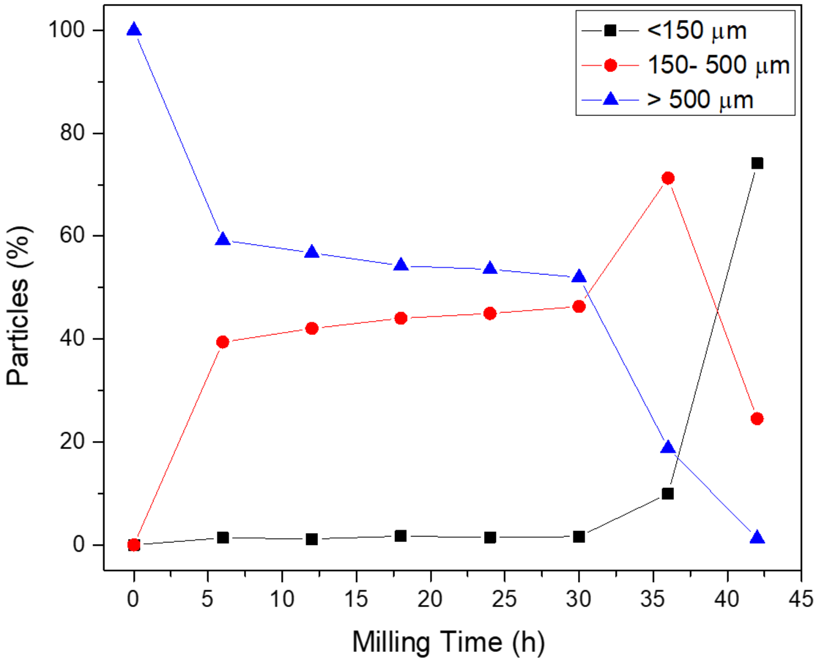

Figure 3.5. Particle size changes during 42 hours of milling.

The SEM micrographs show rock-like morphology for the particles collected after 42 hours of milling (Figure 3.6); however, the particle size and the AR of the particles are different from those of GA powder. The particles in the PBM powder are on average smaller compared to those in the GA powder, as shown in Figure 3.7 (a). The AR result also shows that the PBM particles are less spherical compared to GA particles, shown in Figure 3.7 (b).

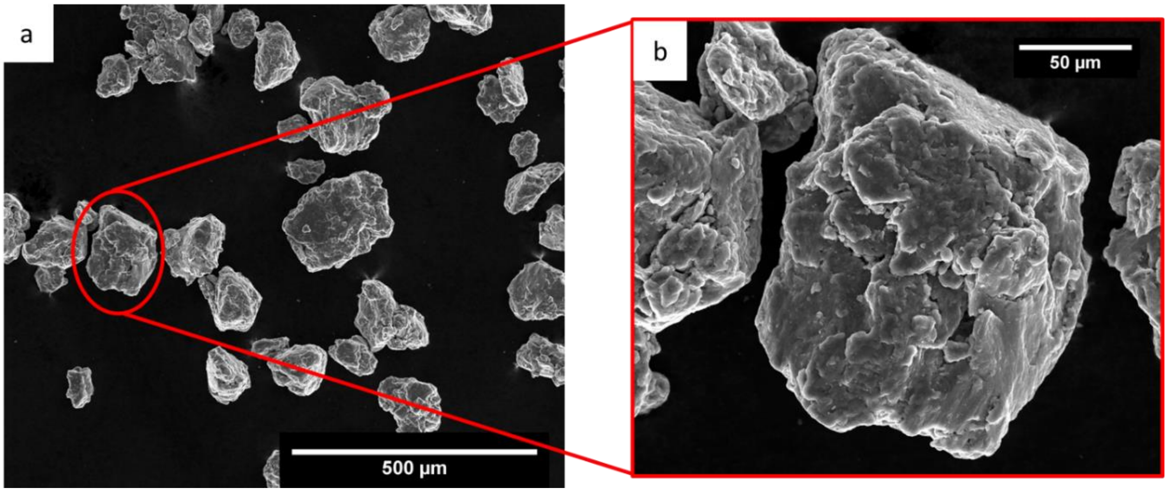

Figure 3.6. The morphology of the planetary ball milled particles (45-150 µm). b) higher magnification of one of the particles in (a). The particles looked rock-like; plate-like shaped particles were not observed.

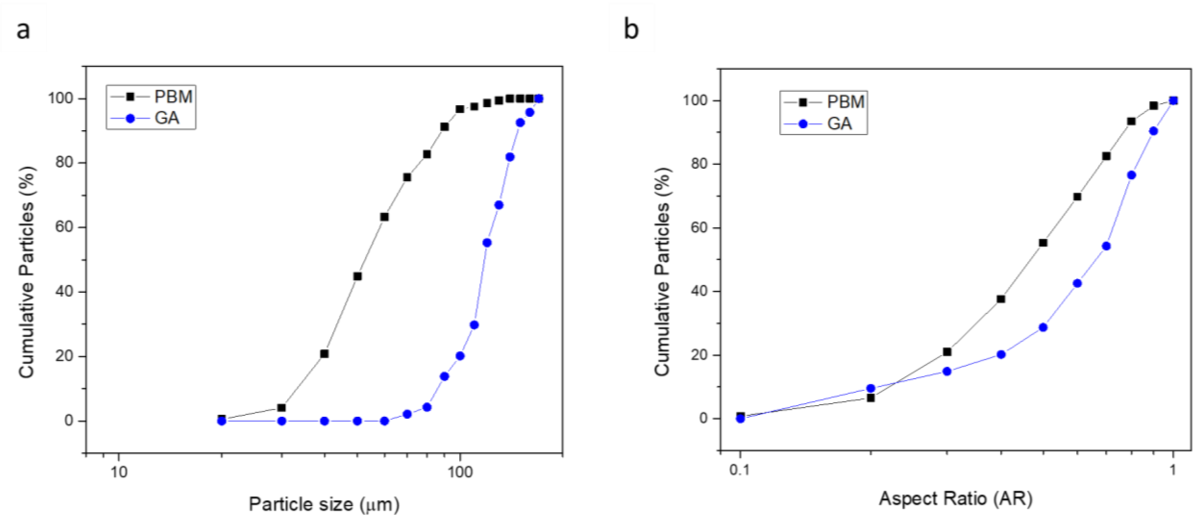

Figure 3.7. a) The AR (aspect ratio) of the particles produced after 42 hours of PBM vs. GA b) particle size of PBM vs. GA powders. (PBM= plantery ball mill; GA=gas atomized).

3.3.2. Cryomilling

The ball-to-powder ratio of 30:1 was used to reduce the required milling time in the cryomilling experiment. The effect of PCA and the ball size on the yield of the cryomilling process is summarized in Table 3.3. Similar to PBM, using larger balls increases the yield of the process and using a lower amount of PCA decreases the yield. Although the mass percentage of particles in the range of 45-150 μm is lower when a lower amount of PCA is used, as shown in Figure 3.8, the mass percentage of particles smaller than 45 μm increased significantly; meanwhile, the mass percentage of large particles decreased. The result shows that size reduction has been successfully performed on the particles using larger balls and a lower amount of PCA. The morphology of the particles was not affected by the ball size; however, the morphology became significantly more spherical when the amount of PCA was decreased (Figure 3.9).

Table 3.3. The processing parameters used for the optimization of ball size and the PCA used in the cryomilling process

Sample ID	RPM	BPR	Run time (hr)	Ball size (inch)	PCA (wt. %)	Yield (45-150 μm) (%)
C-1	500	30:1	10	¼	0.8	13
C-2	500	30:1	10	3/8	0.8	43
C-3	500	30:1	10	3/8	0.2	25

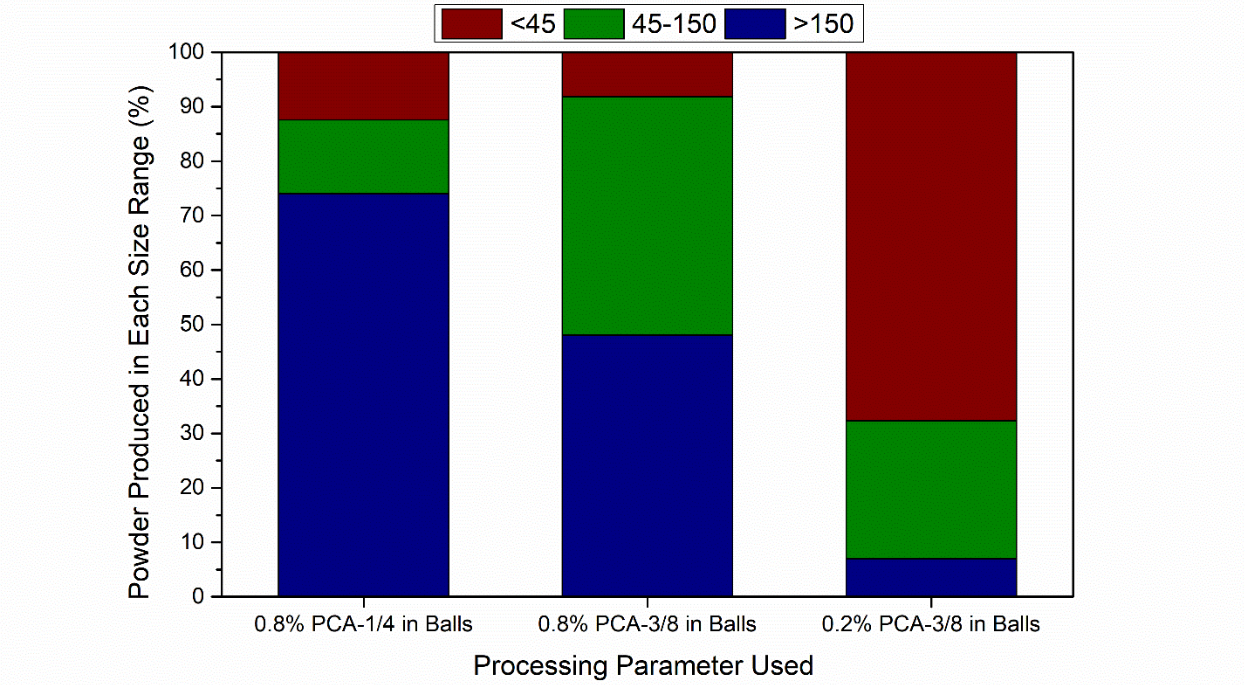

Figure 3.8. Shows the particle size distribution of powders produced in cryomilling using different processing parameters.

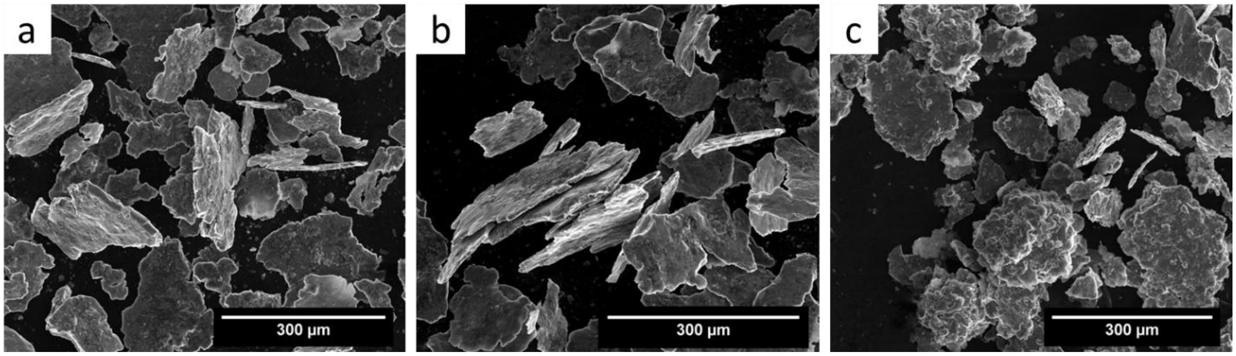

Figure 3.9. a) SEM micrograph of particles produced using 0.8 wt.% PCA and ¼-inch balls, b) SEM micrograph of particles produced using 0.8 wt.% PCA and 3/8-inch balls, c) SEM micrograph of particles produced using 0.2 wt.% PCA and 3/8-inch balls (PCA= process control agent).

In this experiment, the number of balls per unit volume in the vessel during the cryomilling process is higher than with PBM; this can increase the chance of contamination from the stainless steel balls and vessel. However, no significant phase change in the cryomilling powder was observed in the XRD pattern compared to GA powder as displayed in Figure 3.10.

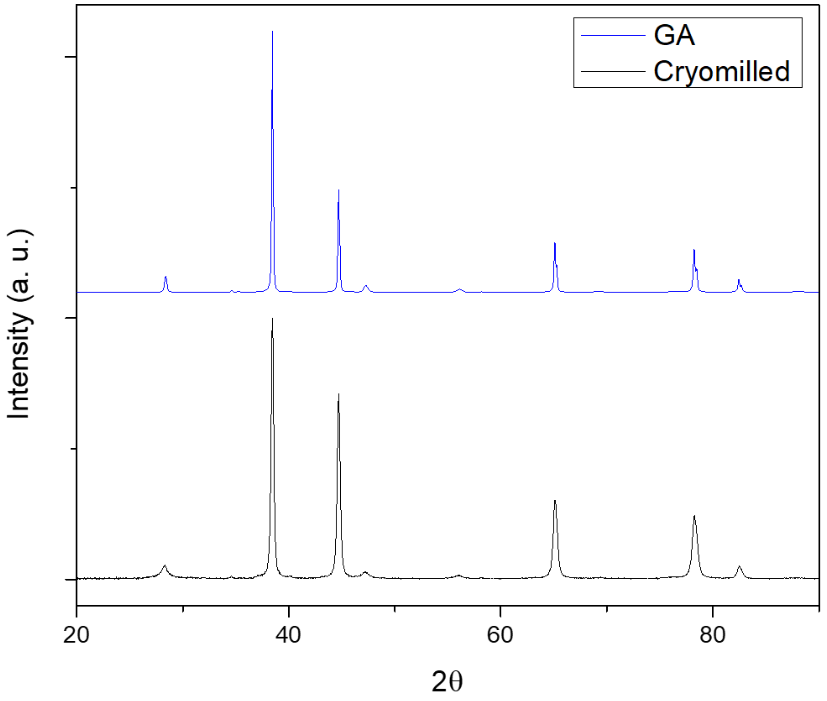

Figure 3.10. XRD pattern of powder cryomilled for 10 hours vs. GA powder. (GA= gas atomized).

The process parameter optimization successfully increased the yield and slightly modified the particle morphology in the cryomilling process. To test the printability of cryomilled powder in AM, the powder produced using process parameters of sample (C-3) in Table 3.3 was used to print U-shaped tracks in a custom built powder bed AM system. The results show that although the particles produced using lower PCA and larger balls show a smaller number of plate-like particles, they were not suitable to be used in this custom-built powder bed system. The results displayed in Figure 3.11 indicate that U-tracks deposited with GA powder (Figure 3.11 (a)) have a higher height and are more continuous compared to U-tracks deposited with the cryomilled powder (Figure 3.11 (b)).

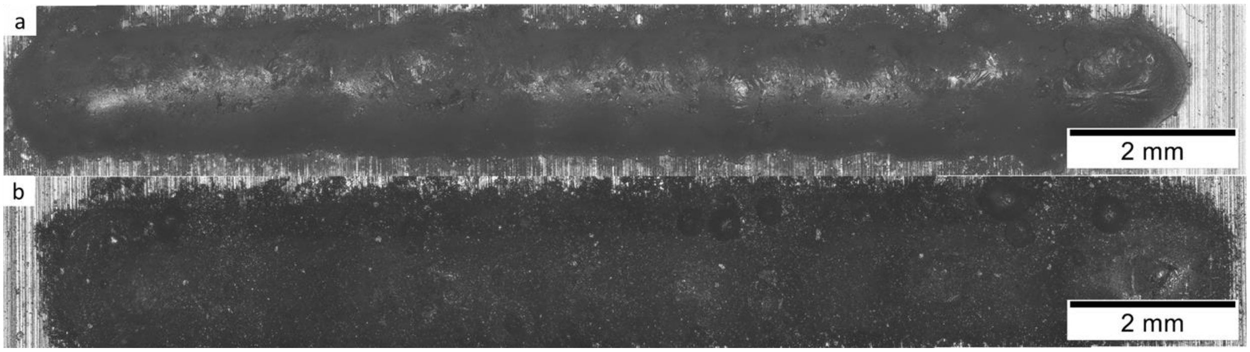

Figure 3.11. Single tracks deposited in a custom powder bed using a) GA and b) cryomilled powder. (GA= gas atomized).

3.4. Discussion

3.4.1. Planetary ball milling (PBM)

PBM is used for numerous purposes in the powder industry. It is mostly used to modify the microstructure of the particles, for mechanical alloying, and less often for size modification. PBM has also been used to produce powder for AM. Han et al. used PBM to prepare aluminum matrix composites for SLM [67]. They showed that increasing the milling time can provide particles with semi-spherical morphology. In high energy milling processes such as PBM, the particles can be welded together and form one large particle. This effect has been observed in our PBM powder with no PCA as well. Zhang et al. used a backpropagation neural network to predict the relationship between PCA and particle size during the milling [65]. Their result, backed up with experimental data, showed that by increasing the PCA from 0% to 1%, the particle size decreases from 40 μm to 27 μm. However, an increased amount of PCA can interfere with the milling process by minimizing the formation of larger particles from smaller particles. In our study, 1 wt.% PCA helped to increase the yield significantly; however, when a higher amount of PCA was used, particles were unable to weld together to form more rock-like particles. During the milling process two processes affecting particle size are simultaneously taking place: fusion of smaller particles together to form larger particles, and fracture of the larger particles to form smaller particles [68]. In fact, the right amount of cold welding and powder fracture is necessary to fabricate particles with the desired size and morphology. Micrographs displayed in Figure 3.3 show that there are a significant amount of very fine particles produced when 1.5 wt.% PCA was used, suggesting that a higher amount of PCA prevents welding of finer particles to each other. However, in 1 wt.% PCA, we can see that the larger particles mostly consist of smaller particles that were welded together (see Figure 3.3).

The effect of the ball size on the particles during the milling process has been previously demonstrated by many researchers. Shin et al. showed that increasing the ball size from 1 mm to 2 mm in wet ball milling significantly reduced the average particle size; however, increasing the ball size more than 2 mm increases the average particle size [69]. In their results, the 2 mm balls showed the optimum size reduction impact. The change in the ball size modifies the dynamic of the particle size reduction in two primary ways: 1) changing the total number of contact points between the balls and particles, and 2) changing the kinetic energy of the colliding balls. Our collaborators at the Colorado State University showed that larger balls increase the force on particles in every impact [25]. Increasing energy increases the probability of overcoming the tensile strength of the particle and breaking it into smaller particles. In addition, larger balls impact the particles deeper than smaller balls, making each impact more efficient in the particle size reduction process. Our results show that increasing the ball size increases the yield while producing more plate-like particles.

Using larger balls resulted in formation of more plate-like particles due to the ductile behavior of the particles. The larger size of the balls presses the particles more forcefully when they are between two balls or between the balls and the vessel’s wall. As the milling process continues for an extended time, welding and fracture of flattened particles increases the yield of the process to more than 70%. Although the morphology of the particles milled for 42 hours showed semi-spherical shape, as displayed in Figure 3.6, the milled particles show different particle size distributions and aspect ratios compared to the GA powder (Figure 3.7). Additional morphology modification should be used to improve the AR of the milled particles. Lower AR and particle size can cause a significant change in the flowability of the milled powder in AM. As described in Chapter 2. In this study, the milled powder was on average smaller than GA powder, which can increase the particle-to-particle friction and particle agglomeration, consequently affecting the flowability of the powder. In addition, the lower AR observed in the milled powder influences its compactibility. Powder with non-spherical shapes tends to pack less efficiently compared to spherically shaped particles. The compaction behavior, important in SLM systems, plays an important role in the part's height and porosity. In addition, compacted non-spherical powder usually does not easily initiate powder flow. The initiation of flow is crucial in the hopper discharge in both SLM and L-DED systems. However, experimental work is required to quantify the direct impact of these changes in the powder morphology on the quality of printed parts.

3.4.2. Cryomilling

Cryomilling has been successfully used in size reduction, grain refinement, and production of composite materials. However, this powerful technique mostly has been used for producing powder to be used with other consolidating techniques such as spark plasma sintering (SPS) rather than with AM. Cryomilling has proven very successful in producing a homogenous distribution of ceramics and metal powder to be used as a metal matrix. Although the use of this technique for reducing particle size has not been widely investigated, some studies mention this effect. De Lira et al. showed that the temperature, rotation speed, and ball-to-powder ratio play important roles in the particle size and crystalline size of milled pure Al particles [70]. They showed that the Al particles experienced an initial size increase followed by a size reduction with continued milling at room temperature. However, only reduction in the particle size was observed when the cryogenic temperature was used. Other studies, such as the study published by Badiola et al. in 2009, show that particle size distribution and average particle size significantly changed in PBM and cryomilling of 12Al.3CuO powder [71]. The cryomilled particles showed a significant increase in the particle size, whereas PBM powder showed a slight decrease in the average particle size. An increase in the size of Inconel 625 particles after cryomilling for 8 hours has also been reported [72]. The particle size distribution for Ti particles during cryomilling became broader as the milling time increased, and the average particle size increased from approximately 50 μm to 110 μm. In addition, the particle morphology changed from plate-like particles after 1 hour of cryomilling to rock-like particles after 6 hours of milling [73]. A significant change in the morphology and size of cryomilled pure Mg is reported by Wang et al. Their result showed that flat particles were seen at first, transitioning to a rock-like shape after cryomilling for 8 hours [74]. Although many of these studies have shown the increase in the size of the cryomilled particles, it is important to mention that the starting size of the particles in the current work and in the published works are very different. Most of the published works were focusing on using GA powder as the starting feedstock material, with particle size on the order of 100 μm; however, the size of the particles used in the current study is almost 10 times that size. The larger starting particles can be one reason that a reduction in particle size has been observed.

The effects of ball size and the amount of PCA on the yield and morphology of the particles have been shown in the cryomilled and PBM powder. However, as the milling media, ball-to-powder ratio, and the jar size are different in cryomilled and PBM process, optimization of the amount of PCA and ball size is required for each system. Larger balls in both milling settings increased the yield of the process due to changes in the kinetic energy of the balls. According to previously published work on cryomilling of Al alloys, using a high amount of PCA (1%) was not suggested due to the formation of highly faceted particles. Ye et al. showed that increasing the amount of PCA from 0 to 0.2 wt.% in cryomilling Al alloy with B_4C particles increases the material yield significantly; however, increasing the PCA amount to higher values does not increase the yield as much [75]. Similarly, our work showed higher yield when a higher amount of PCA was used. However, the main difference between the 0.2 wt.% and 0.8 wt.% PCA samples was the abundance of smaller particles when a lower amount of PCA was used. The lower amount of PCA and extended milling time can result in cold welding of these finer particles and the formation of larger particles in the desired size, which can be of interest for future work.

The result of AM deposition of U-shaped tracks using the cryomilled and GA powder showed significant differences. These differences can be traced back to the morphology and packing behavior of the cryomilled powder. Powder with non-spherical shape usually shows poor initial packing density. This is due to the fact that the particles are clinging to each other on the edges and as a result, there will be empty spaces between the particles. The empty space can result in lack-of-fusion pores in the samples. The empty space also affects the available material in the melt pool, resulting in lower buildup height of the tracks printed in AM. In addition, finer particles usually show lower flowability. This is due to their higher surface energy and higher number of particles. The fine particles have a hard time passing each other to fill the voids and increase the packing density.

3.5. Conclusions

Additive manufacturing (AM), as a promising technique for reducing the cost and waste of production, is potentially able to upcycle scrap material. The support structures printed during selective laser melting can be recycled in a solid-state recycling technique. In this work, a planetary ball mill and cryomill are used to produce particles smaller than 150 μm that can be used in different AM techniques. The amount of process control agent, ball size, and milling duration used in the planetary ball mill process have been varied to achieve this goal. The larger balls increase the yield of the process significantly. Although the addition of PCA to the milling media increases the efficiency, the addition of higher than 1.0 wt.% does not increase the yield nor improve the size reduction in a noticeable manner.

Cryomilling was used to produce powder in the size range of 45-150 μm, as a potential feedstock for AM processes. Cryomilling has many advantages compared to PBM, such as larger jars, which can increase the amount of powder produced in each run. In addition, using the cryogenic temperature shortened the milling duration. In this study, the PCA and ball size used in the cryomilling were optimized to increase the yield and alter the morphology. The result of this study showed that a higher amount of PCA will increase the formation of very fine particles, which is not desirable in AM. Larger balls, however, can increase the yield of the process significantly.

Chapter 4: Directed Energy Deposition of AlSi10Mg: Single Track Nonscalability and Bulk Properties

Abstract

Additive manufacturing of Al alloys presents an opportunity to produce complex parts that leverage their high specific strength. This chapter aims to study the effect of processing parameters on the fabrication of single tracks and thin walls using AlSi10Mg powder in L-DED. A processing window was identified to enable continuous single track deposition with a regular shape. Deposition of thin walls and single tracks were used as a guideline to deposit blocks. Blocks were deposited using L-DED, and the physical, microstructural, and mechanical properties of the samples were investigated. Results demonstrated that the morphology of the thin walls were a better indicator of the morphology of the block samples than single tracks were, and care must be taken when transitioning from depositing single tracks to bulk (thin walls and blocks) samples. Results from mechanical testing show slight inhomogenity as a function of height within the build for elongation and ultimate tensile strength. Microhardness and yield strength, however, were mostly uniform throughout the build. Overall, the results of this study demonstrate that L-DED is suitable for depositing AlSi10Mg and obtaining mechanical properties superior to those achieved through casting.

4.1. Introduction

Additive manufacturing (AM) has been widely used in recent years because of its ability to fabricate parts with unique microstructure and complex geometries. A wide range of metal alloys have been deposited using the LENS® system including and not limited to stainless steel [76], Ti [77], Al alloys [78], and Ni superalloys [79]. Al-Si alloys in particular have been extensively used specifically due to their low density, good mechanical properties, and low recycling costs [80]. However, material properties, such as high reflectivity (91%), high thermal conductivity (146 W m^{-1} K^{-1}) [81,82] and relatively low melting point (600°C), make processing Al alloys via metal AM more challenging [83]. Unfortunately, the high solidification shrinkage and solubility of hydrogen combined with the high coefficient of thermal expansion and wide solidification temperature range can change the weldability and behavior of these alloys in metal AM [84].

Deposition of parts in the laser directed energy deposition (L-DED) system will be affected by many processing parameters including but not limited to laser scan speed, laser power, and powder feedrate. Because of their simplictiy, studies of single track deposits are often used to explore the influence of processing parameters on sample microstructure and physical properties in metal AM, and to establish process condtions for larger builds [85–87]. These studies have evaluated mostly PBF parameters, yet one study investigated L-DED of pure Fe showing that similar process parameters could be used for both single tracks and bulk deposits [87]. For Al-Si-Mg alloys, there are various published studies on the relationship between microstructure and processing parameters, most of which are based on the PBF technique [12,81,88–90]. Previously published studies on the deposition of bulk AlSi10Mg using L-DED also generally focus on processing parameter optimization, mechanical behavior characterization, and heat treatment [45,91,92]. Javidani et al. evaluated the feasibility of depositing bulk AlSi10Mg with L-DED; variations in the hardness and microsturcture in the L-DED deposited samples were observed [45]. Wang et al. investigated the effect of scan speed and chamber oxygen concentration on the pore formation and consequently the mechanical properties of AlSi10Mg walls deposited in L-DED [91]. To the authors' knowledge, the relationship between single tracks and bulk (thin wall and block) samples deposited in a L-DED system for AlSi10Mg has not been investigated. To fill this knowledge gap, this work aims to investigate the effect of processing parameters on deposition of single tracks, thin walls, and block samples. Specifically, the processing window for depositing AlSi10Mg single tracks was defined by looking into the morphology and melt pool size. The scalability between single track, thin wall, and block processing conditions were examined. Successful deposition of block samples allowed for an investigation into the microstructure and tensile behavior.

4.2. Experimental procedure

AlSi10Mg gas atomized powders were purchased from Valimet Inc. in the particle size range of 46-150 μm. A LENS® 1000 workstation was used to deposit single tracks, thin walls, and blocks on a 6061 Al (Cu 0.15-0.4 wt.%, Fe max 0.7 wt.%, Mg 0.8-0.12 wt.%, Mn max 0.15 wt.%, Si 0.4-0.8 wt.%, Ti max 0.15 wt.%, Cr 0.15-0.4 wt.% Al bal.) substrate. The chamber was thoroughly cleaned before each deposit to prevent any cross contamination, and the oxygen concentration was kept below 20 ppm for the entire deposition process. The combination of different laser power values (400, 500, 600, 700, 800, and 900 W), laser scan speeds (4.2, 10.5, and 16.9 mm/s) and powder feedrate settings (1.8, 2.0, and 2.2 rotation per minute (RPM)) were used to deposit fifty-four single tracks. The powder flowrate in g/s was recorded by measuring the amount of powder going through the LENS® system in a fixed amount of time, while the powder feedrate setting was kept constant. The tracks were characterized by visual inspection using an Olympus BX53M optical microscope (OM) to determine the integrity of each combination of deposition parameters. A Mitsubishi model F020S wire electric discharge machining (EDM) system was used to cut cross sections of the single tracks. Cross section samples were polished metallographically with SiC papers (600 to 1200 grit size) using an auto polisher (Buehler

AutoMet 250) followed by manually polishing down to 1 μm using diamond suspension. Thirty-six thin wall samples (1.27 cm x 1.27 cm x 0.5 mm) were deposited with two scan speeds (4.2 and 16.9 mm/s), three different powder feedrates (1.8, 2.0 and 2.2 RPM), and varying laser power from 400-900 W. The layer increment was 0.304 mm for all the thin walls. The macroscopic quality of the thin walls was investigated by examining their size and shape relative to the target dimensions in the CAD model. Several horizontal blocks were deposited using laser power as a variable (500 W, 600 W, 700 W), a scan speed of 16.9 mm/s, and a powder feedrate of 2 RPM. The hatch increment, layer increment, and laser spot size used were 0.406, 0.304, and 1.2 mm, respectively. The blocks were designed to be 3.81 cm x 1.01 cm x 1.01 cm in size. Only the three blocks deposited with laser power = 600 W were of high quality and were, therefore, used for further characterization. Five dogbone samples were cut from each block using wire EDM, following the dimensions outlined in Figure 4.1 (a) [43]. A separation of 0.5 mm was used between each dogbone, as seen in Figure 4.1 (b). In this work, the dogbones are labeled 1, 2, 3, 4 and 5, where 1 is the closest to the substrate and 5 is closest to the top of the block. Additional samples were also cut from the block parallel to the build direction, as shown in Figure 4.1 (b), and were used for microstructural characterization. These samples were manually polished to 1 μm diamond and etched with Keller's reagent for 12 seconds.

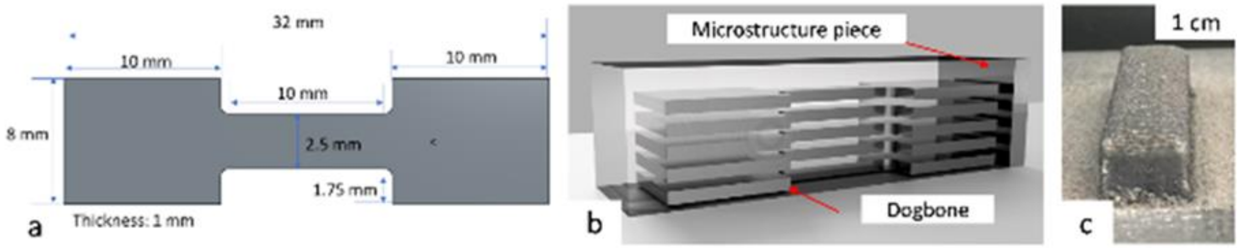

Figure 4.1. a) the geometry of the dogbones cut for the tensile tests (the dogbone radius is 1 mm). b) schematic showing the location of dogbones and sample used for microstructural characterization relative to the L-DED AlSi10Mg build geometry. c) photograph of an L-DED AlSi10Mg block deposited for tensile tests.

A FEI Quanta 3D scanning electron microscope (SEM) equipped with energy dispersive X-ray spectroscopy (EDS) was used to analyze the microstructure and chemical composition of the various samples. X-ray diffraction (XRD) was performed on polished samples with a Rigaku SmartLab diffractometer using a Cu k_α filter to analyze the phases in the virgin powder and the blocks. Archimedes' principle was used to measure the density of the block samples in ethanol at room temperature [93]. All tensile tests were performed using an Instron 8801 load frame equipped with a 100 kN load cell and a video extensometer to resolve axial strain with a nominal strain rate of 0.001 s^{-1}. Vickers microhardness tests were performed using a Struers Duramin 5 instrument by applying 9.81 N load for 15 s. Microhardness tests were performed on a vertical sample, cut from the original block sample, with the testing surface parallel to the build direction. A total of 50 different locations (5 rows of 10 indents) were systematically tested in one of the blocks to analyze the microhardness.

4.3. Results

4.3.1. Single tracks

OM images of single tracks can be used to examine their integrity. It is noticeable that both the laser power and scan speed have a significant impact on the stability of the single tracks. The morphologies of eighteen representative single tracks, deposited with three different scan speeds (4.2 mm/s, 10.5 mm/s, 16.9 mm/s) and six different laser powers (400-900 W) while keeping the powder feedrate constant (2 RPM), are shown in Figure 4.2 . A red border in Figure 4.2 represents an unsuccessful single track. A yellow border represents continuous single tracks with irregular shapes. A green border shows continuous and regular shaped single tracks. The single track with a white/black border is deposited with the same parameters used for the block deposits. The cross sections of all fifty-four single tracks (not shown) exhibit an oval shape; a keyhole melt pool shape was not observed in any of the deposited tracks.

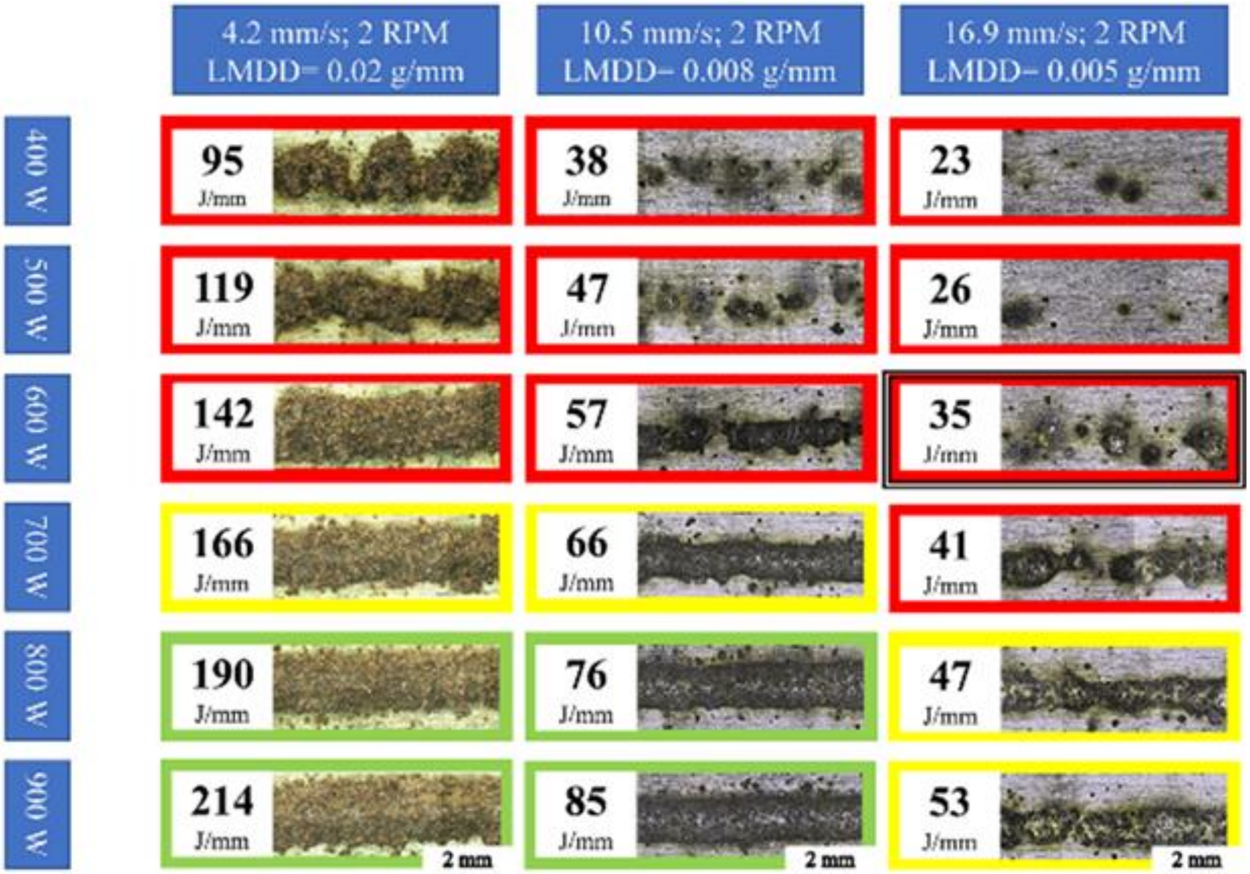

Figure 4.2. Optical micrographs of L-DED AlSi10Mg single tracks deposited using different scan speeds (mm/s) and laser powers (W). The powder feedrate for all tracks was two revolutions per minute (2 RPM).

Powder feedrate can also affect the morphology, shape, and size of the single tracks. Figure 4.3 shows the morphologies and cross sections of single tracks deposited with laser power of 700 W and scan speed of 10.5 mm/s, while varying the powder feedrate from 1.8 RPM (Figure 4.3 (a)), to 2.0 RPM (Figure 4.3 (b)) and 2.2 RPM (Figure 4.3 (c)). As powder feedrate increases, the shape of the single track becomes more uniform, the track height increases, and the penetration into the substrate decreases. The same behavior has been observed in single tracks deposited with different laser power and scan speed values.

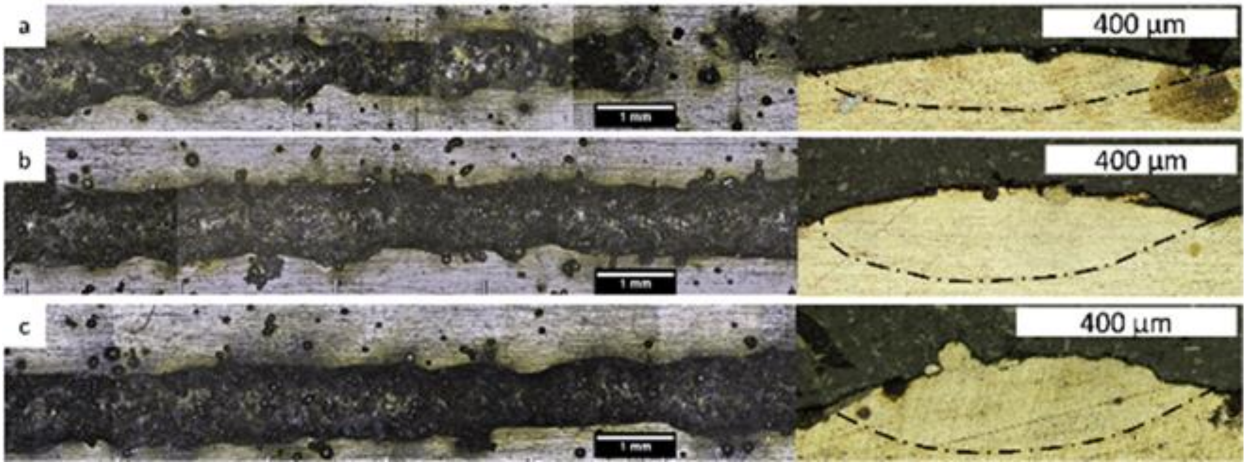

Figure 4.3. Optical micrographs showing a bird's-eye (left) and cross section (right) view of single tracks deposited with 10.5 mm/s scan speed and 700 W laser power. Powder feedrate was varied: a) 1.8 RPM (LMDD=0.006 g/mm), b) 2.0 RPM (LMDD=0.007 g/mm), and c) 2.2 RPM (LMDD=0.01 g/mm).

4.3.2. Thin walls

The deposited thin walls showed a range of morphology, surface finish, size, and porosity depending on laser power and scan speed, as noted in Figure 4.4, and observed in the photographs of representative samples shown in Figure 4.5. The red cells in Figure 4.4 represent the thin walls with dimensions that differ from the designed dimensions and the yellow cells represent the thin walls with poor surface finish and high porosity. Eleven parameter combinations presented in Figure 4.4 indicate that increasing the laser power resulted in larger thin walls. Lower scan speeds resulted in taller and wider thin walls. Increasing the scan speed resulted in thin walls that were closer in size and geometry to the target dimensions. Thin walls deposited with powder feedrates lower or higher than 2 RPM showed lack of growth or extensive growth. A laser power of 600 W and a scan speed of 16.9 mm/s were the optimal parameters for depositing thin walls with minimal porosity and high dimensional accuracy (highlighted in green in Figure 4.4).

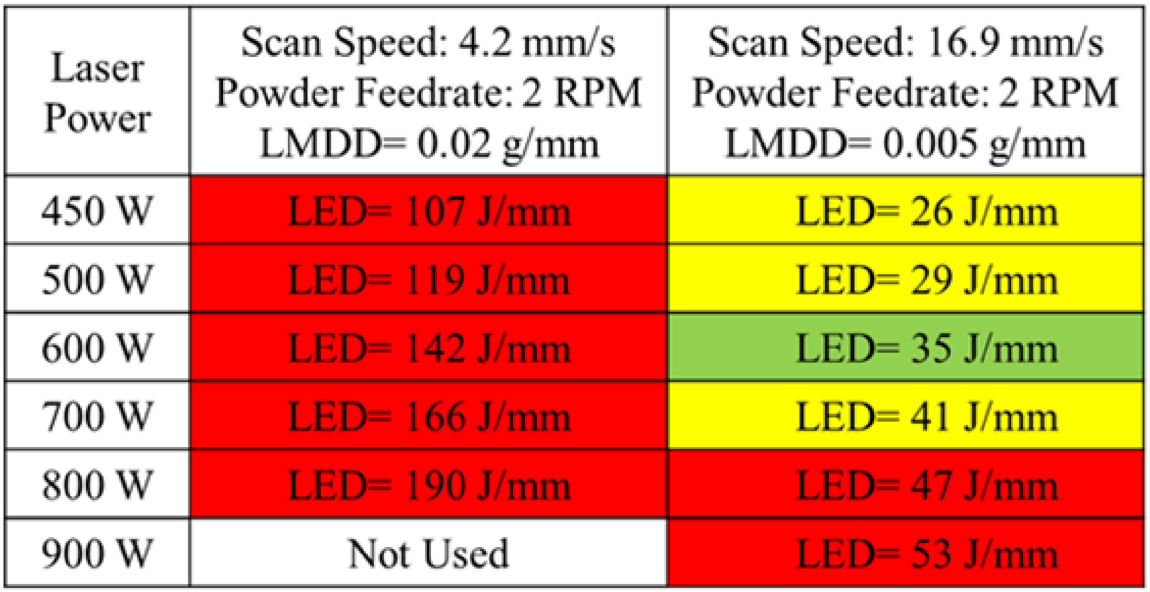

Laser Power	Scan Speed: 4.2 mm/s Powder Feedrate: 2 RPM LMDD= 0.02 g/mm	Scan Speed: 16.9 mm/s Powder Feedrate: 2 RPM LMDD= 0.005 g/mm
450 W	LED= 107 J/mm	LED= 26 J/mm
500 W	LED= 119 J/mm	LED= 29 J/mm
600 W	LED= 142 J/mm	LED= 35 J/mm
700 W	LED= 166 J/mm	LED= 41 J/mm
800 W	LED= 190 J/mm	LED= 47 J/mm
900 W	Not Used	LED= 53 J/mm

Figure 4.4. Parameters used in L-DED AlSi10Mg thin wall deposits.

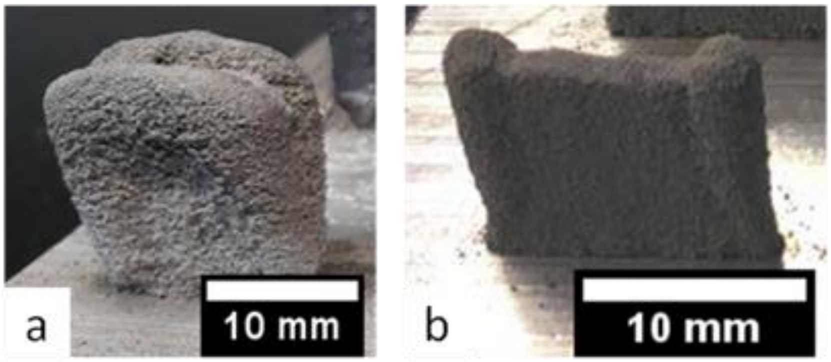

Figure 4.5. The morphology of two representative L-DED AlSi10Mg thin walls: deposition parameters were: a) 600 W, 2 RPM, 4.2 mm/s b) 600 W, 2 RPM, 16.9 mm/s.

4.3.3. Blocks

The block samples that were deposited using the optimal thin wall processing parameters, noted in Figure 4.4, exhibited good surface finish, uniform shape, and no discoloration on the surfaces, as illustrated in Figure 4.1 (c). These blocks were selected for further study. The measured dimensions of the blocks after deposition were very close to the target dimensions (3.86 ± 0.01) cm x (0.86 ± 0.03) cm x (1.09 ± 0.03) cm. Archimedes density measurements indicate that all samples were fully dense, 99.3% ± 0.3, compared to a theoretical density value of 2.68 g/cm^3 [45].

The XRD measurements, presented in Figure 4.6 for both the starting powder and one of the blocks, indicate the presence of Al, Si, and small peaks of Mg_2Si in both samples. No additional extraneous peaks are detected in either the powder or the block. Additionally, minimal differences are observed between the XRD pattern of the powder and that of the block, indicating that the phase state of the starting powder was preserved after deposition.

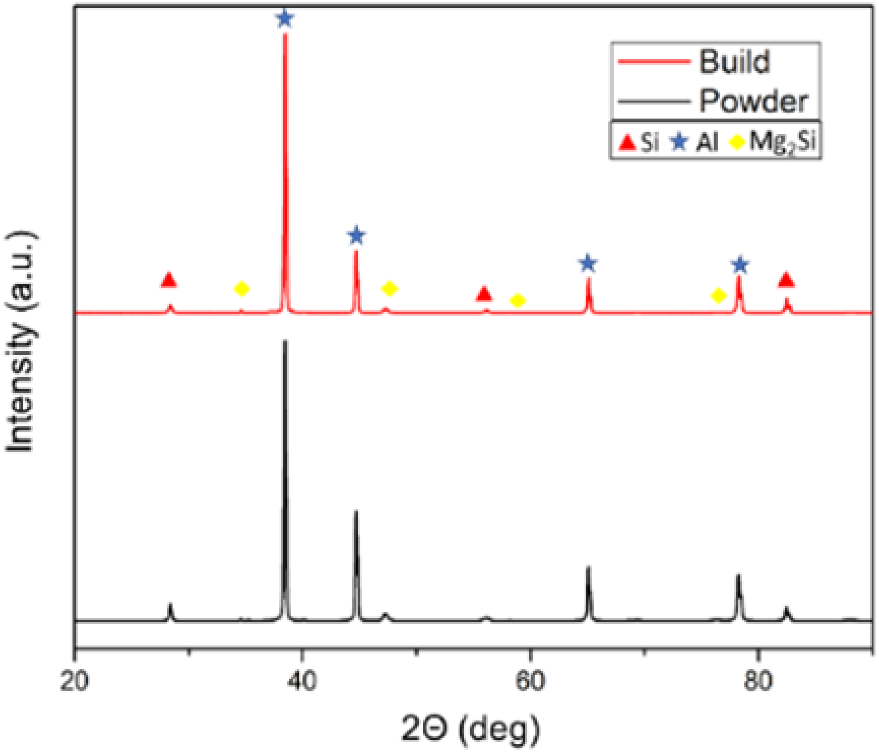

Figure 4.6. XRD patterns for the AlSi10Mg powder and L-DED AlSi10Mg block sample.

EDS analysis of the deposited block shows Al and Mg are uniformly distributed throughout the sample, as presented in Figure 4.7. In contrast, segregation of Si was observed at the cell boundaries.

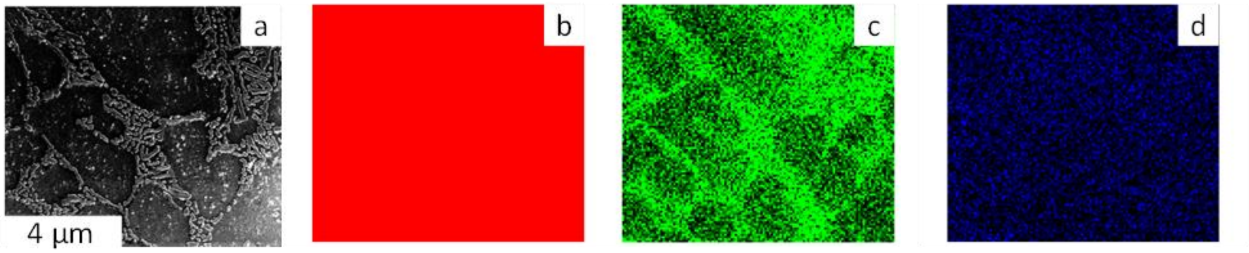

Figure 4.7. a) SEM image of the etched surface from the L-DED AlSi10Mg microstructure characterization sample. EDS elemental maps showing the distributions of: b) Al, c) Si, and d) Mg in the deposited block.

An etched surface was used to analyze the microstructural evolution along the build direction (Figure 4.8). Figure 4.8 (a) shows the change in the microstructure in two subsequent layers. The cellular structure is visible in the 'previous' layer, transforming to the heat affected zone (HAZ) and to a dendritic microstructure in the 'new' layer. Figure 4.8 (b) and (c) show the presence of the Al matrix (darker color) and the concentration of the Si/α eutectic (lighter color) in the cellular boundaries. Figure 4.8 (b) displays a representative microstructure of the region near the top of the sample, and Figure 4.8 (c) shows a representative microstructure of the region closer to the substrate.

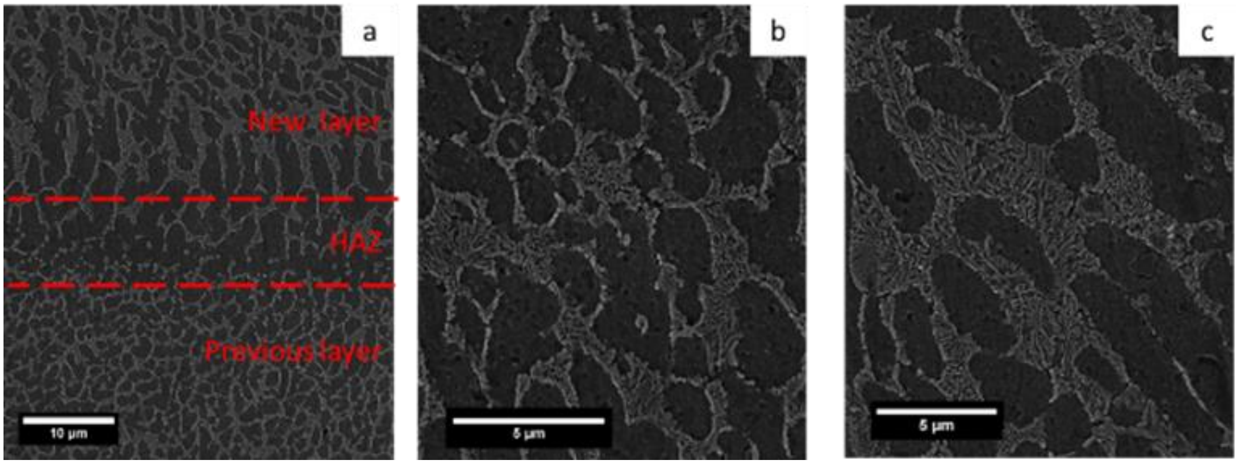

Figure 4.8. SEM micrographs showing the microstructure of the: a) two subsequent layers, b) top and c) bottom of the L-DED AlSi10Mg block. The build direction is from bottom to the top of the micrographs. The light regions are the Si/α eutectic, and the dark regions are Al matrix. Note the differences in scale.

The tensile properties of the blocks exhibit minimal changes along the build direction. Figure 4.9 (a) and (b) provide a summary of the elongation to failure, ultimate tensile strength (UTS) and yield strength in the tensile samples from the bottom of the block to the top, averaged for all three blocks. The average values of the tensile test and the microhardness are provided in Table 4.1. A slight decrease in the value of microhardness was seen by comparing measurements closer to the top of the sample with measurements closer to the substrate (Figure 4.9 (b)), but the values all remain within a standard deviation of each other.

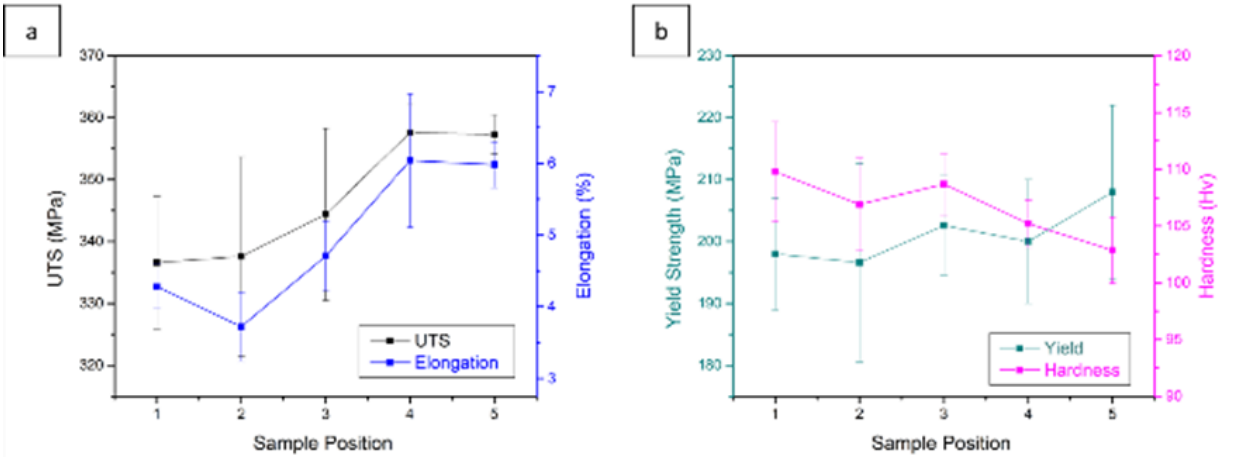

Figure 4.9. Location dependence of mechanical behavior in L-DED AlSi10Mg blocks. a) elongation to failure and ultimate tensile strength (UTS), b) yield strength, and Vickers microhardness of dogbones 1, 2, 3, 4, and 5. The error bars in UTS, yield strength, and elongation represent the standard deviation from three blocks. The microhardness error bars represent the standard deviation for the multiple indentations in one block sample.

Table 4.1. Average mechanical test results for L-DED AlSi10Mg blocks.

Mechanical Properties	This Work	SLM [90]	SLM + Aging [83]	Conventional Cast and Aged [83]
Ultimate Tensile Strength (MPa)	344 ± 16	425.25 ±10.7	399 ± 7	300-317
Yield Strength (2% offset) (MPa)	200 ± 10	322.17 ±8.1	--	-
Elongation (%)	5 ± 1.0	5.3±0.22	3.3 ± 0.4	2.5-3.5
Microhardness (HV)	107 ± 4	132.55±5.3	152.5 ± 5	86

Despite the high relative density of the blocks, pores with two different shapes and sizes were observed in the cross section of the deposited blocks, as shown in Figure 4.10. Large pores with a length ranging from 40 to 300 μm were concentrated along the first few deposited layers and between different tracks (Figure 4.10 (a)). Unmelted particles were trapped in some pores, as observed in Figure 4.10 (b). These elongated pores with irregular shapes are categorized as lack-of-fusion (LoF) pores. The number and size of LoF pores appear to decrease from the bottom of the sample to the top. Small pores were observed throughout the deposited sample especially at locations far from the substrate. These pores were more spherical with sizes ranging from 2 to 45 μm (Figure 4.10 (c)). Small spherical pores commonly result from gas entrapped in the build during deposition or in the feedstock gas atomized particles. Similar pore structures were observed in the fracture surfaces (Figure 4.11 (a) and (b)). The dimples are also observed in the fracture surface, consistent with the ductile deformation response. A higher magnification image of a LoF pore at the fracture surface is provided in Figure 4.11 (c).

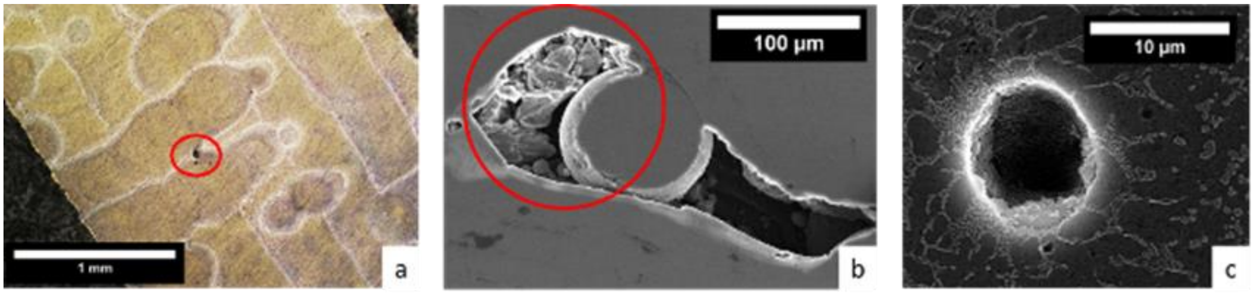

Figure 4.10. Micrographs showing the different shapes of the porosity observed in the L-DED AlSi10Mg blocks. a) Optical microscopy image showing track boundaries; a pore between tracks is highlighted. b) SEM micrograph showing irregular pores that were observed close to the substrate. Unmelted particles are highlighted inside the pore. c) SEM micrograph showing spherical porosity that was observed close to the top of the build.

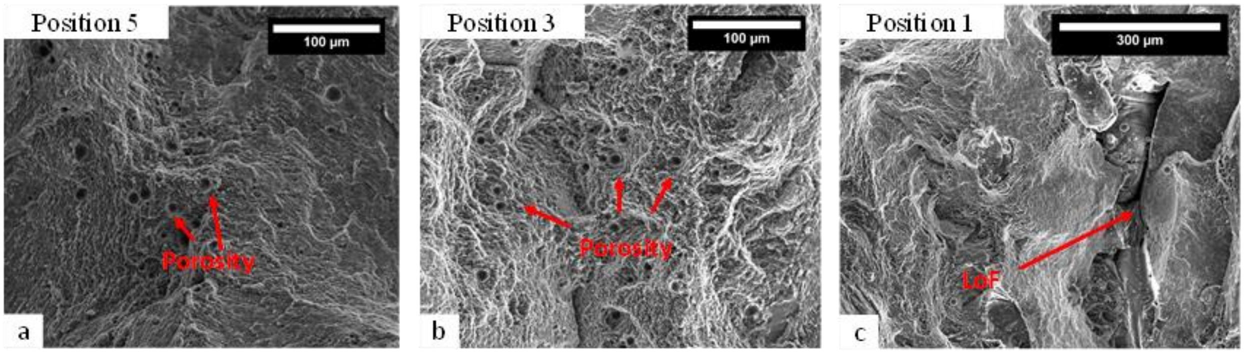

Figure 4.11. SEM micrographs highlighting specific features found on the fracture surfaces of the L-DED AlSi10Mg dogbone samples: a) dimples and porosity for position 5, b) cleavage. fracture and spherical porosity for position 3, and c) lack of fusion (LoF) pores and cleavage fracture in position 1 (bottom of the build).

4.4. Discussion

4.4.1. Single track deposition

Buchbinder et al. suggested to increase the laser power to overcome some of the issues associated with the high reflectivity and high heat conductivity of Al alloy deposits [94]. Similarly, there are a number of studies that use high laser power (1900-3600 W) to deposit AlSi10Mg using L-DED [95–97]. However, these studies deposit samples with significant inhomogeneity in the microstructure, leading to variability in the microhardness values throughout the build. In the current study, a range of acceptable combinations of laser power and scan speed were identified to produce single tracks with uniform morphology (continuous semi-cylindrical shape). The colormap used in Figure 4.2 shows three categories of single track morphology. Single tracks presented with a red border were unable to form a continuous track using the parameters indicated. A yellow border represents parameters leading to single tracks that do not have a regular cylindrical shape. Balling, which is the formation of a ball of material on top of the substrate or previous layer [85], was also observed in the single tracks in this category. The green borders highlight parameters that enable continuous single track deposits with regular cylindrical shapes. The quality of the single track morphology, i.e., continuity and cylindrical shape, is improved as the laser power is increased while keeping the powder feed rate and scan speed constant. In contrast, increasing the scan speed when keeping the other parameters constant results in a decrease in the height and an increase in the irregularity in the morphology of the single track. These irregularly shaped single tracks formed when the energy was low, and a series of disconnected beads were deposited instead of a continuous single track. Laser power values lower than 800 W do not provide sufficient energy to melt the particles and create a stable melt pool that continues throughout the track. The need for high laser power to successfully deposit Al is expected and is commonly attributed to the high reflectivity of Al and the interference from the passivation layer [98].

A commonly used metric to assess the energy delivered to the track is the linear energy density (LED) (J/mm), which scales to the ratio of: $\frac{P}{v}$ [99], where P is laser power in W and v is scan speed in mm/s. The calculated LED values for the single tracks shown in Figure 4.2 highlight that the quality of the tracks improve as you move to the bottom left hand corner of the diagram, which is where the LED values are higher. However, the data also show that LED is not sufficient to predict track quality, as values as high as 142 J/mm led to poor quality yet values as low as 76 J/mm led to good quality. Low laser power does not provide enough energy to melt the substrate and particles, so a continuous single track cannot be deposited. Balling can also be seen in some of the single tracks with lower laser power and lower scan speed. Therefore, LED alone does not directly predict whether the formation of a continuous single track will be successful. This is not only because of the inherent limitations of the LED values (e.g., it is not based on physical phenomena), but this measurement also does not include the effect of powder feedrate, which is important in L-DED techniques. This observation is consistent with other published work. As

Scipioni Bertoli et al. showed, the Volumetric Energy Density (VED) cannot properly predict melting conditions and single track morphology in L-PBF of stainless steel [100].

The powder feedrate affects the quality of the deposits and can change the processing window. Increasing powder feedrate increases the amount of material available in the melt pool and subsequently may increase the dimensions of the single track. The available material in the melt pool can be expressed by introducing another metric, linear material delivery density (LMDD), calculated as $\frac{F}{v}$ (g/mm), where F is powder flowrate (g/s) and v is scan speed (mm/s) [101]. This parameter corresponds to the amount of material delivered per unit length of the track. Higher values of LMDD indicate that more particles are introduced into the melt pool and the available energy could be used to melt more particles into the track. Consequently, the powder capture efficiency and the size of the melt pool are increased. However, increasing the feedrate beyond an optimum point results in a reduction of the powder capture efficiency due to an increase in the number of floating particles on the melt pool surface that deflect incoming particles, as Haley et. al. explained in their study [102]. High LMDD values are required to provide enough material in the molten pool for deposition of high-quality single tracks, i.e., continuous single tracks. On the other hand, high LED values are needed to provide enough energy to melt the powder particles and cold substrate to create the melt pool. Figure 4.3 shows that as LMDD increases, the shape of the single track becomes more uniform. Moreover, the cross section of the single tracks show that the height of the single track increases as LMDD increases, while the penetration depth to substrate decreases with increasing LMDD, indicating that some compromise exists between single track uniformity and dimensions with respect to increasing LMDD.

Based on the aforementioned observations, the effect of processing parameters on the single track morphology is summarized as follows. Increasing the powder feedrate while keeping the laser scan speed and power constant improves single track integrity and surface finish, as shown in Figure 4.3. High laser power and low scan speed can cause the balling of material on the surface of the substrate with minimal wetting (penetration of the melt pool into the substrate). The surface energy of a spherical molten material is lower than the surface energy of a semi-cylinder of material such as a single track [103]. With high scan speed and low laser power, there is not enough energy available to melt all the particles completely to achieve a uniform track shape. The resulting balling of material is poorly connected to the previous layers, and the track is often noncontinuous. Besides the processing parameters investigated in this study, other processing parameters such as carrier gas flow rate, layer increment, hatch spacing, etc. are known to affect the deposition behavior; a comprehensive investigation into the effect of all of these parameters, although outside of scope of the current study, would provide valuable insight into L-DED of metal systems.

4.4.2. Thin wall deposition

Thin walls deposited using the processing window feasible for successful single track deposition generally displayed poor surface finish, inaccurate dimensions, and high porosity. Figure 4.4 shows the processing parameters used for the thin walls and the corresponding values of LED and LMDD. The red cells in Figure 4.4 represent the thin walls that exhibit high volume of pores and have dimensions that significantly deviate from the target values. The results of this study indicate that high laser power and low scan speed are not required to successfully deposit AlSi10Mg thin walls. Lower scan speed (high LMDD) resulted in thin walls with larger height and width than the target dimensions, while increasing the laser power made the walls larger in width, height, and length. Increasing the scan speed to 16.9 mm/s (lower LMDD) made the geometry of the thin walls closer to the target dimensions and improved the surface finish.

However, increasing the laser power led to asymmetric shape of the thin walls, with the top of the wall being larger than the bottom. The yellow cells in Figure 4.4 highlight the parameters that produce thin walls with sizes close to the target dimensions but with discontinuities in the shape of the thin wall, along with high porosity. The green cell shows the parameters that resulted in the best thin wall in terms of size and morphology. The inaccuracy in geometry of the thin walls with high LMDD can be due to a higher concentration of particles per unit length, which enlarges the dimension of the individual thin walls. High energy densities are not desirable for thin walls due to formation of steep thermal gradients in each layer that increase the possibility of creating keyholes in the deposits. The thin wall deposits demonstrate a LMDD and LED processing window that is reversed from the requirements for processing successful single tracks. However, both sample geometries possess a narrow multivariate processing window for producing successful samples. LED, or any single processing metric, is insufficient to describe the conditions necessary for producing successful AlSi10Mg parts of any geometry.

4.4.3. Block deposition

Yadroitsev et al. showed that single track morphology can determine the properties of the parts and that surface stability may influence the formation of porosity in the build [85]. The morphology of single tracks can be varied by changing deposition parameters such as laser scan speed and power as was seen in other studies [12,102]. The parameters that lead to balling in single tracks can often cause defects when they are used to deposit blocks. These defects include porosity, micro-cracks, and poor surface finish [104]. Although a single track may commonly be used as a guide for choosing a set of parameters for a bulk deposit, this is not the case for L-DED of AlSi10Mg in this study.

Based on the thin wall deposition experiment, it was found that successful thin wall deposits could be achieved using a laser power of 600 W, a scan speed of 16.9 mm/s, and a powder feedrate of 2 RPM. The blocks deposited with these parameters were successful as well; however, the single track deposited with the same set of parameters as the bulk sample, as shown in Figure 4.2 and highlighted with the black and white frame, does not show a good surface finish nor morphology. Although the blocks deposited based on the optimal thin wall processing parameters were fully dense with high dimensional accuracy, the physical and microstructural features between thin walls and blocks were slightly different. This difference is due to the effect of geometry on the thermal history and temperature gradient during deposition. It is noteworthy to mention that the dimensional accuracy of the single tracks is not comparable to that for the block. This variation in dimensional accuracy between the single tracks and the blocks can be explained by the amount of available energy at each point in a bulk deposition versus that in a single track. Zheng et al. showed that in the LENS® system, as the number of layers increases the temperature of the melt pool increases, while the cooling rate decreases [105]. In addition, the optical and thermophysical properties of the Al varies with temperature. Darla et al. showed that thermal conductivity and laser reflectivity of pure Al decreases significantly at elevated temperatures [106]. Thus, the temperature increase caused by the heat accumulation of multi-layer deposition will decrease the thermal conductivity and laser reflectivity of the melt pool, further increasing the energy stored and reducing the energy needed for subsequent deposition. In other words, the LED required for deposition of upper layers in blocks and thin walls is lower than that needed to deposit single tracks.

Although the parameters needed to deposit high-quality (i.e., continuous) single tracks do not translate to the parameters needed for highly dense bulk samples, the parameters for thin wall deposition did translate well into those needed for larger blocks. A thin wall study produces processing parameters that are more scalable than a single track study, while still being more efficient and economical than performing a similar study on block deposits. Using thin walls to explore the processing parameter space will be particularly useful for materials that have not been extensively studied using L-DED. However, more experimental work on thin wall deposits is required to determine the process parameter scalability in other alloy systems beyond the AlSi10Mg studied here. However, some features in the single tracks do translate to the bulk deposits. The balling and shape irregularity found in the single tracks could be partially responsible for the large pores that were seen in the first few layers of the bulk samples. Smaller pores observed in the top layers of the deposit can be the result of the higher temperatures in the melt pool leading to the evaporation of some of the elements in the powder. These observations indicate that achieving optimal build quality may require changing the processing parameters during the deposition process. Further, studying single tracks provides insight into the interaction between deposited material and the substrate, which is important for repair applications or improving the initial layers of a build.

4.4.4. Microstructure and mechanical behavior of block deposits

Using the optimal thin wall processing conditions, we show that it is possible to deposit AlSi10Mg blocks with minimal porosity and minimal microstructural and mechanical property variation throughout the build. The block deposits display a cellular microstructure (Figure 4.8), which results from the interaction between the phase transformation behavior of AlSi10Mg and the nonequilibrium nature of the AM process. Unlike the microstructure of cast Al-Si alloys, where Si particles have needle- or rod-like morphologies in the Al matrix [107], these samples show that very fine Si particles form into a Si/α eutectic cellular network. The microstructure formed in samples deposited with L-DED is similar to what has been observed in AlSi10Mg samples processed in PBF [12]. The high cooling rate associated with AM processes increases the solubility of Si in the Al matrix; however, as the matrix solidifies, it rejects extra Si into the liquid. The solubility of Si will continue to decrease when the remaining liquid cools down, leading to rejection of more Si to the solidified front. This results in islands of Si-rich eutectic regions along the cell boundaries when the liquid finally solidifies [108]. Rapid solidification of eutectic or hypoeutectic Al-Si alloy results in an increased concentration of primary Si in the Al matrix as the solidification velocity increases [10]. The solute concentration of Si in the Al liquid is affected by the cooling rate and the diffusion rate of Si, which can be controlled by the process parameters [12,108].

The primary strengthening mechanisms in AlSi10Mg are solid solution strengthening and precipitation hardening [109]. Mg_2Si precipitation allows this alloy matrix to be age hardened without compromising other mechanical properties [83]. The layer-by-layer deposition nature of LENS® processing acts as a heat treatment to let Mg_2Si phases be formed and stabilized in layers close to the substrate. As Zheng et al. showed, the bottom layers of a LENS® deposit are exposed to repeated heating cycles as subsequent layers are being deposited, leading to exposure of the first few layers to precipitation-forming temperatures for a relatively long time [105]. The elevated temperatures that develop in the first few layers of the deposits help to stabilize the Mg_2Si phase. The EDS results (Figure 4.7) show a high concentration of Si in the cell boundaries as well as an even distribution of Mg in the sample. With the resolution of EDS, it is not possible to distinguish Mg_2Si directly. However, XRD results (see Figure 4.6) show the presence of the Mg_2Si phase in the bulk sample, which confirms that LENS® processing can precipitate this phase without requiring any postprocessing heat treatments.

The micrographs in Figure 4.10 show the presence of different types of porosity in the blocks. Pores, in AM, are divided into two main categories: irregular pores and spherical pores. Irregularly shaped pores are typically larger than 100 μm in size and are often the result of lack of fusion/bonding/melting, shrinkage, and material feed shortages that can usually be seen on the border of tracks [6,104]. Spherical pores are usually smaller than 100 μm and mostly seen in the middle of molten tracks. These pores are the result of material vaporization, entrapped gas, or Marangoni turbulence in the melt pool [104]. In this study, the pores in the layers closer to the substrate were mostly due to lack of fusion, or an insufficient hatch overlap (Figure 4.10 (a)), while the smaller pores in the layers farther from the substrate are likely the result of entrapped gas in the sample (Figure 4.10 (c)).

The average microhardness and tensile strength of the samples in this study are higher than those for cast samples but lower than those for samples processed by PBF [86], see Table 4.1. This is a consequence of having smaller cell and grain sizes in the AM parts compared to cast samples, which increases the total yield strength of the samples according to the Hall-Petch mechanism. Alternatively, the mechanical properties are lower than as-built PBF samples, likely due to the finer microstructures that are formed in PBF parts due to higher cooling rates [8].

The microhardness and yield strength results exhibit a slight change as a function of location in the block. Numerous other studies have also shown location dependent microhardness values in L-DED samples. For instance, Chen et al. reported an increase in the microhardness value going from the substrate to the top of their bulk samples [95], while Lv et al. showed the opposite trend [97]. In both studies, the location dependence was attributed to the difference in the cellular structure of the bulk samples. The high laser power (1900-3600 W) and the geometry of the samples (similar to thin walls) used in these studies resulted in inhomogeneous cellular structures throughout the samples leading to a gradient in the microhardness values. In contrast, by using the optimal thin wall processing conditions, we are able to deposit block samples at lower laser power (600 W) leading to homogenous microstructures and mechanical properties.

The grain boundaries play an essential role in providing resistance to dislocation movement in a polycrystalline material. In this study, a significant change in the microstructure has not been seen, and this suggests that the yield strength in the different locations of the samples should not be different. Conversely, it is seen in the AM literature that elongation and tensile strength of samples depend on the presence of porosity, especially LoF porosity. LoF porosity acts as a source of stress concentration during tensile testing [12,110]. The Si segregation to the cell boundaries, as mentioned above, also reduces ductility because Si is a brittle phase. Prashanth et al. demonstrated, for instance, that in PBF parts the fracture propagates preferentially along the hatch overlap regions, where the brittle Si phase is concentrated [111]. In the current study, the tensile specimens that were closest to the substrate exhibit a lower UTS and elongation than the specimens from the top of the blocks. This behavior is likely due to the higher number of larger LoF pores and the increased Si segregation to cell boundaries observed in the layers closer to the substrate, which result in the material being less ductile.

4.5. Conclusions

A series of single tracks, thin walls, and block samples were deposited from AlSi10Mg powder using the L-DED system. The physical properties of the single tracks, the geometry and porosity of thin walls, and the physical and mechanical properties of the block samples were investigated. The single track analysis shows that a minimum power of 800 W and a maximum scan speed of 10.5 mm/s are required to be able to successfully deposit single tracks with the desired shape and morphology. Increasing powder feedrate resulted in an increase in the width, height, and depth of the cross section of the single tracks up to a saturation point. Although single track morphology might affect the porosity in the bulk sample, viable single track parameters do not necessarily lead to viable thin walls or blocks. New strategies must be developed for scaling desired single track features to bulk parts. In fact, thin walls can provide better guidance on proper deposition parameters for larger blocks.

The scalability of optimal thin wall processing parameters was demonstrated by depositing block samples under the same conditions. The mechanical behavior of the deposited blocks in this study is equivalent to or better than cast materials. Minor inhomogeneity in mechanical behavior (ultimate tensile strength and elongation) in the block deposits were observed as a function of height within the build. This behavior is related to inhomogeneous microstructural features, including porosity and Si/α eutectic formation at the cell boundaries. Only minimal changes in the microhardness and yield strength were observed, due to the retention of a fine homogenous microstructure after deposition. This study confirms that, although not straightforward, L-DED can be used to successfully build AlSi10Mg parts with desirable microstructures and properties.

Chapter 5: The Reusability of AlSi10Mg Powder in Directed Energy Deposition

Abstract

Metal additive manufacturing (AM) has emerged as a powerful method of fabricating complex parts using a wide range of metal powders. However, large amounts of powder do not fuse to the final part and are lost as waste. Powder recycling is essential to make AM processes more sustainable. The effect of reusing AlSi10Mg powder in laser directed energy deposition has not been well studied, particularly the effect on the powder physical properties and the mechanical properties of the final parts. In this work, AlSi10Mg powder has been used for five deposition cycles in a directed energy deposition system, and the results show that the act of reusing the powder changes the powder morphology, size, and flowability. The elongation and ultimate tensile strength of parts deposited using the recycled powder decreases after being reused one time; however, no significant change was observed when the powder was used for more than one reuse cycle.

5.1. Introduction

Metal additive manufacturing (AM) has proven itself capable of producing complex parts for a wide range of applications [8]. AM allows for the fabrication of parts with unique microstructures and significant geometric complexity compared to conventional metal forming techniques. Although based on similar principles, different AM systems make use of different powder delivery systems, energy sources, deposition strategies, etc. Powder bed fusion (PBF) systems such as selective laser melting (SLM) and laser directed energy deposition (L-DED) systems, such as laser engineered net shaping (LENS®) are explained previously.

Laser-based metal AM has been employed to process a variety of starting materials such as stainless steel, Al alloys, Ti alloys, and Ni-based superalloys [112]. Al alloys are used in many industries, from automobiles to aerospace, due to their light weight and high specific strength. Although novel methods have been introduced to deposit high strength (7xxx series) Al alloys in AM [113,114]. The processing and properties of AlSi10Mg is well documented in both PBF and L-DED, demonstrating that metal AM can be a powerful tool for processing AlSi10Mg parts [97,115,116].

Early studies on AM recognized it as a novel method to potentially reduce waste production compared to conventional subtractive manufacturing methods by eliminating metal scrap or swarf and minimizing the required post-processing steps [117]. However, different studies have shown that powder waste during AM can be significant, unless that waste powder itself is recycled [118,119]. The material capture efficiency, the ratio between the amount of powder that is used to form the final part and the total powder that goes into the system, can be used as a metric to determine the amount of waste produced in the AM process [20]. Powder capture efficiency is generally reported to be between 3-25% [120], indicating that 75-97% of the powder used during AM will go to waste. Although the materials capture efficiency can be adjusted using different processing parameters, improving the capture efficiency can sometimes come at the expense of the quality of the final part. One method of mitigating the low capture efficiency in AM is through powder recycling, taking the waste powder from one build cycle and reusing it for the fabrication of other parts. Recycling of waste powder could be critical in decreasing the cost and environmental impact of producing AM parts.

Although a large portion of the powder used in AM does not fuse to the final part, some of the particles could be influenced by the laser or the AM process itself. The unused particles have the potential to interact with the laser or other hot surfaces in the chamber and undergo morphological changes. Additionally, flowing powder during AM processing could influence the surface of the particles, the surface of particles can be affected by the friction between the particles themselves and also the friction between the particles and the powder transportation vessel. Several studies have been dedicated to understanding the effect of powder reuse on the characteristics of the powders themselves and the properties of the final parts. Powder characteristics include, but are not limited to, the shape, particle size, size distribution, surface finish, oxidation, and contamination on the surface. Terrassa et al. investigated the impact of reusing 316L stainless steel powders for nine cycles in L-DED. Compared to parts made from virgin powders, parts made from recycled powders exhibited minimal changes in their mechanical properties [43]. Slotwinski et al. found that the particle size distribution of stainless steel powder increased after being recycled in direct metal laser sintering [121]. Recycling of AlSi10Mg powder in SLM systems has been explored in several studies [122–125]. For instance, Tradowsky et al. investigated the influence of post-processing and powder recycling and concluded that using recycled powders results in parts with a greater number of pores. They attributed the formation of irregularly shaped pores in the final parts to formation of an oxide layer on the surface of recycled powder [126]. Most of these studies showed that although recycling powder does yield some changes to the particles and properties of the final parts, the properties of the final parts are still acceptable for most applications. However, the resulting particle size distributions for recycled powders are inconsistent between different studies, with some studies observing that recycled powders are larger than virgin powders [122], and other studies such as Del Re et al. observing the opposite [124]. These contradictions by different authors suggest that there are different factors before and during the deposition process that can influence the particle size. To the authors' knowledge, there are no studies focusing on reusing AlSi10Mg powders in L-DED systems. Since L-DED systems use a fundamentally different powder delivery system compared to SLM, which is particularly sensitive to feedstock particle size, further investigation is required to understand the effect of reusing AlSi10Mg powder on the reused powder characteristics and the properties of the final builds. To this end, the influence of reusing AlSi10Mg powder during L-DED processing has been investigated by consecutively recycling powders for five deposition cycles. The changes in the powder morphology, particle size distribution, and flowability through the five reuse and deposition cycles was investigated. In addition, mechanical and microstructure analysis was performed on the parts deposited with the fresh and recycled powder to assess how the recycling process influences the quality of the deposited parts.

5.2. Materials and Methods

AlSi10Mg powder with a size range of 45-150 µm was purchased from Valimet. Mechanical sieving was used to confirm the size of the AlSi10Mg powder particles. The powders were used in a LENS® 1000 workstation system to deposit blocks with dimensions of 3.81 cm x 1.01 cm x 1.01 cm. Following from the results of our previous work (See Chapter 4), the parameters used for deposition were 600 W laser power, 16.9 mm/min scan speed, and 2 RPM powder feedrate [116]. Fresh powder (referred to as P0 in this study) was used to deposit blocks that are considered as the first cycle (B1 blocks). Powder recovered from the first cycle (P1) that was not attached to the final parts were collected and sieved. The sieved powder was used for the following cycle (C2) to deposit blocks (B2 blocks) and make P2 powder. The same routine was continued for 3 more cycles, making a total of five cycles. A schematic flow chart of the process is shown in Figure 5.1. The recommended particle size range for L-DED is between 45 µm and 150 µm. #325 and #100 mesh sieves were used to remove the particles outside the recommended range. Particles between 46-150 μm were collected and used for the following cycle. All the block samples were deposited in a two-week period and the oxygen level was kept at below 20 ppm.

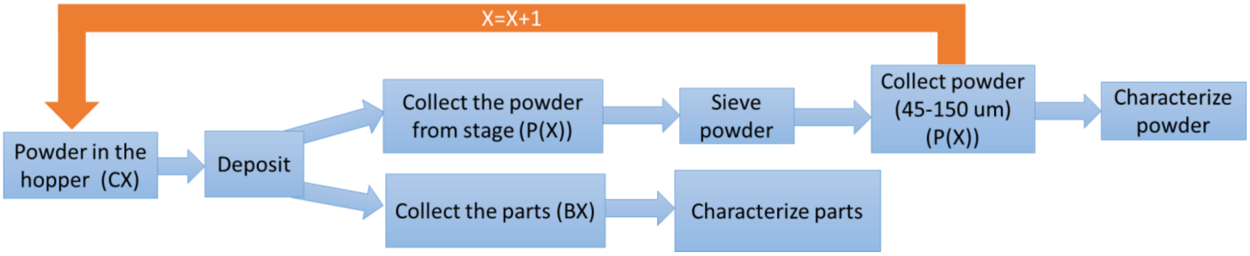

Figure 5.1. Flow chart of the process. Blue arrow indicates the step taken in each cycle; the orange arrow indicates the start of a new cycle.

Particle size and powder morphology were characterized using a FEI Quanta 3D scanning electron microscopy (SEM). The particle size (D_{10}, D_{50}, and D_{90}), average aspect ratio (AR_{50}), and particle size distribution for each powder was calculated from SEM micrographs. The software provided on the Olympus BX53M microscope was used to measure the particle size and $AR_{50.}$ Particle size in this study is considered as the equivalent diameter of a spherical particle with the same area as the particle captured in the SEM micrographs. AR_{50} is the ratio between the smallest and largest diameter of the particles, where 1 corresponds to a perfect sphere. Span represents the width of the particle size distribution and is calculated using the equation $\frac{(D_{90}-D_{10})}{D_{50}}$. The flowrate of the particles was measured using two different approaches. The first method, referred to as the powder feed rate (PFR) method, involves measuring the actual effective flowrate during a deposition experiment in units of g/min. In this study, PFR was calculated within the L-DED machine during each deposition by measuring the difference in the amount of powder in the hopper before and after deposition relative to the duration of the deposition. PFR provides the average powder flow rate for the whole deposition experiment. The second method involves measuring the powder flowrate using a custom-built funnel method. 50 g of powder was put through a Pyrex funnel, and the required time for the powder to flow from the funnel was measured. A Photron

SA-Z high-speed camera, operating at 500 fps (frames per second), was used to measure the required flow time more accurately. Further details on our custom funnel method can be found in a previous publication [127]. X-ray diffraction (XRD) was used to investigate the phase state of the powders from different cycles. XRD patterns were acquired using a SmartLab diffractometer using Cu Kα radiation.

The blocks deposited in each cycle were used for density measurements, mechanical testing, and microstructure analysis. The dog bone coupons were cut using a Mitsubishi wire electrical discharge machine (EDM) model F020S. The dog bone samples have a gauge length of 10 mm and a thickness of 1 mm, and were cut parallel to the build direction, as shown in the schematic in Figure 5.2. Dog bones were polished and used for the tensile testing and density analysis. Sample densities in this study were measured in ethanol at room temperature using the Archimedes method [93]. Tensile tests were performed on the dog bones using an Instron 8801 equipped with a 100kN load cell and a video extensometer to resolve axial strain with a nominal strain rate of 0.001 s^{-1}. The fracture surfaces of the dog bones after the tensile tests were investigated using SEM. A separate piece of the build (referred to here as a microstructure piece) was cut from each block to be used for microstructure and microhardness analysis, as shown in the schematic in Figure 5.2. Vickers microhardness tests were obtained using a Struers Duramin 5 instrument by averaging the microhardness value of 50 indents performed with an indent force of 9.8 N with a 15 s hold.

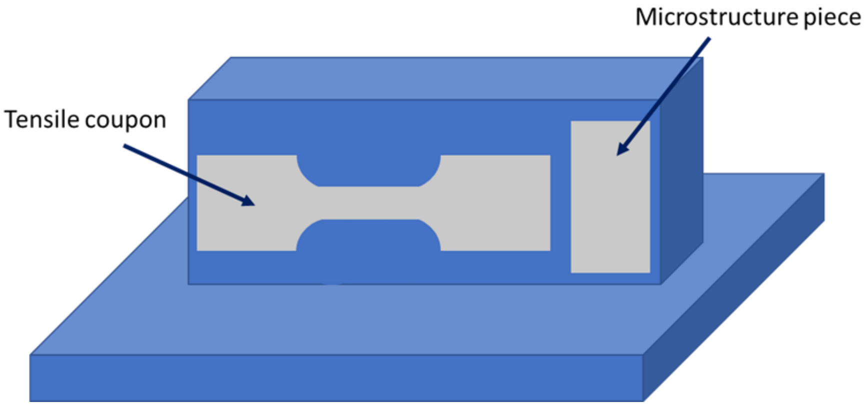

Figure 5.2. Schematic of a deposited block showing the geometry and locations of the dog bone tensile coupons and microstructure piece used for bulk analysis in this study.

5.3. Results

The P0-P4 powders display particles with primarily spherical shaped morphologies, with some satellite features formed on their surfaces (Figure 5.3). Additionally, semi-spherical and elongated morphologies can be observed in the particles from all the cycles. The AR_{50} of the powders generally decreases with increasing reuse cycle (Figure 5.4 (c)). Fresh powder (P0) with an $AR_{50} = 0.75$, has the most spherical particles in this study, while powder from cycle P4 has the most non-spherical particles, having an $AR_{50} = 0.61$. The particle size (D_{10}, D_{50}, and D_{90}) increases with increasing reuse number, as observed in Figure 5.4 (a). The D_{50} of the virgin powder (P0) was less than 80 µm. The D_{50} increases with increasing powder reuse cycles, with the D_{50} becoming larger than 100 µm for cycles C3 and C4 (P3 and P4). Sieving analysis (Figure 5.5) reveals that the powders collected after each cycle contain particles larger than 150 µm and smaller than 45 µm. On average, 0.11wt. % of the collected particles were smaller than 45 µm, and 0.34 wt.% were larger than 150 µm for each cycle. The amount of the particles smaller than 45 µm decreased with increasing powder reuse cycle. However, the number of particles larger than 150 µm does not follow an obvious trend with increasing reuse cycle. The span value decreases with increasing reuse cycle, as displayed in Figure 5.4 (b). The particle size distribution narrows as the powders are reused, with the span value decreasing from 0.51 in P0 to 0.38 in P4 powder.

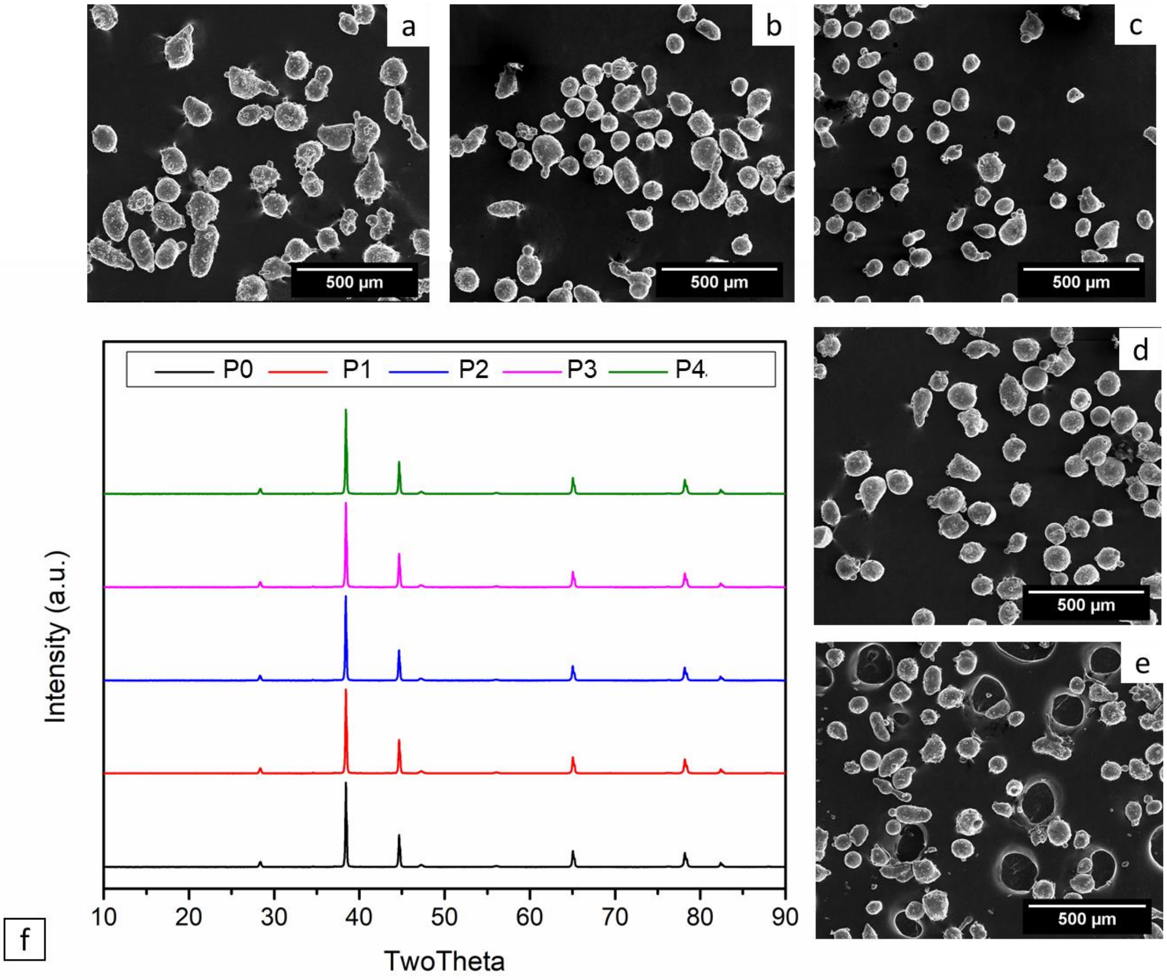

Figure 5.3. SEM micrographs displaying the morphology of the a) P0, b) P1, c) P2, d) P3, and e) P4 powders. f) XRD patterns of the powders from each reuse cycle.

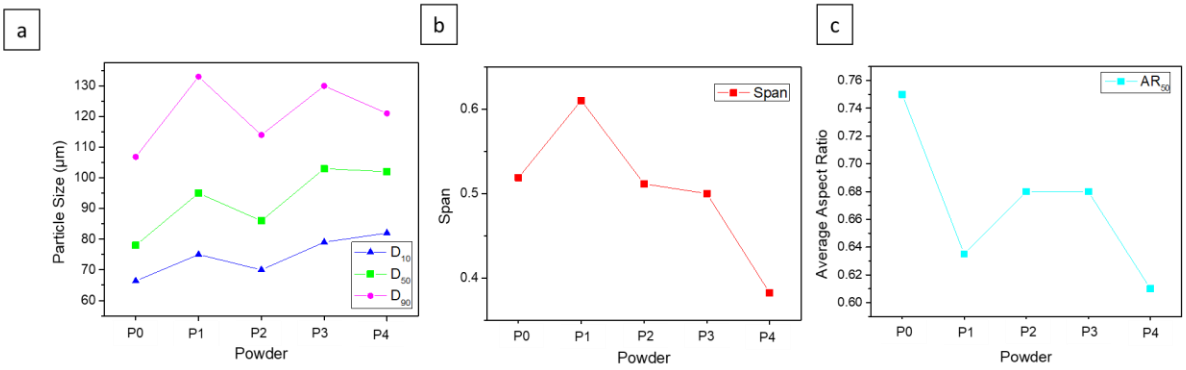

Figure 5.4. a) Particle size (D_{10}, D_{50}, and D_{90}), b) span, and c) average aspect ratio (AR_{50}) of the powders from all the reuse cycles.

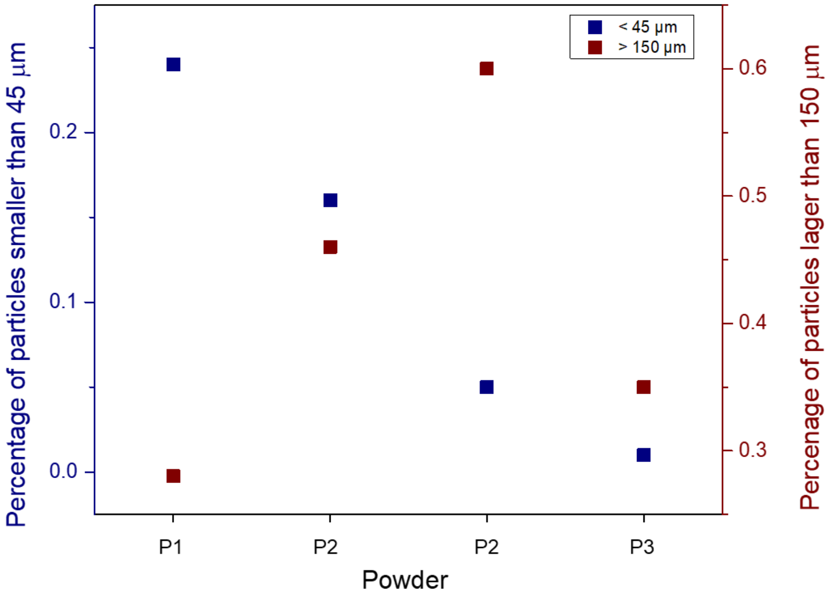

Figure 5.5. The mass percent of particles smaller than 45 µm and larger than 150 µm found in each cycle.

The morphology of the particles larger than 150 µm collected in different cycles is displayed in Figure 5.6. The micrographs of these particles suggest that the particles primarily consist of several particles that are fused to each other. However, individual semi-spherical particles that are larger than 150 µm are observed as well. In addition, no changes are observed in the XRD patterns with increasing powder reuse cycles (Figure 5.3 (f)). No extraneous peaks were observed in any of the powder samples as well, confirming that reusing the AlSi10Mg powder does not affect the observed phase state and no significant contamination is being introduced during the recycling process.

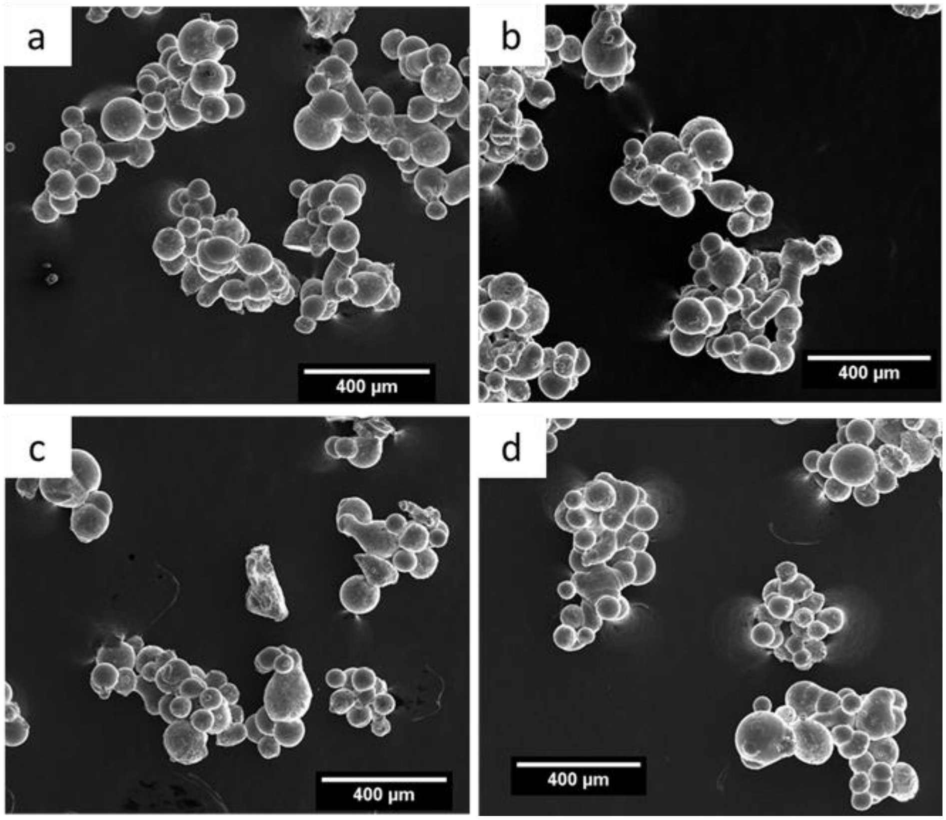

Figure 5.6. SEM micrographs displaying the morphology of the particles larger than 150 μm from powders a) P1, b) P2, c) P3, and d) P4.

The flowrate measurement results, displayed in Figure 5.7, show that both PFR and the customized funnel flowrate measurement techniques show similar flowrate behavior with increasing powder reuse cycles. The P0 powder has a flowrate of 9.15 g/s, which is significantly higher than the recycled powders (8.08-8.50 g/s). However, no significant change in flowrate was observed between powders P1, P2, P3, and P4, indicating that increased reuse cycles do not meaningfully impact powder flowability. The flow analysis of the powders in this work show that our custom funnel method produces a similar trend in flowability as to what is observed in PFR, confirming that our custom funnel measurement is an adequate proxy for observing relative changes in flowability during L-DED.

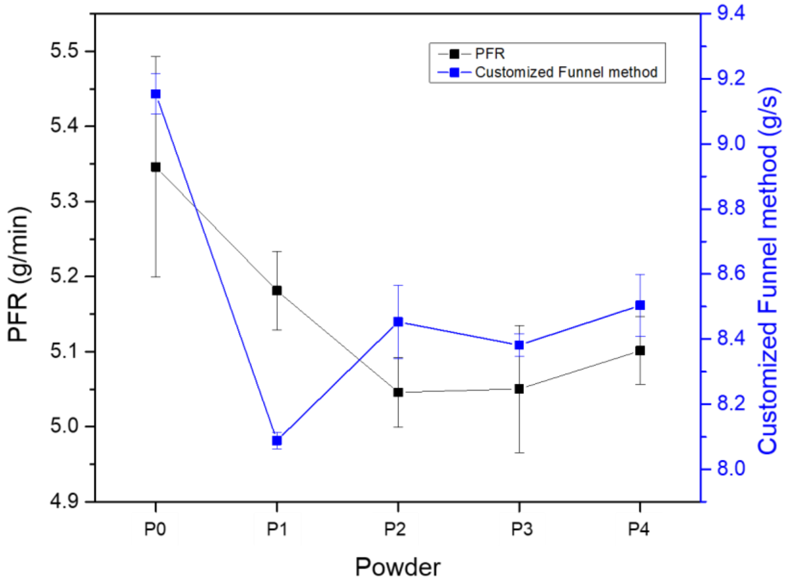

Figure 5.7. Flowrate of the powders from the different reuse cycles measured using the modified funnel method and the powder feedrate (PRF) method.

The measured density values (Figure 5.8 (a)) show that the samples are, on average, 99% dense compared to the theoretical density (2.68 g/cm^3 [45]). Minimal variation in density is observed between the blocks fabricated with the P0-P4 powders. Further, the pore morphology in the block samples were similar amongst all the cycles, with most of the pores being similar to the representative pore displayed in Figure 5.8 (b).

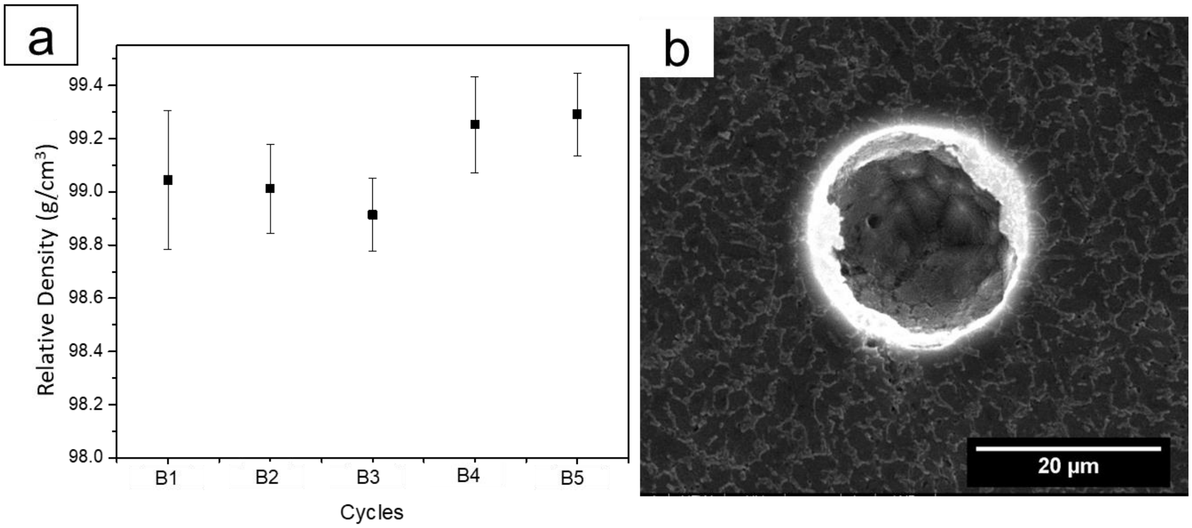

Figure 5.8. a) The density of deposited blocks for each cycle, b) representative micrograph of a pore observed in a deposited block sample.

The mechanical properties of the blocks deposited using the P0-P4 powders are displayed in Figure 5.9. The highest ultimate tensile strength (UTS) and elongation values in this study are 329 MPa and 9.7%, respectively, which are observed from the B1 build. However, UTS and elongation values do not change significantly between cycles B2-B5. In addition, the yield strength in the samples does not change significantly between the five cycles. A similar pattern is observed from the microhardness measurements, except for the B3 samples, which shows the lowest microhardness value among all the cycles.

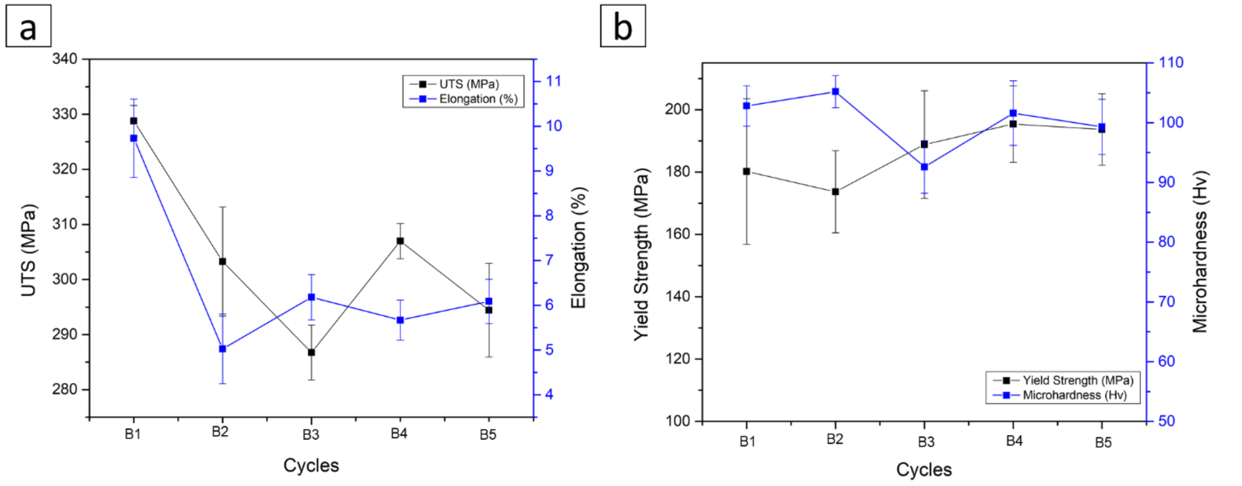

Figure 5.9. Mechanical properties of the samples deposited for all of the cycles. a) ultimate tensile strength (UTS) and elongation. b) yield strength and microhardness.

5.4. Discussion

The quality of the final parts in AM is influenced by a wide range of parameters that can be controlled directly and indirectly by the user. Among these parameters, powder characteristics have a significant indirect influence on the properties. Powder characteristics such as chemical composition, morphology, and particle size distribution can affect the AM process and, at the same time, the AM process can modify the characteristics of the waste powder. Particle size distribution and morphology will influence the flowability and compactibility of the powders, which is discussed in more detail later. In this study, it is observed that increasing number of reuse cycles results in an increase in the D_{50} and a decrease in the span and AR_{50}. Santecchia et al. investigated the laser-metal powder interaction in SLM and showed that by-products such as condensate and spatter formed during the process [128]. In L-DED systems, powders are ejected through the nozzles aiming at the substrate, and the laser-powder interaction can be significantly different compared to SLM. Haley et al. showed the probability of detecting particles at a specific angle from the nozzle after they left the nozzle toward the substrate [129]. Their results suggest that not all the particles will be affected by the laser directly; however, they might still be affected by other particles. In PBF, the heat from the melt pool and laser travels through the powder particles, where some studies show that the particles are even melted before directly interacting with the laser [38,130]. However, heat transfer is significantly lower in a powder bed compared to a bulk sample because of the limited physical contact between the powder particles. Heat transfer between the particles is minimized in L-DED.

In both L-DED and PBF, a high-pressure plume forms above the melt pool due to the evaporation of metal and the heat generated in the melt pool. This high pressure plume in L-DED only allows specific particles to pass the plume barrier and enter the melt pool zone [131]. The size, velocity, and trajectory of the particles play a significant role in determining whether a particle will enter the melt pool or not. Haley et al. used a high-speed camera and extensive modeling to show that some of the particles that interfere with the laser absorb some energy and travel away from the melt pool, while others absorb heat and enter the melt pool [102,129]. In addition, Shin et al. used a predictive model to show the temperature gradient that powders experience after leaving the nozzle [132]. Their results indicate that not all the powder particles experience a temperature sufficient to induce melting. Wolff et al. used in-situ X-ray imaging of the L-DED process and showed that some particles interfered with the laser before they were able to enter the vapor-plasma plume, and they were able to detect a shape-change in those particles [131]. During the deposition process, particles that are partially melted by the laser, or other hot surfaces, can experience significant morphological changes. Molten or partially molten particles can deform or fuse to other particles during a collision. Finer particles are particularly susceptible to such an event due to their smaller volumes making significant melting more likely. The morphologies of these deformed particles will depend on what the particle experiences after melting. Little change in the particle morphology would be expected from particles that experience partial melting but then solidify before landing on the stage. Some of the partially melted particles collide and fuse with another particle. Lastly, particles that impact the stage before solidification will have highly deformed or non-spherical shapes, with the extent of the change depending on the degree of melting and the speed with which the particle impacts the substrate. Our observed increase in D_{50} as a result of the powder reuse process is due to the fact that agglomerates of fused particles are often larger than the particles observed in the virgin powder. In addition, the lightweight fine particles may fly further into the LENS® chamber and be captured by the filtration system. As mentioned earlier, particles smaller than 45 µm and larger than 150 µm can be found in each cycle. Additional fine particles can be produced as a result of splashes from the melt pool and from satellites breaking off from agglomerated particles during the feeding and deposition process. Previous work has reported that particle-particle friction during AM causes the number of particles with satellites to be reduced in waste powders [37]. Similar behavior is observed in this study, with reused particles having smoother surfaces compared to the virgin powders (Figure 5.3). However, the number of fine particles (smaller than 45 μm) decreases with increasing reuse cycles (Figure 5.5), confirming that as the powder is being reused and subsequently sieved, the number of satellites decreases, fine particles are lost in the chamber, and the surface of the particles becomes more smooth. Further, large particles (above 150 μm) are formed after every reuse cycle as a result of multiple particles fusing together, as shown in Figure 5.6, which further reduces the number of fine particles in the powder.

Numerous studies have emphasized the relationship between the powder physical characteristics, the powder flowability, and the properties of the final parts [39,133]. For example, our previous work (see Chapter 2) demonstrated that the morphology of the particles (i.e., AR_{50}) influences the initiation of powder flow from a static or compressed condition while D_{50} influences how well powders maintain their flow after flow has already begun. An inconsistent flow in L-DED systems such as LENS® can result in brief shortages in available powder at any moment during deposition, which can lead to parts with low density and poor properties. The flowrate analysis in this work shows that the greatest change in powder flowrate occurs between the P0 powder and the P1 powder, which are related to the significant changes in the morphology and particle size distribution as a result of the L-DED process (Figure 5.4). Our previous work (see Chapter 2) shows that as D_{50} increases, flowability through nozzles and funnels decreases due to the larger particles being confined by a narrow exit diameter [127]. Similarly, increasing span also decreases the flowrate due to an increase in fine particles which restrict flow by fitting in between larger particles. Conversely, AR_{50} was shown to not strongly influence the flowrate of powders that have already begun to flow. The flowrate of the powder reaches a plateau after two recycling cycles (P2 powders), which we attribute to the changes in the span and D_{50} between the P1-P4 cycles. In these samples, increasing reuse cycles causes the span to decrease and the D_{50} to increase, which has contradictory influences on the flow, thus preventing significant changes to the flow of the powder particles. The result from this work corroborates previous studies by showing that the flowrate of the particles is reduced with increasing powder reuse cycles. However, in this study, the flowrate reaches a plateau after reusing the powders twice. Besides the change in the morphology, size, and span of the particles, no phase change or significant contamination has been identified from the powder XRD patterns.

The relationship between powder recycling, powder flowability, and final part properties has been studied before [39,43,124,134]. Seyda et al. showed the relationship between the flowability of the particles and the properties of parts processed in AM [39]. However, the previous literature is contradictory, with some studies showing that despite changes in morphology after powder reuse, the mechanical properties and density of the samples do not show significant variations [43,134]. Conversely, other studies observe changes in the density or mechanical properties of samples fabricated with reused powders [124]. However, these changes appear to be very material and method dependent. For instance, Tang et al. showed an increase in the flowrate and mechanical properties of Ti6Al4V in selective electron beam melting [37]. Similar behavior was reported by Seyda et al. [135]. However, others such as Del Re et al. showed a decrease in the measured UTS value with increasing reuse cycles in AlSi10Mg made with PBF [124].

In this current study, no significant change in the microstructure and density of the parts has been observed. However, a change was observed in the UTS and elongation values after the first reuse cycle. These changes are discussed in more detail below. Consistent powder flowability during L-DED is critical to achieve successful builds, as inconsistencies in the flowrate can affect the available material in the melt pool, as has been shown by other studies [102]. The excess particles resulting from a sudden increase in the flowrate can block the melt pool from accepting more particles and block the laser from providing energy into the melt pool [102]. Conversely, a shortage of particles due to a low flowrate can increase the chance of pore formation or result in undesired build dimensions. A deficiency in the available material can result in large and irregular pores that are detrimental to the UTS and elongation properties. However, as Haley et al. showed, powder fed systems benefit from a passive stability mechanism that can overcome the changes in the flowrate and height build up in different layers during deposition [129]. Nevertheless, changes in the mechanical properties are expected if the flow rate is inconsistent during deposition.

In the current study, the UTS and elongation values decrease after the first reuse cycle, which is attributed to the change in flowrate of the powders due to the changes in powder morphology. The yield strength and microhardness of the samples from all five cycles do not show any statistically significant differences. It is shown in many AM studies that the UTS and elongation values are more sensitive to the presence of the pores in the samples. Conversely, the microhardness and yield strength are more related to the grain size suggesting that the changes we observe in the UTS and elongation are the result of the porosity inside the samples [136]. Our previous work on AlSi10Mg (see Chapter 4) indicates that UTS and elongation are strongly influenced by the presence of lack of fusion pores in the build, which can emerge due to poor powder flowability [137]. Given the significant decrease in powder flowability after a single reuse cycle, the decrease in UTS and elongation in samples B2-B5 is attributed to an increase in the number of lack of fusion pores [116].

5.5. Conclusions

The influence of AlSi10Mg powder reuse during laser directed energy deposition (L-DED) has been investigated. The characterization of the particles shows that the average particle size increases and the particle size distribution narrows with increasing powder reuse cycles. Additionally, reused particles exhibited a lower average aspect ratio compared to the virgin powder. The changes to powder size and morphology led to a significant change in the flowrate after the first two reuse cycles. Minimal changes were observed in the mechanical properties of the samples with increasing reuse cycles. However, the ultimate tensile strength and elongation experienced a decrease between fresh and 1-time used powder. The change in the ultimate tensile strength and elongation is attributed to the change in flowrate that occur during the first two reuse cycles. However, the results of this study demonstrate that although recycling AlSi10Mg powder does change the powder morphology and particle size, there are only minimal changes to the powder flowrate and mechanical properties of the parts. This work indicates that recycling AlSi10Mg powder during L-DED does not compromise the properties of the final parts, and therefore could be an effective method of reducing the cost and environmental impact of the L-DED process.

Chapter 6: Fabrication and Microstructure Evolution of Aluminum Matrix Composites Processed Using Powder Bed Fusion

Abstract

Additive manufacturing is a promising technique for processing aluminum matrix composites, allowing for parts that have low weight, high strength, tailored microstructures, and complex geometries. In this work, gas atomized Al 5083 and cryomilled Al 5083 with 5 wt.% B_4C powders have been used to process single tracks with different processing parameters using a powder bed fusion additive manufacturing technique. The effect of the ceramic reinforcement and processing parameters on the morphology and microstructure of the single tracks was investigated. The results of this work show that single tracks deposited with gas atomized and aluminum matrix composite powders have different melt pool size and morphology. In addition, the samples processed with ceramic reinforcements have a location-dependent dispersion of the B_4C particles throughout the single track. Scanning electron microscopy (SEM) and transmission electron microscopy (TEM) were employed to investigate the microstructure of the single tracks and confirm the presence of the reinforcements.

6.1. Introduction

Additive manufacturing (AM), which involves solidifying metal powder in a layer-by-layer manner, has potential applications in industries such as aerospace, automotive, and medicine [138]. AM offers the opportunity to increase design freedom, decrease post-processing steps, and reduce production costs. A wide variety of different chemical compositions have been processed in AM, including stainless steel [43], aluminum [90], and nickel-based superalloys [79]. Among these compositions, Al has attracted extensive attention in the aerospace and automobile industry due to its high specific strength and low cost. However, the most common Al alloys used in AM exhibit relatively low strength [114]. High performance Al alloys such as the 7xxx series are mostly un-weldable and suffer from hot cracking during AM [139]. However, limited studies have focused on the processing of Al 5xxx and 6xxx series in AM [140]. Al 5xxx and 6xxx inherently exhibit lower strength compared to high performance Al alloys and significant modification will be required in order to improve their mechanical properties.

One method to improve the mechanical properties of Al is by adding ceramic reinforcements to an Al matrix. These aluminum matrix composites (AMCs) have enhanced strength due to the ceramic reinforcements while still exhibiting high ductility from the metal matrix. Dislocation accumulation around the ceramic reinforcement particles leads to improved strength in the composite through the Orowan strengthening mechanism [141]. One of the most used alloys in AMC systems is Al 5083, which possesses good weldability, corrosion resistance, and formability. The Mn and Cr in Al 5083 precipitate into different phases that will improve the mechanical properties [142]. The high hardness of AMC samples makes machining and processing of these alloys difficult. Therefore, AM could be employed to manufacture AMCs parts with complex geometry that require minimum machining and post processing.

Previous studies exist on AM of different Al alloys which incorporate a variety of ceramic reinforcements, such as TiB_2 [89], SiC, $MgAl_2O_4$ [143], and Al_2O_3 [144]. The addition of Al_2O_3 to the pure Al matrix in selective laser melting (SLM) resulted in improved yield strength and microhardness [144]. Aversa et al. showed that the addition of nano-TiB_2 to AlSi10Mg altered the laser absorption behavior of the AlSi10Mg matrix, changing the morphology of the deposited single tracks and the optimal processing parameters [89].

B_4C has a high melting point, high hardness, and low density [145]. Moreover, the density of B_4C is close to Al; however, the high cost of B_4C has made this ceramic reinforcement less used compared to other reinforcements. A variety of different methods have been used to process B_4C reinforced Al 5083 alloys such as stir casting, squeeze casting, spray deposition, and powder metallurgy [146–148]. It is known that the size, morphology, and amount of B_4C reinforcement will influence the mechanical properties of wrought Al alloys. For example, Zhang et al. showed that increasing the amount of B_4C in Al from 5 to 20 wt.% increases the tensile strength while decreasing the relative density and ductility [149].

Cryomilling, which involves milling particles in a slurry of liquid N, has been used previously to prepare AMC powders for further powder metallurgical processing. It has been found that cryomilling produces a homogeneous distribution of ceramic particles in the Al matrix [75]. In addition, cryomilling can produce fine grains through severe plastic deformation and the inhibition of recrystallization [150]. Fine grains produced during the cryomilling process usually increase the strength at the expense of the ductility. In order to improve the ductility of the fine-grained Al, different approaches have been investigated. Trimodal composites, which are a mixture of fine and coarse grains in the matrix, plus ceramic reinforcements, have demonstrated the potential to improve the ductility while maintaining superior strength [151].

The most common feedstock used in AM is gas atomized (GA) powder, which consists of particles with a spherical shape and smooth surfaces. These powders have good flowability and often result in parts with fewer defects [152]. Less common feedstocks have also been used for AM such as water atomized (WA) powder and milled powder. These powders normally do not possess spherical shape and their flowability might be different compared to GA powder. In addition, the feasibility of using milled powder in AM has been investigated (see Chapter 3). Different studies have demonstrated minimal differences between samples processed in AM using milled stainless steel powder compared to GA [63]. Although it has not been extensively investigated, cryomilled powders can be used as starting feedstock in AM. Cryomilled powder has a unique morphology resulting from the milling process, often resulting in particles with flattened or other non-spherical shapes. The right combination of process control agent and milling duration can produce a powder whose morphology is suitable for AM. Han et al. showed that the duration of milling could change the morphology of aluminum particles and result in particles with good flowability after 20 hrs of milling [67]. Although AMCs using Al 5083 and B_4C have been extensively studied in more conventional manufacturing processes, to the authors' knowledge, there are no studies in the literature focusing on this combination in AM. In this work, metal AM is used to deposit single tracks of Al 5083 GA and Al 5083 + B_4C cryomilled powders. The influence of the B_4C particles and processing parameters on the morphology and size (width, depth, and height) of the single tracks has been investigated. The microstructure and the precipitates in the single tracks were also analyzed.

6.2. Materials and characterization

The Al 5083 GA powder was purchased from TLS Technic GmbH &Co and mechanically sieved to acquire particles smaller than 45 µm. The AMC powder was prepared by cryomilling Al 5083 GA powder (Valimet) with submicron 5 vol.% B_4C (U.S. Army Armament Research, Development and Engineering Center) and 0.2 wt.% stearic acid ($CH_3(CH_2)16CO_2H$ (Sigma Aldric)) as the process control agent. The mixture was milled in liquid N_2 for 12 hours, as has been described in previous studies [153]. Single tracks were deposited using a laser engineered net shaping (LENS®) workstation with a custom powder bed system. A thin layer of powder (150 µm) was spread on an Al 6061 substrate. Single tracks were processed using different scan speeds and laser powers, as summarized in Table 6.1. Three single tracks were deposited using each of the processing parameter combinations. The morphology of the single tracks was visually inspected and characterized using an Olympus BX533M optical microscope (OM), with the intent of identifying the physical differences between single tracks deposited with GA and AMC powders. The single tracks were cross sectioned in three different location along the track using a Mitsubishi model F020S wire electrical discharge machining (EDM) system. Cross-sections were polished metallographically with silicon carbide paper down to 1200 grit followed by polishing down to 1 µm using diamond suspension. Final polishing was performed using a vibratory polisher with 0.05 µm silica suspension. A FEI Quanta 3D scanning electron microscope (SEM) equipped with a backscattered electron detector (BSE) was used to analyze the morphology of the powders and the microstructure of the single track cross-section samples. Transmission electron microscopy (TEM) foil specimens were prepared using the focused ion beam (FIB) lift out process on the FEI SEM. The microstructure, elemental configuration, and phase composition of the foil specimens were examined using a JEOL TEM 2800 equipped with an energy-dispersive X-ray spectroscopy (EDS) detector. Phase analysis of the GA and AMC powders was performed using X-ray diffraction (XRD) with a Rigaku SmartLab diffractometer using a Cu Kα radiation source.

Table 6.1. The processing parameters used for deposition of the single tracks.

	Laser power (W)	Scan speed (mm/s)	VED (J/mm^3)
1	680	4.2	432
2	780	4.2	498
3	880	4.2	557
4	880	10.5	221

Volumetric energy density (VED) (J/mm^3) can be used to correlate the morphology of the deposited single tracks to the processing parameters. VED is a metric that assesses the energy delivered to the single track as a function of laser parameters, scan speed, and powder bed thickness [154]. VED is expressed in Equation 1:

Equation 1 $$\mathrm{VED} = \frac{\mathrm{P}}{\vartheta\sigma\mathrm{t}} \left[\frac{\mathrm{J}}{\mathrm{mm}^3}\right]$$

VED is defined as the ratio between laser power (P) and the product of the laser scan speed (ϑ), the diameter of the laser beam (σ), and the thickness of the powder layer (t). The calculated value for each set of deposition parameters is summarized in Table 6.1.

6.3. Results

GA and AMC powders exhibit different morphologies, as displayed in Figure 6.1 (a) and (b), respectively. As expected, the GA particles exhibit spherical shapes and smooth surfaces. Alternatively, the AMC particles show non-spherical shapes with rough surfaces due to the milling process (Figure 6.1 (b)). The XRD pattern of the GA powder displays only the presence of Al while the AMC powder XRD pattern shows the same primary peaks as the GA powder with the peaks corresponding to B_4C, as seen in Figure 6.1 (c). Milling the AMC powder does not change the phases present in the Al matrix.

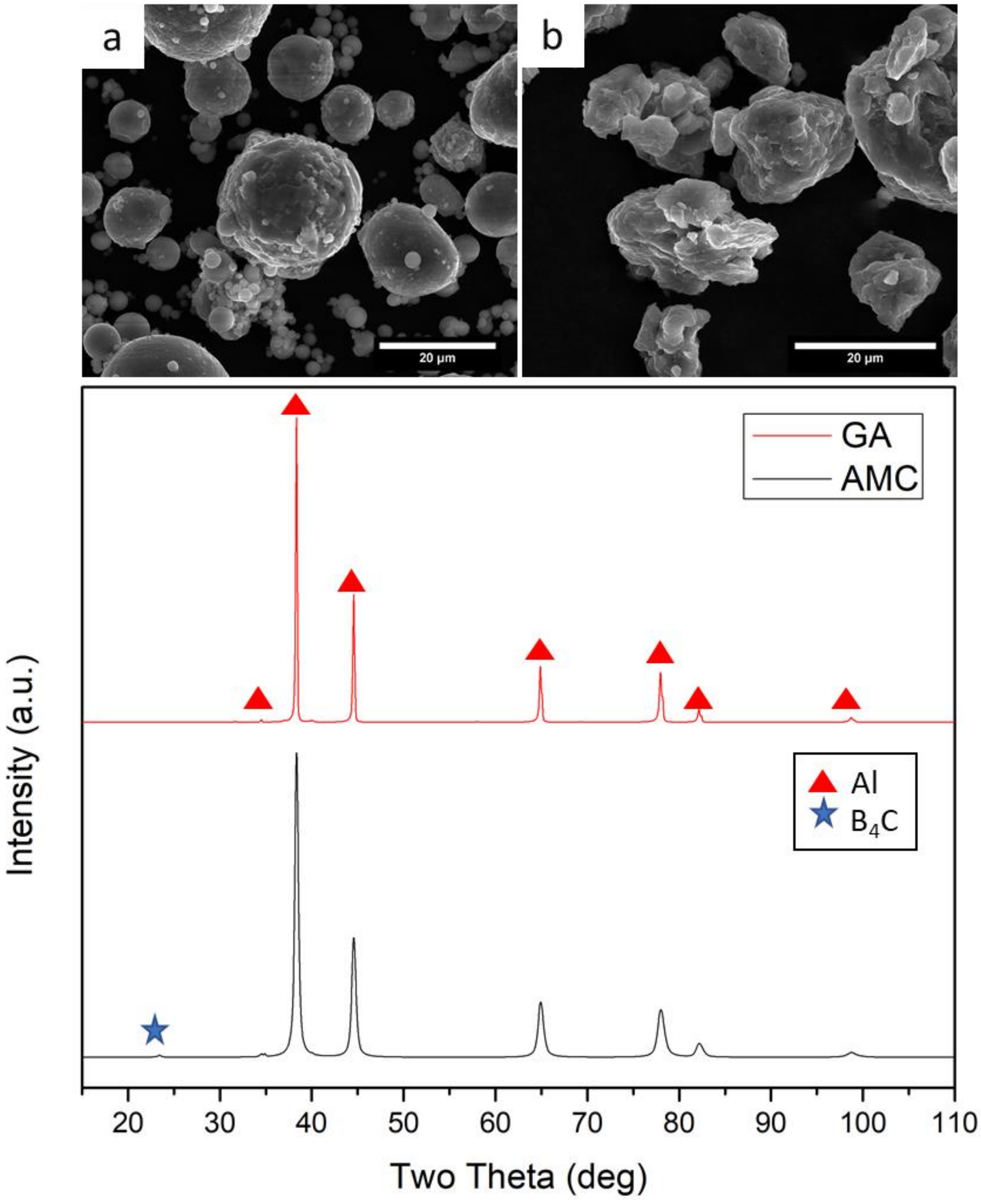

Figure 6.1. a) SEM micrograph of the GA particles. b) SEM micrograph of the AMC particles. c) XRD patterns of GA and AMC powders. (GA= gas atomized; AMC= aluminum matrix composite).

The morphology and the cross-section dimensions of single tracks can provide valuable information about the processability and behavior of the printed material, which can in turn provide insight into the properties of the final printed parts. The ideal morphology of a single track is a semi-cylindrical continuous shape that is attached to the substrate. Although our single tracks display a variety of shapes and morphologies, as seen in Figure 6.2, some similarities were observed between single tracks deposited with GA and AMC powders. As expected, the changes in the morphology of the single tracks are linked to the processing parameters. GA and AMC single tracks deposited with 4.2 mm/s scan speed and 680 W laser power do not exhibit a continuous shape, and beads are observable throughout the track. However, increasing the laser power resulted in both sets of the single tracks having smoother surfaces and greater consistency, regardless of which powder feedstock was used. In fact, at higher powers (880 W), both sets of single tracks are continuous. The single tracks deposited with 10.2 mm/s and 880 W show more continuous shapes, indicating that increasing the scan speed results in single tracks with more smooth surfaces.

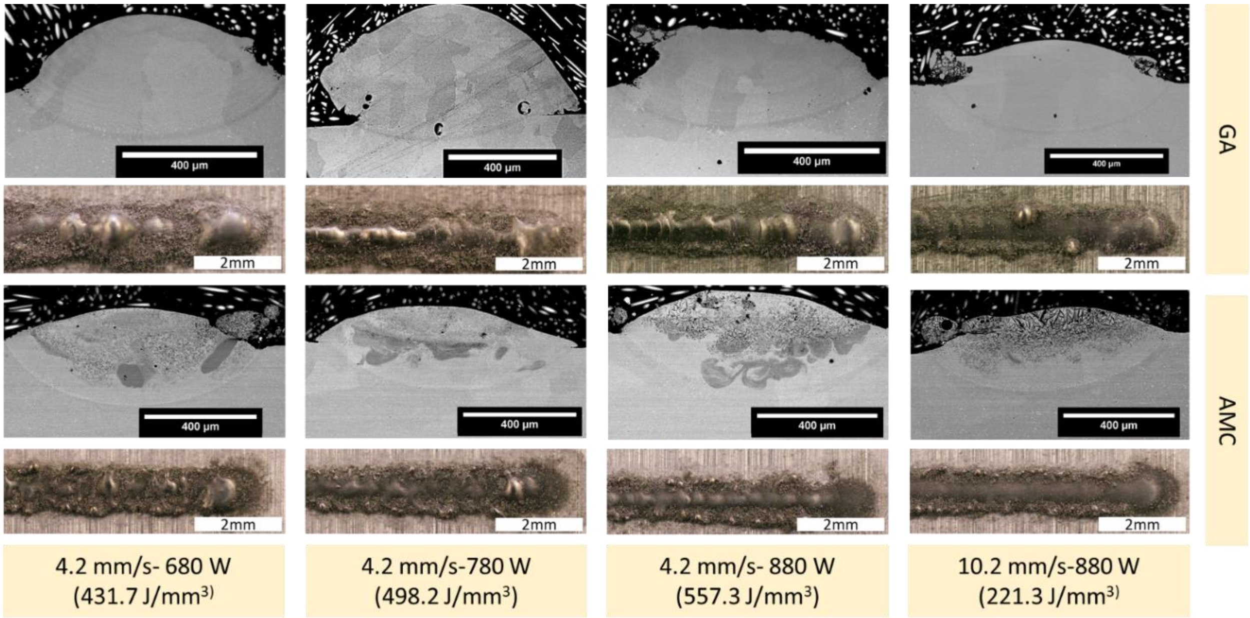

Figure 6.2. SEM micrographs of the GA and AMC single track cross-sections along with the corresponding optical micrographs displaying the overall morphology of the single tracks made using different VED values. (GA= gas atomized; AMC= aluminum matrix composite; VED= volumetric energy density).

The single tracks processed with GA powders display rounded or oval shaped cross-sections, while the AMC based single tracks display more flat or lens shaped cross-sections. The depth and width of single tracks cross-section were very similar in both GA and AMC samples. However, that is not the case for the height of the cross-sections, which are displayed in Figure 6.3

(a). Laser power and scan speed influence the height of single tracks differently depending on whether GA or AMC powders are used. The height of single tracks deposited with GA powder decreased with increasing laser power and increasing scan speed. Conversely, the height of single tracks deposited with AMC powders increased with increasing laser power and had minimal response to increasing scan speed. The overall change in the height of single tracks deposited with GA powder is more significant compared to the single tracks deposited with AMC powder.

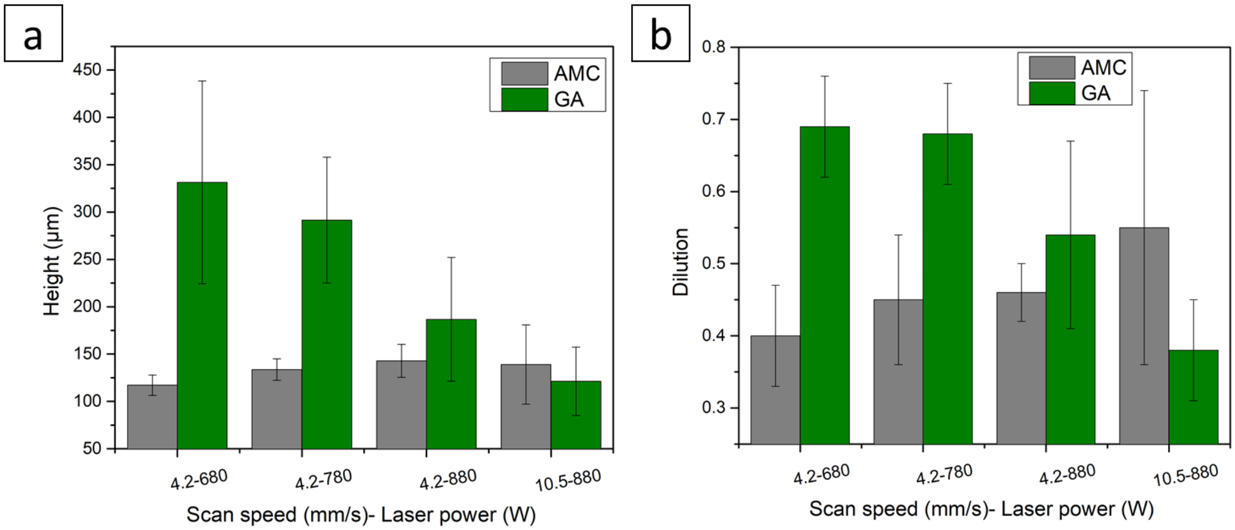

Figure 6.3. a) The height and b) dilution of single tracks deposited with GA and AMC powder made using different scan speed and laser power values. (GA= gas atomized; AMC= aluminum matrix composite).

Dilution is another important single track parameter that can determine the characteristics of the final printed parts. The geometrical definition of dilution is the height of the single track divided by the sum of the height and depth. Similar to single track height, laser power and scan speed influence the dilution of single tracks differently depending on whether GA or AMC powders are used. Looking at the dilution of the GA single tracks (displayed in Figure 6.3 (b)), increasing the laser power from 680 W to 780 W results in minimal change to the dilution ratio. However, increasing the laser power to 880 W significantly decreases the dilution ratio. Also, dilution decreased when the laser power was kept constant (880 W) and the scan speed was increased. The opposite behavior was observed in single tracks deposited with AMC powder, the dilution value increased when the scan speed was kept constant and the laser power was increased, Additionally, the dilution value increases when the laser power is constant (880 W) and the scan speed is increased. Additionally, GA single tracks display overall greater heights and larger dilution ratios than AMC single tracks when processed at 4.2 mm/s, regardless of laser power. However, increasing the scan speed to 10.5 mm/s results in an AMC track with a greater height and larger dilution ratio than the equivalently processed GA track (Figure 6.3 (a) and (b)). It is important to note that there is a significant amount of variance in the measured height and dilution values, making it challenging to completely deconvolute the influence of processing parameters on sample geometry.

The microstructure of the single tracks displays a variety of features. Some porosity, mostly small circular pores, are observed in the single tracks deposited with GA and AMC powder. Pores in AM are divided into two main categories: small regular pores and large irregular pores. Small pores are usually the result of gas entrapment in the deposition process or from the feedstock powder, while large irregular shaped pores are the result of using insufficient laser energy during deposition. Single tracks deposited with AMC powder showed rod-shaped features that possess a range of sizes and are irregularly dispersed in the single tracks. Figure 6.4. (a) displays the diversity in microstructures found in the AMC single track samples. Three different regions are observed in the samples. These regions include: regions with a homogeneous dispersion of fine precipitates (denoted with a blue oval), regions with large elongated precipitates (denoted with red ovals), and the heat-affected zone (denoted with a green box in Figure 6.4. (a)) which lacks precipitates. This pattern was observed in all the AMC single tracks; however, the region of fine precipitates becomes smaller in the single tracks deposited with the lowest VED value. The number of rod-shaped precipitates larger than 10 µm (measured along their length) is higher in single tracks deposited with the lowest VED value, as seen in Figure 6.4. (b). The majority of the rod-shaped precipitates in the samples with higher VED values were smaller than 10 µm.

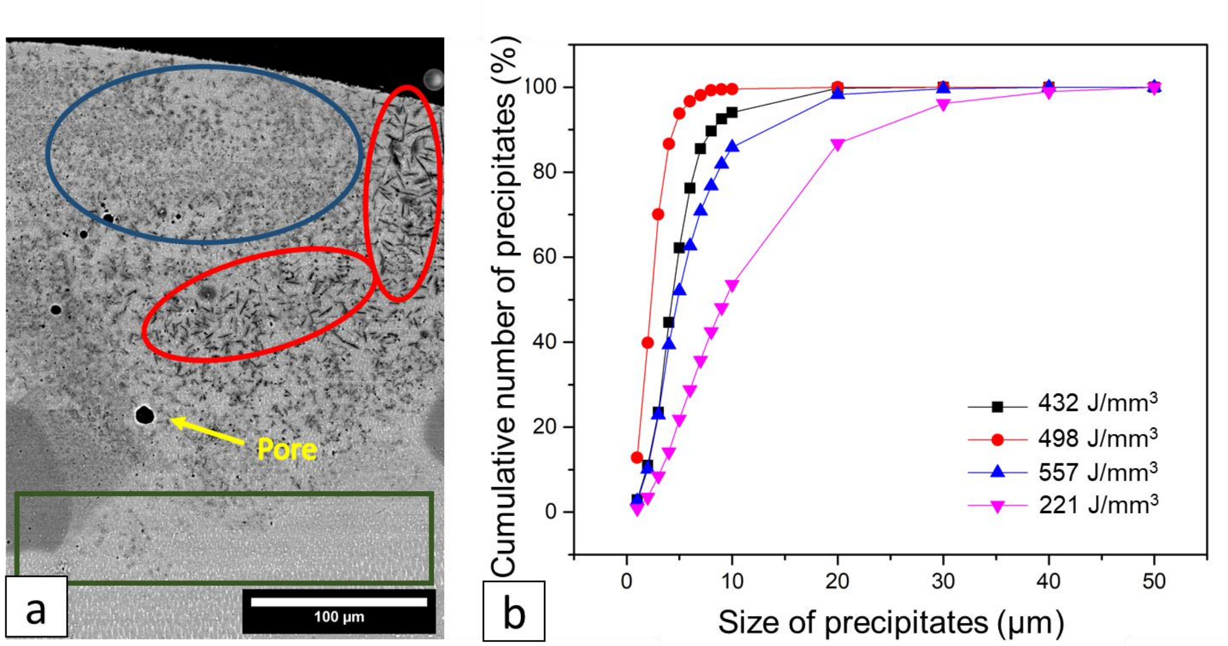

Figure 6.4. a) SEM micrograph of a single track made with AMC powder (deposited with 4.2 mm/s and 680 W). The distribution of the rod-shaped features is highlighted. The green frame highlights the heat-affected zone, the red frame highlights a region with larger rods, and the blue frame highlights a region with fine features. A pore is shown with a yellow arrow. b) the size distribution of the rod-shape features versus the cumulative number of the precipitates for AMC single tracks processed at the listed VED values. (AMC= aluminum matrix composites; VED= volumetric energy density).

TEM samples have been prepared to analyze the microstructure as well as the phase and elemental distribution of the single tracks. The TEM micrographs and the diffraction patterns from GA and AMC deposited samples are shown in Figure 6.5. The matrix of both GA and AMC based samples display Al diffraction patterns. Some precipitates and dislocations are observed in the GA samples (Figure 6.5. (a)). Fine precipitates and rod-shaped features are observed in the AMC samples (Figure 6.5 (b)). The diffraction pattern of the rod confirms the presence of B_4C. Additionally, a high density of dislocations is observed in the AMC samples, with the regions around the precipitates and rod-shaped features being particularly rich in dislocations. EDS analysis indicates that the fine precipitates in the AMC samples are rich in B and C with some segregation of Fe around the edges (Figure 6.6). The fine precipitates are noticeably deficient in Al. The rod-shaped features in the AMC-based single tracks are observed to have one of two different chemical compositions, as seen in the EDS maps in Figure 6.7. Some of the rod-shaped precipitates possess the expected B and C rich composition. However, other rod precipitates are rich in metals, primarily Cr, Mn, Mg, and Fe. The EDS analysis of the GA samples shows segregation in Fe, O, Co, Cu, and Mg (Figure 6.8).

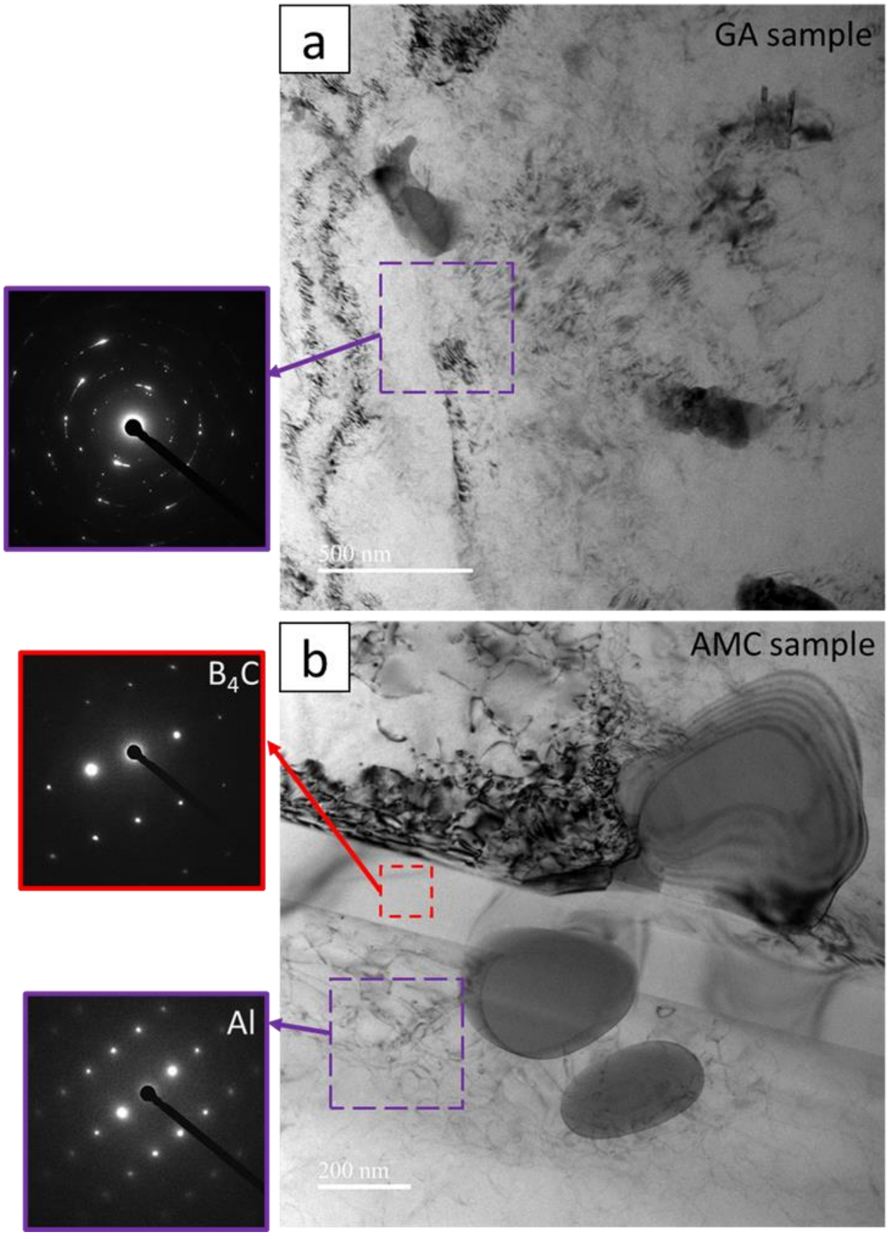

Figure 6.5. TEM micrographs of a) a GA single track sample with the diffraction pattern indicating polycrystalline Al. b) An AMC single track sample with the diffraction pattern of the rod-shaped precipitate indicating a B_4C structure. The diffraction pattern of the matrix displays the expected Al structure. (GA= gas atomized; AMC= aluminum matrix composites).

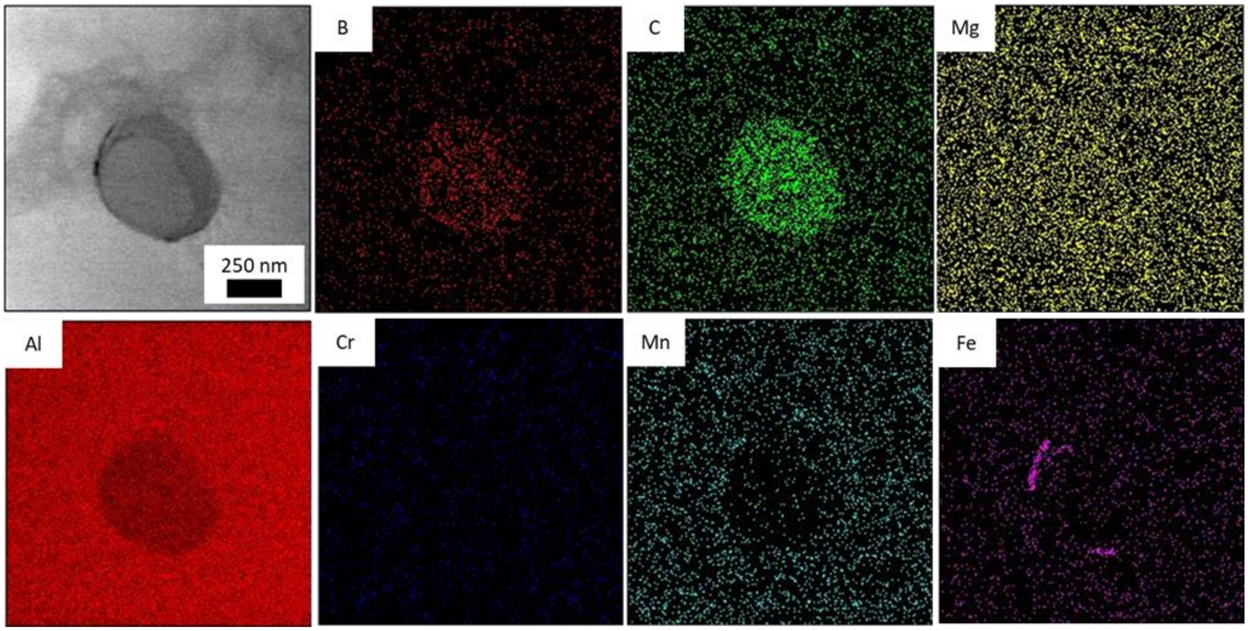

Figure 6.6. EDS elemental maps of a fine precipitate in an AMC single track sample. The precipitate is rich in B and C and depleted in Al. Some Fe segregation around the particle is observed. (AMC=aluminum matric composites).

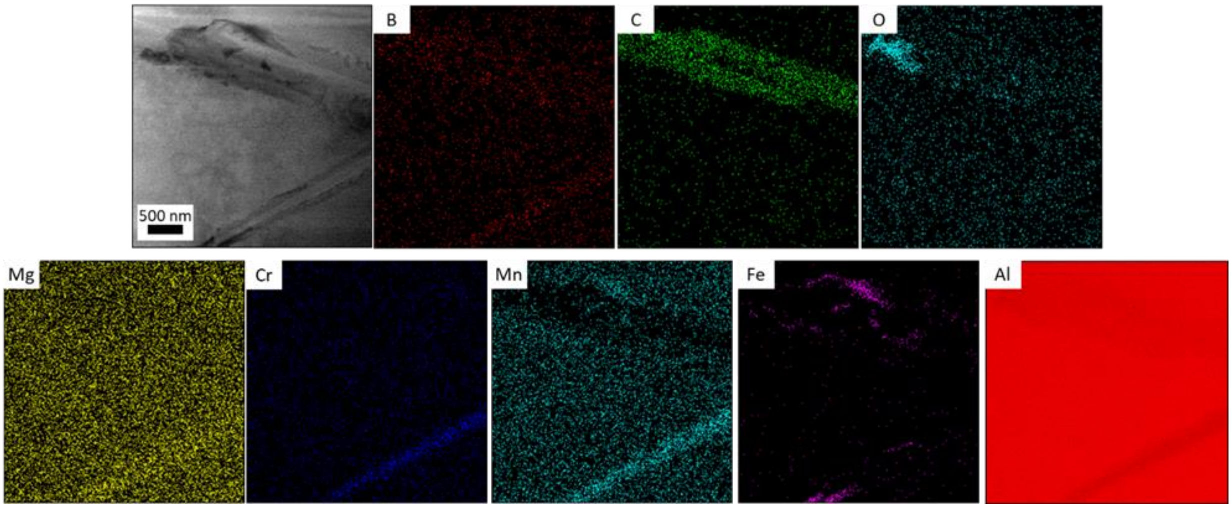

Figure 6.7. EDS elemental maps of some rod-shaped precipitates in an AMC single track sample. One rod is rich in B and C, while the other rod is rich in Mg, Cr, and Mn. Some segregation of Fe can be observed along the rods as well. (AMC=aluminum matric composites).

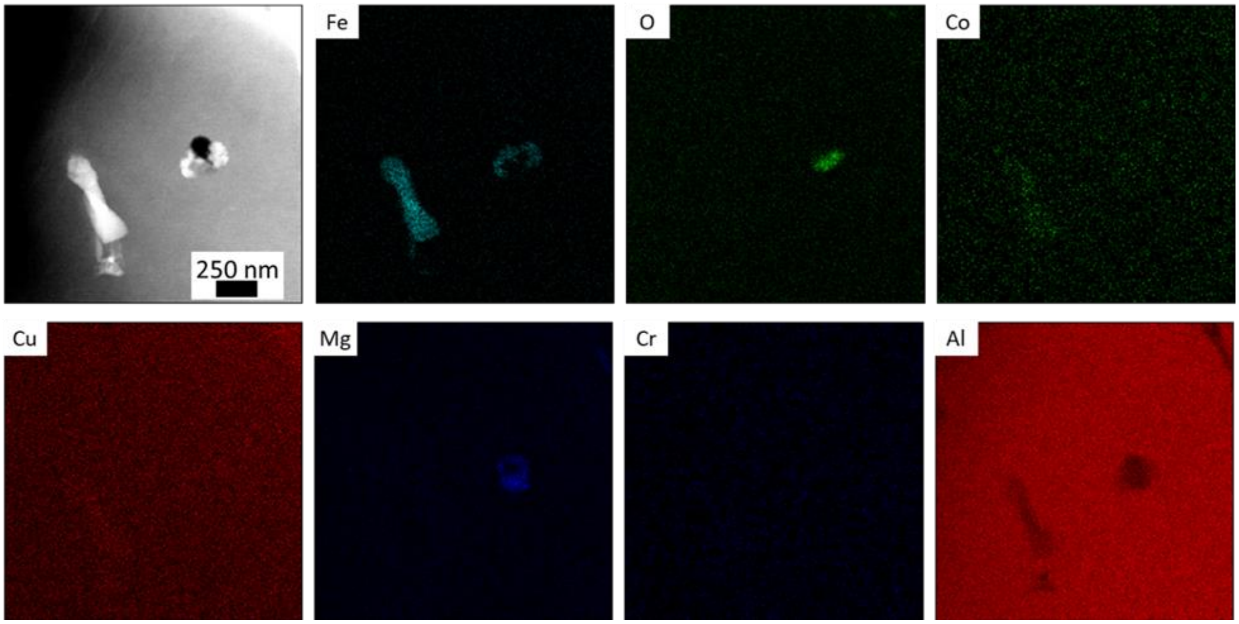

Figure 6.8. EDS elemental map of precipitates in a GA single track samples. Segregation of Fe, Co, Mg, and Cu is observed. (GA= gas atomized).

6.4. Discussion

Particle flowability is significantly influenced by particle shape and morphology, with highly flowability particles being most desirable for use in AM. For example, GA powder is widely used in AM due to its high flowability as a result of its spherical shape and narrow particle size distribution. However, the limitations in production of GA powders have stimulated studies on the flowability of non-spherical powders such as WA or milled powders. In Chapter 2, the relationship between the powder morphology and flowability was studied, finding that the morphology of WA particles lead to particles interlocking with each other and requiring more energy to initiate the flow [127]. Processing AMC powders involves incorporating two different powders with very different particle sizes and behavior. Hence, cryomilling was used to improve the distribution of B_4C in the Al matrix. Cryomilling leads to attachment and entrapment of the ceramic reinforcements into the matrix particles. However, as is shown in Figure 6.1 (b), the non-spherical morphology of the milled powder is different from the GA particles. Numerous studies have investigated using non-spherical particles such as WA powder in AM [155–157], finding that there are only minor differences between samples deposited with GA and WA powders. In addition, Fullenwider investigated using milled stainless steel powder in AM [25], revealing that there is no significant difference between single tracks deposited with milled and GA powders. Despite the differences in morphology in the current study, the XRD patterns of the GA and AMC powders are similar to each other except for the presence of B_4C peaks in the AMC powder. The similarity in the XRD patterns of the two powders indicates that cryomilling does not significantly impact the bulk phase state of the AMC powder.

The morphology and cross-sections of the GA and AMC single tracks presented in Figure 6.2 display several key similarities. Both sets of cross-sections are ovular or lenticular in shape with no signs of keyholing. Pores were also observed in both sets of single tracks. The pores in our samples are small and circular and are the result of evaporation of the different elements in the melt pool. However, the morphology of the AMC single tracks displays smoother surfaces than GA single tracks. Additionally, balling has been observed mostly in the samples made with GA powders. Balling is the formation of individual balls of material that have minimal wetting to the substrate or the rest of the track. The differences between the GA and AMC single tracks can be attributed to the differences in the powder characteristics such as morphology and size distribution. The change in the morphology of the particles can alter the flowability and compaction of the particles as well as the interaction between the particles and the laser. Scipioni Bertoli et al. investigated the laser absorption of WA and GA powders and showed that the laser absorption in WA powder is higher due to the irregular shape of the particles [38]. A reduced height in multi-layer wall builds has also been observed when WA powder is used during deposition instead of

GA powder [157]. Also, Mahmood et al. used swarf materials to deposit in laser directed energy deposition and found that the melt pool is hotter compared to deposition with GA powder [53].

Samples processed with the lowest VED values have the smoothest surfaces in both sets of samples. However, the height and dilution of the single tracks does not show a strong trend with VED, regardless of which powder is used for the deposit. There are numerous studies demonstrating the relationship between single track properties and VED. However, Scipioni Bertoli et al. showed that VED could not directly predict the properties of single tracks [100]. In addition, Kiani et al. showed that other metrics, such as linear energy densities could not determine the properties of the single tracks as well [137]. Other studies relate the height and dilution of the tracks to the cooling rate and melt pool temperature instead of VED. Work by Farshidianfar et al. showed that dilution exhibits a strong correlation with the cooling rate of the melt pool in single tracks, with higher dilution values indicating higher cooling rates [158]. The change in the dilution and height of our tracks can be explained better when considering the scan speed and laser power separately. In fact, the change in the height of the single tracks is attributed to change in the melt pool temperature, cooling rate, and available materials. Increasing the laser power while keeping the scan speed constant increases the melt pool temperature. Although the laser power and scan speed used to deposit both sets of single tracks are the same, the size and morphology of the single tracks show a different behavior between the AMC and GA samples. For example, the height of the GA single tracks is greater overall than the AMC tracks, except when the tracks are processed at 10.5 mm/s. Also, in GA samples the dilution is higher at the lower scan speed (Figure 6.3 (b)) compared to the dilution of the single track deposited with higher scan speed. The significant differences in single track morphology imply that there are differences in the melt pool temperature and behavior between GA and AMC samples.

Many factors can play a role in the formation of the different morphologies found in our single tracks. The difference in the size of the melt pool between GA and AMC can be due to presence of powders with different morphologies and ceramic reinforcements that can lead to a non-uniform temperature in the melt pool. The absorption of the laser by the particles of the matrix and the reinforcements is different and that can affect the local temperature of the melt pool leading to changes in the dynamics of the melt pool. Aversa et al. showed that in SLM of AlSi10Mg single tracks, the addition of 1 wt. % nano-TiB_2 can significantly influence the laser absorption of the powder and consequently the morphology of the single tracks [89]. As was mentioned earlier, the morphology of the cryomilled powder may also lead to increased absorption of the laser energy, leading to higher melt pool temperature during deposition. The ceramic reinforcements in our AMC powders will absorb more energy from the laser than the matrix, resulting in changes in the local temperature of the melt pool. Al reflects a significant amount of energy from the laser beam while B_4C will absorb a significant amount of energy. The amount of energy absorbed by different particles in the melt pool creates a temperature gradient that influences the fluid dynamics and surface tension in the melt pool. A Marangoni flow force will be generated due to the surface tension variation in the melt pool, and is normally influenced by the local temperature and the composition [159]. The difference in the local temperature created by presence of the different particle morphologies and the reinforcement particles in the matrix will affect the Marangoni flow in the melt pool. We therefore attribute the differences in the morphology of the GA and AMC single tracks to the non-uniform temperature and Maragoni flow effects in the melt pool.

A variety of different microstructural features are observed in the single tracks deposited with AMC powder (Figure 6.4). Figure 6.4 (b) shows that the size of the rod-shaped precipitates is influenced by the scan speed, with the rod-shaped features being larger in the samples with the highest scan speed. The highest scan speed in this study is also the sample with the lowest VED, while the other three samples are all deposited with the same scan speed and have similar VED values (431-557 J/mm^3). The behavior of the rod-shaped features is related to the scan speed, indicating that it is also related to the temperature of the melt pool and cooling rate. Other studies have shown that the higher scan speed usually results in higher cooling rate and lower melt pool temperature [160]. The difference in cooling rate and melt pool temperatures along with the difference in local temperature can be responsible for the formation of the larger rod-shaped particles. In addition, elevated temperatures can affect the morphology and the size of the B_4C particles. In this study, the rod size is also location specific, with different regions having different sized rod-shaped particles. In the melt pool, the temperature and the solidification path are also location dependent. The first nucleation in the melt pool usually happens on the existing grains of the substrate. The solidification continues as the melt pool cools down, with the top of the melt pool being the last part to solidify. The combination of the cooling rate and temperature gradient will determine the grain size and solidification structures. The heat-affected zone is the region farthest from the top of the melt pool and no rod-shaped features are observed in this region. Fine grains are usually observed at the top of the single tracks [8], where we also observe finer rod-shaped features in the AMC single tracks. Likewise, larger rod-shaped features are observed in areas that commonly exhibit larger grains in the melt pool. Similar behavior has been observed by Dai et al. who used SLM to process AlN/AlSi10Mg composites and found that the size and distribution of the reinforcements were correlated with the linear energy density (P/ϑ) [161]. In the same work, they showed that the presence of oxides in the melt pool could influence the direction of the Marangoni flow and reduce the surface tension in the melt pool.

There are several types of precipitates that are observed in heat-treated Al 5083 samples; including $MgAl_2$, Mg_2Si, Mg_2Al_3, $Cr_2Mg_3Al_{18}$, (Fe, Cr)$_3$SiAl$_{12}$, $MnAl_6$, $Al_{12}Mg_2$(CrMnFe), $CuMg_5Si_4Al_4$, and $Cu_2Mg_8Si_6Al_5$ [142]. Our EDS maps display Fe, Co, Mg, and Cu segregation in the GA samples (Figure 6.8), suggesting the formation of some precipitates. However, our GA single tracks were not heat treated and most of these precipitates would not be expected to form in the as-deposited single tracks. On the other hand, the EDS map in Figure 6.7 shows that the segregation of different elements, such as Mn, Mg, Fe, and Cr, in the AMC samples are larger and greater in number than in the GA samples. Some of these elements can be found in the Al 5083 powder itself. We also attribute the metal segregation to stainless steel contamination acquired by the AMC powder during the cryomilling process. During cryomilling, Al particles are impacted between stainless steel balls or against the sides of the stainless steel jar. Some amount of steel contamination is, therefore, expected during the milling process.

Although the melting temperature of B_4C is above 2700 °C, B_4C is known to be highly reactive with liquid Al [162]. Different intermetallic components can be formed between Al and B_4C, such as Al_4C_3, Al_2BC, AlB_{12}, Al_3BC, AlB_2 even at temperatures as low as 627 °C. B_4C, AlB_2, Al_3BC, and Al are also in thermodynamic equilibrium at room temperature. However, the short interaction time between the laser and powder makes AM an inherently metastable process, allowing for some equilibrium phases to be avoided. Scan speed and laser power will influence the cooling rate, the temperature gradient, and the peak temperature in the melt pool. In fact, the cooling rate and temperature gradient are location dependent, being different in different parts of the melt pool [163–165]. The variation of cooling rate and temperature gradient in the melt pool can result in the formation of different intermetallic components in the Al-B-C system being formed in different parts of the single track. EDS maps of the finer precipitates indicate that they are depleted of Al and rich in B and C, suggesting the presence of B_4C. The rod-shaped precipitates are mostly rich in B and C and depleted in Al; however, some of the rods are rich in other precipitates, as displayed in Figure 6.7. In addition, the diffraction patterns of the rod-shaped precipitates indicate that they possess a B_4C crystal structure. The location of the larger rod-shaped precipitates suggests that these precipitates form in lower cooling rate regions in the melt pool, whereas in the higher cooling rate regions, finer B_4C particles are more favorable. In order to fully understand the phases and chemical segregation observed in the single tracks deposited with AMC powder more work is need. The future work on this project can shed light on the mechanisms that were responsible for chemical segregations formation.

6.5. Conclusions

Adding ceramic reinforcements to an Al matrix can improve its mechanical properties. However, conventional processing and machining of aluminum matrix composites (AMCs) can be difficult. Instead, AM could be a viable method for producing AMC parts with complex geometries. In this study, Al-B_4C AMC powders were prepared using cryomilling. Single tracks of these AMC powders were deposited using a customized powder bed system. Single tracks using gas atomized (GA) powder were also deposited for comparison. The morphology and microstructure of the single tracks were investigated, and the following conclusions were drawn.

- Single tracks with Al 5083 AMC and GA powder were successfully deposited. Differences in the morphology, height of the single tracks, and dilution occur due to the variation in the morphology of the AMC and GA powders and the presence of the B_4C particles in the AMC powder. Besides the morphological differences, few pores were observed in the cross-sections of the single tracks.

- Rod-shaped features were observed in the single tracks processed with AMC powder. The size of these features is related to the volumetric energy density (VED) used in the processing of the single tracks, with lower VED values resulting in larger features. Variation in the size of these features was observed in every single track. This variation can be due to the different local temperatures and cooling rates in the single tracks.
- The GA and AMC single track samples exhibit different precipitates with unique chemistries and morphologies. In general, precipitates in AMC samples are divided into two categories: 1) precipitates rich in B and C, and 2) precipitates rich in Cr, Mn, and Mg. The diffraction patterns confirmed the presence of B_4C in some of the precipitates. The second category of the precipitates are from intermetallic components that form as a result of the degradation of B_4C in Al, as well as contamination from the cryomilling process.

Chapter 7: Conclusions and Suggestions for Future Work

7.1. Summary and conclusions

Additive manufacturing (AM) of metallic alloys has been explored in many scientific studies, typically with a focus on understanding how to tailor the microstructure and mechanical properties for specific applications. Powder bed fusion (PBF) and laser directed energy deposition (L-DED) are both established methods in the AM industry. These methods use a high energy laser to melt the powder particles in a layer-by-layer manner. Although the effort has been made to understand the relationship between the processing parameters in AM (PBF and L-DED) and part properties, there is a critical knowledge gap related to how the properties of the starting feedstock powder influence the final part properties. Gas atomized (GA) powder is one of the most used and investigated feedstocks in AM. The spherical morphology and particle size distribution of GA powders are believed to contribute to the quality of the parts. However, the relationship between the powder characteristics and the flow has not been extensively investigated. Chapter 2 of this dissertation focused on exploring the relationship between metal powder characteristics, such as morphology and particle size, with the flowability. Six different powders with different size ranges, morphologies, and chemical compositions were investigated using three different powder flowability testing systems. The results showed that different characteristics, such as average particle diameter or the aspect ratio, will play a significant role in various aspects of powder flowability. The results in Chapter 2 illustrate that although particles can be produced through the same process, they might show very different flowability behavior. In addition, the results indicated that the particle morphology plays an essential role in the initiation of flow from a static condition. In contrast, the particle size is critical in how well the flow is maintained after initiation.

Gas atomization powder synthesis can be an expensive process, therefore, leading to considerable research into finding viable alternative powder feedstock sources for AM. Chapter 3 focused on the preparation of novel feedstock powders for AM to reduce the cost of powder production and introducing new methods to recycle Al waste. For this study, waste materials were collected from other AM facilities and then processed using planetary ball milling and cryomilling to produce a powder with a size and shape suitable for AM. In the planetary ball milling experiment, larger size balls were shown to increase the impact of the particles and to be more effective in the size reduction process. Also, continuing ball milling for an extended amount of time resulted in high yield (particles in the desired size) and semi-spherical shaped particles. In the cryomilling process, the increased ball-to-powder ratio and using cryogenic liquid were effectively used to reduce the milling duration. The results demonstrated that high yield was achieved using larger size balls and a lower amount of process control agent.

Chapter 4 focused on processing one of the most popular Al alloys (AlSi10Mg) in AM using L-DED. Single tracks are typically used as an indicator of bulk deposition; their properties are normally considered translatable to the bulk deposition. However, depositing AlSi10Mg in the L-DED system demonstrated that the single tracks are not scalable to bulk deposition. The results indicated that the properties of single tracks and bulk samples deposited with similar processing parameters are significantly different, meaning that optimal single track deposition parameters will not always yield viable bulk parts. It was found that successful thin wall deposition parameters are a better indicator of block sample’s properties than single tracks. From this investigation, a processing map was developed for the deposition of the single tracks and thin walls using L-DED systems. Fully dense blocks were successfully deposited using the processing parameter map developed based on thin wall deposition. In addition, the mechanical properties of the blocks showed a minimal change in the strength and hardness along the build direction, indicating that the parameters that were adopted from thin wall deposition led to uniform properties in the blocks.

The powder capture efficiency of the AM systems is very low, which results in the production of a high amount of waste. A significantly large portion of powder used to deposit in AM is not going to fuse and form the final parts and requires further processing to be reused in AM. In addition, powder reuse may influence the powder properties and the quality of the final parts. Chapter 5 focused on understanding the influence of powder reuse on the powder characteristics and the properties of the final AM parts properties. AlSi10Mg powder was reused for four cycles, and the mechanical properties of the bulk samples and morphological features of the powders were investigated. The results indicated that as the powder is being reused, the average particle size increases and the particle size distribution narrows. However, the flowability of the powder does not significantly change with powder reuse. The mechanical properties of the samples deposited in different cycles exhibited minimal changes as well.

The most common Al alloys used in AM inherently have lower strength compared to high-strength Al alloys. Ceramic reinforcements can be added to Al alloys to improve their mechanical properties. In Chapter 6, we used aluminum matrix composite powders to deposit single tracks in AM. The aluminum matrix composites are produced by cryomilling Al 5083 powder with B_4C particles for 8 hours. The effect of processing parameters on the morphology and geometry of the single tracks indicated that gas atomized powder without ceramic additions showed slight variations in track height and flatness compared to single tracks deposited with B_4C particles embedded in the starting material. The microstructure, especially the chemical segregation and secondary phase formation, was also different in the single tracks deposited with GA powder compared those made with aluminum metal matrix composite powder.

7.2. Future work

Portions of the work presented in this dissertation are part of ongoing projects. For example, the investigation on the use of alternative feedstock in additive manufacturing presented in Chapter 3 is not yet complete. The future effort on this project will include the production of enough powder to be used in the LENS® system to print parts and to understand the effect of powder preparation methods on the flowrate of the powder and the final properties of the parts. As mentioned in Chapter 2, the particle morphology and size influence the powder flow, and consequently, the properties of the part. In addition, some studies have shown that powders with fine particle sizes will react differently in the melt pool and may serve as a nucleation point to form finer grains in the printed parts. The microstructure analysis of the parts can show the differences in the grain size and cell structure of the AlSi10Mg parts printed using waste materials. Understanding the role of processing parameters in tailoring the properties of the powders is essential as well. Although the chemical composition of the milled powder and GA powder is the same, the morphology of the particles may affect their interaction with the laser. In addition to the morphology, the surface chemistry of the powder particles can change their behavior in the melt pool. Different techniques such as X-ray photoelectron spectroscopy and TEM can be used to investigate the surface chemistry of powders produced by milling and their impact on the microstructure. High-speed photography could be used to investigate how powders with various morphologies interact with the laser in the melt pool.

Although the feasibility of printing single tracks using aluminum matrix composites is investigated in Chapter 6, the impact of the ceramic reinforcements on the mechanical properties and microstructure of the builds has not been extensively investigated. Ceramic reinforcements alter the dynamics of the melt pool, which can change the microstructure and properties of the parts printed using AM. In addition, the amount of these additives and their composition can significantly affect the part properties. Future work on the aluminum matrix composites project includes the deposition of blocks with different amounts of B_4C reinforcements in order to understand the effect these reinforcements have on the microstructure and mechanical properties of the parts. In addition, B_4C and other ceramic reinforcements tend to agglomerate in the melt pool, leading to inhomogeneity in the melt pool that may affect the properties significantly. Different microscopy techniques, such as SEM and TEM, can be used to investigate the distribution of the ceramic reinforcements and identify the intermetallic phases that form during deposition.

Efforts have been made to improve the mechanical properties of additively manufactured aluminum alloys parts. These efforts mostly include tailoring the processing parameters or addition of different elements to modify the microstructure. However, the Al alloys that were used in most of these studies were selected based on conventional manufacturing processes. ThermoCalc and CALPHAD can be employed to design a set of Al alloys specifically for additive manufacturing. Atomization facilities at UC Irvine provide a unique opportunity to prepare customized gas atomized powder that then could be used in AM. High resolution microscopy such as TEM can be used to confirm the formation of the desired phases. Mechanical testing and microstructure analysis could be used to validate whether the higher strength compared to more conventional Al powder has been achieved.

REFERENCES

[1] P.C. Priarone, G. Ingarao, R. di Lorenzo, L. Settineri, Influence of material-related aspects of additive and subtractive Ti-6Al-4V manufacturing on energy demand and carbon dioxide emissions, J. Ind. Ecol. 21 (2017) S191–S202.

[2] C. Blain, Additive Manufacturing Can Reduce Part Counts Significantly, DesignNews. (2018). https://www.designnews.com/automation-motion-control/additive-manufacturing-can-reduce-part-counts-significantly/32852757559475 (accessed September 6, 2020).

[3] W.J. Sames, F.A. List, S. Pannala, R.R. Dehoff, S.S. Babu, F.A. List, S. Pannala, R.R. Dehoff, S.S.B. The, W.J. Sames, F.A. List, S. Pannala, R.R. Dehoff, S.S. Babu, The metallurgy and processing science of metal additive manufacturing The metallurgy and processing science of metal additive manufacturing, 6608 (2016). https://doi.org/10.1080/09506608.2015.1116649.

[4] T.D. Ngo, A. Kashani, G. Imbalzano, K.T.Q. Nguyen, D. Hui, Additive manufacturing (3D printing): A review of materials, methods, applications and challenges, Compos. Part B Eng. 143 (2018) 172–196.

[5] L. Dowling, J. Kennedy, S. O'Shaughnessy, D. Trimble, A review of critical repeatability and reproducibility issues in powder bed fusion, Mater. Des. 186 (2020) 108346.

[6] N.T. Aboulkhair, N.M. Everitt, I. Ashcroft, C. Tuck, Reducing porosity in AlSi10Mg parts processed by selective laser melting, Addit. Manuf. 1 (2014) 77–86. https://doi.org/10.1016/j.addma.2014.08.001.

[7] A. Mauduit, S. Pillot, H. Gransac, Study of the suitability of aluminum alloys for additive manufacturing by laser powder bed fusion, UPB Sci. Bull. Ser. B. 79 (2017) 219–238.

[8] T. DebRoy, H.L. Wei, J.S. Zuback, T. Mukherjee, J.W. Elmer, J.O. Milewski, A.M. Beese, A. Wilson-Heid, A. De, W. Zhang, Additive manufacturing of metallic components–process, structure and properties, Prog. Mater. Sci. 92 (2017) 112–224.

[9] ASTM international. F3318-18 Standard for Additive Manufacturing- Finished Part Properties - Specification for AlSi10Mg with Powder Bed Fusion- Laser Beam, (n.d.). https://doi.org/https://doi.org/10.1520/F3318-18.

[10] J. Fiocchi, A. Tuissi, P. Bassani, C.A. Biffi, Low temperature annealing dedicated to AlSi10Mg selective laser melting products, J. Alloys Compd. 695 (2017) 3402–3409.

[11] S. Nafisi, D. Emadi, R. Ghomashchi, Impact of Mg addition on solidification behaviour of Al–7% Si alloy, Mater. Sci. Technol. 24 (2008) 718–724.

[12] W. Pei, W. Zhengying, C. Zhen, D. Jun, H. Yuyang, L. Junfeng, Z. Yatong, P. Wei, Z. Wei, Z. Chen, J. Du, Y. He, J. Li, Y. Zhou, The AlSi10Mg samples produced by selective laser melting: single track, densification, microstructure and mechanical behavior, Appl. Surf. Sci. 408 (2017) 38–50. https://doi.org/10.1016/j.apsusc.2017.02.215.

[13] M. Brandt, Laser additive manufacturing: materials, design, technologies, and applications, Woodhead Publishing, 2016.

[14] B. Wu, C. Myant, S. Weider, The value of additive manufacturing: future opportunities, Imp. Coll. London, Brief. Pap. (2017).

[15] T. McCue, Significant 3D Printing Forecast Surges To $35.6 Billion, Forbes. (2019). https://www.forbes.com/sites/tjmccue/2019/03/27/wohlers-report-2019-forecasts-35-6-billion-in-3d-printing-industry-growth-by-2024/#6cfcd4747d8a.

[16] B. Hapuwatte, K.D. Seevers, F. Badurdeen, I.S. Jawahir, Total life cycle sustainability analysis of additively manufactured products, Procedia CIRP. 48 (2016) 376–381.

[17] Y. Luo, Z. Ji, M.C. Leu, R. Caudill, Environmental performance analysis of solid freedom fabrication processes, in: Proc. 1999 IEEE Int. Symp. Electron. Environ. (Cat. No. 99CH36357), IEEE, 1999: pp. 1–6.

[18] S. Yang, T. Talekar, M.A. Sulthan, Y.F. Zhao, A generic sustainability assessment model towards consolidated parts fabricated by additive manufacturing process, Procedia Manuf. 10 (2017) 831–844.

[19] P. Markillie, A Third Industrial Revolution, Econ. (2013).

[20] K. Ma, T. Smith, E.J. Lavernia, J.M. Schoenung, Environmental Sustainability of Laser Metal Deposition: The Role of Feedstock Powder and Feedstock Utilization Factor, Procedia Manuf. 7 (2017) 198–204. https://doi.org/10.1016/j.promfg.2016.12.049.

[21] K. Kellens, R. Mertens, D. Paraskevas, W. Dewulf, J.R. Duflou, Environmental Impact of Additive Manufacturing Processes: Does AM contribute to a more sustainable way of part manufacturing?, Procedia CIRP. 61 (2017) 582–587.

[22] T. Peng, K. Kellens, R. Tang, C. Chen, G. Chen, Sustainability of additive manufacturing: An overview on its energy demand and environmental impact, Addit. Manuf. 21 (2018) 694–704.

[23] I.E. Anderson, E.M.H. White, R. Dehoff, Feedstock powder processing research needs for additive manufacturing development, Curr. Opin. Solid State Mater. Sci. 22 (2018) 8–15.

[24] I. Gibson, D. Rosen, B. Stucker, Directed energy deposition processes, in: Addit. Manuf. Technol., Springer, 2015: pp. 245–268.

[25] B. Fullenwider, P. Kiani, J.M. Schoenung, K. Ma, Two-stage ball milling of recycled machining chips to create an alternative feedstock powder for metal additive manufacturing, Powder Technol. 342 (2018) 562–571.

[26] D. Hackett, H. Kopech, Atomization advances in thermal spray powder, Adv. Mater. Process. 159 (2001) 31–34.

[27] P. Sun, Z.Z. Fang, Y. Zhang, Y. Xia, Review of the methods for production of spherical Ti and Ti alloy powder, Jom. 69 (2017) 1853–1860.

[28] S. Hoeges, A. Zwiren, C. Schade, Additive manufacturing using water atomized steel powders, Met. Powder Rep. 00 (2017) 1–7. https://doi.org/http://dx.doi.org/10.1016/j.mprp.2017.01.004.

[29] G. Chen, S.Y. Zhao, P. Tan, J. Wang, C.S. Xiang, H.P. Tang, A comparative study of Ti-

6Al-4V powders for additive manufacturing by gas atomization, plasma rotating electrode process and plasma atomization, Powder Technol. 333 (2018) 38–46.

[30] P. Baláž, High-energy milling, in: Mechanochemistry Nanosci. Miner. Eng., Springer, 2008: pp. 103–132.

[31] E.J. Lavernia, B.Q. Han, J.M. Schoenung, Cryomilled nanostructured materials: Processing and properties, Mater. Sci. Eng. A. 493 (2008) 207–214.

[32] N. Serres, D. Tidu, S. Sankare, F. Hlawka, Environmental comparison of MESO-CLAD?? process and conventional machining implementing life cycle assessment, J. Clean. Prod. 19 (2011) 1117–1124. https://doi.org/10.1016/j.jclepro.2010.12.010.

[33] M.A. Jackson, J.D. Morrow, D.J. Thoma, F.E. Pfefferkorn, A comparison of 316 L stainless steel parts manufactured by directed energy deposition using gas-atomized and mechanically-generated feedstock, CIRP Ann. (2020).

[34] T. Durejko, J. Aniszewska, M. Ziętala, A. Antolak-Dudka, T. Czujko, R.A. Varin, V. Paserin, The application of globular water-atomized iron powders for additive manufacturing by a LENS technique, Materials (Basel). 11 (2018) 843.

[35] S.K. Everton, M. Hirsch, P. Stravroulakis, R.K. Leach, A.T. Clare, Review of in-situ process monitoring and in-situ metrology for metal additive manufacturing, Mater. Des. 95 (2016) 431–445.

[36] S. Singh, S. Ramakrishna, R. Singh, Material issues in additive manufacturing: A review, J. Manuf. Process. 25 (2017) 185–200.

[37] H.P. Tang, M. Qian, N. Liu, X.Z. Zhang, G.Y. Yang, J. Wang, Effect of Powder Reuse Times on Additive Manufacturing of Ti-6Al-4V by Selective Electron Beam Melting, Jom. 67 (2015) 555–563. https://doi.org/10.1007/s11837-015-1300-4.

[38] U.S. Bertoli, G. Guss, S. Wu, M.J. Matthews, J.M. Schoenung, In-situ characterization of laser-powder interaction and cooling rates through high-speed imaging of powder bed fusion additive manufacturing, Mater. Des. 135 (2017) 385–396.

[39] V. Seyda, D. Herzog, C. Emmelmann, Relationship between powder characteristics and part properties in laser beam melting of Ti–6Al–4V, and implications on quality, J. Laser Appl. 29 (2017) 22311.

[40] D.F. Susan, J.D. Puskar, J.A. Brooks, C.V. Robino, Quantitative characterization of porosity in stainless steel LENS powders and deposits, Mater. Charact. 57 (2006) 36–43.

[41] Standard Test Methods for Determining Loose and Tapped Bulk Densities of Powders using a Graduated Cylinder, (18AD).

[42] J. Clayton, D. Millington-Smith, B. Armstrong, The application of powder rheology in additive manufacturing, Jom. 67 (2015) 544–548.

[43] K.L. Terrassa, B.E. MacDonald, J.C. Haley, J.M. Schoenung, Reuse of Powder Feedstock for Directed Energy Deposition, Powder Technol. (2018).

[44] M.F. McGuire, Stainless steels for design engineers, Asm International, 2008.

[45] M. Javidani, J. Arreguin-Zavala, J. Danovitch, Y. Tian, M. Brochu, Additive Manufacturing of AlSi10Mg Alloy Using Direct Energy Deposition: Microstructure and Hardness Characterization, J. Therm. Spray Technol. 26 (2017) 587–597. https://doi.org/10.1007/s11666-016-0495-4.

[46] M. Dihydrate, Freeman Technology, (2014) 1–2. https://www.freemantech.co.uk/ (accessed September 7, 2019).

[47] Mercury Scientific Inc., (n.d.). http://www.mercuryscientific.com (accessed September 7, 2019).

[48] G. Forte, P.J. Clark, Z. Yan, E.H. Stitt, M. Marigo, Using a Freeman FT4 rheometer and Electrical Capacitance Tomography to assess powder blending, Powder Technol. 337 (2018) 25–35.

[49] T. Wei, V. Simko, R package ‘corrplot’: visualization of a correlation matrix (version 0.84).’, R Found. Stat. Comput. Vienna. Https//Github. Com/Taiyun/Corrplot. (2017).

[50] J.E. Funk, D.R. Dinger, Predictive process control of crowded particulate suspensions: applied to ceramic manufacturing, Kluwer Academic, Boston, 1994.

[51] C. Meier, R. Weissbach, J. Weinberg, W.A. Wall, A.J. Hart, Critical influences of particle size and adhesion on the powder layer uniformity in metal additive manufacturing, J. Mater. Process. Technol. 266 (2019) 484–501.

[52] N. Vlachos, I.T.H. Chang, Investigation of flow properties of metal powders from narrow particle size distribution to polydisperse mixtures through an improved Hall-flowmeter, Powder Technol. 205 (2011) 71–80.

[53] K. Mahmood, W.U.H. Syed, A.J. Pinkerton, Innovative reconsolidation of carbon steel machining swarf by laser metal deposition, Opt. Lasers Eng. 49 (2011) 240–247.

[54] J.I. Chang, J.J. Lin, J.S. Huang, Y.M. Chang, Recycling oil and steel from grinding swarf, Resour. Conserv. Recycl. 49 (2006) 191–201.

[55] J. Gronostajski, H. Marciniak, A. Matuszak, New methods of aluminium and aluminium-alloy chips recycling, J. Mater. Process. Technol. 106 (2000) 34–39.

[56] B. Wan, W. Chen, T. Lu, F. Liu, Z. Jiang, M. Mao, Review of solid state recycling of aluminum chips, Resour. Conserv. Recycl. 125 (2017) 37–47.

[57] J.B.M. Moungomo, D. Nganga-Kouya, V. Songmene, J. Kouam, J.P. Kenné, J.P. Kenn??, Machinability study of recycled aluminum cans and machining chips, Int. J. Adv. Manuf. Technol. 87 (2016) 2551–2566. https://doi.org/10.1007/s00170-016-8564-x.

[58] A. Canakci, T. Varol, A novel method for the production of metal powders without conventional atomization process, J. Clean. Prod. 99 (2015) 312–319. https://doi.org/10.1016/j.jclepro.2015.02.090.

[59] K. Mahmood, A. Khan, A. Pinkerton, Laser metal deposition of steel components using machining waste as build material, 2011 Conf. Lasers Electro-Optics Laser Sci. to Photonic Appl. CLEO 2011. (2011) 3–4.

[60] S. Ghods, E. Schultz, C. Wisdom, R. Schur, R. Pahuja, A. Montelione, D. Arola, M. Ramulu, Electron beam additive manufacturing of Ti6Al4V: Evolution of powder morphology and part microstructure with powder reuse, Materialia. 9 (2020) 100631.

[61] F. Calignano, Design optimization of supports for overhanging structures in aluminum and titanium alloys by selective laser melting, Mater. Des. 64 (2014) 203–213.

[62] Y.F. Fuziana, A.R.M. Warikh, M.A. Lajis, M.A. Azam, N.S. Muhammad, Recycling aluminium (Al 6061) chip through powder metallurgy route, Mater. Res. Innov. 18 (2014) S6-354.

[63] B. Fullenwider, P. Kiani, J.M. Schoenung, K. Ma, From Recycled Machining Waste to Useful Powders for Metal Additive Manufacturing, in: REWAS 2019, Springer, 2019: pp. 3–7.

[64] N. Bay, Mechanisms producing metallic bonds in cold welding., Weld. J. 62 (1983) 137.

[65] Y.F. Zhang, L. Lu, S.M. Yap, Prediction of the amount of PCA for mechanical milling, J. Mater. Process. Technol. 89 (1999) 260–265.

[66] Morf3D Aerospace, (n.d.). http://morf3d.com/ (accessed May 8, 2020).

[67] Q. Han, R. Setchi, S.L. Evans, Characterisation and milling time optimisation of nanocrystalline aluminium powder for selective laser melting, Int. J. Adv. Manuf. Technol. 88 (2017) 1429–1438.

[68] H. Yang, Reinforcement Size Effect in Cryomilled Aluminum Boron Carbide Metal Matrix Composites, University of California, Davis, 2015.

[69] H. Shin, S. Lee, H.S. Jung, J.-B. Kim, Effect of ball size and powder loading on the milling efficiency of a laboratory-scale wet ball mill, Ceram. Int. 39 (2013) 8963–8968.

[70] H.M. de Lira, P.R. Rodriguez, O.O. de Araujo Filho, C.H. Gonzalez, Nanostructured Al Powder Obtained by High Energy Ball Milling at Ambient and Cryogenic Temperatures, in: Mater. Sci. Forum, Trans Tech Publ, 2014: pp. 125–129.

[71] C. Badiola, M. Schoenitz, X. Zhu, E.L. Dreizin, Nanocomposite thermite powders prepared by cryomilling, J. Alloys Compd. 488 (2009) 386–391.

[72] J. He, E.J. Lavernia, Development of nanocrystalline structure during cryomilling, J. Mater. Res. 16 (2001).

[73] F. Sun, P. Rojas, A. Zúñiga, E.J. Lavernia, Nanostructure in a Ti alloy processed using a cryomilling technique, Mater. Sci. Eng. A. 430 (2006) 90–97.

[74] X. Wang, L. Jiang, D. Zhang, I.J. Beyerlein, S. Mahajan, T.J. Rupert, E.J. Lavernia, J.M. Schoenung, Reversed compressive yield anisotropy in magnesium with microlaminated structure, Acta Mater. 146 (2018) 12–24.

[75] J. Ye, J. He, J.M. Schoenung, Cryomilling for the fabrication of a particulate B 4 C reinforced Al nanocomposite: Part I. Effects of process conditions on structure, Metall. Mater. Trans. A. 37 (2006) 3099–3109.

[76] T.R. Smith, J.D. Sugar, J.M. Schoenung, C. San Marchi, Anomalous Annealing Response of Directed Energy Deposited Type 304L Austenitic Stainless Steel, JOM. (2018) 1–6.

[77] Y. Zhai, H. Galarraga, D.A. Lados, Microstructure, static properties, and fatigue crack growth mechanisms in Ti-6Al-4V fabricated by additive manufacturing: LENS and EBM, Eng. Fail. Anal. 69 (2016) 3–14.

[78] G.P. Dinda, A.K. Dasgupta, J. Mazumder, Evolution of microstructure in laser deposited Al–11.28% Si alloy, Surf. Coatings Technol. 206 (2012) 2152–2160.

[79] N.A. Kistler, A.R. Nassar, E.W. Reutzel, D.J. Corbin, A.M. Beese, Effect of directed energy deposition processing parameters on laser deposited Inconel® 718: Microstructure, fusion zone morphology, and hardness, J. Laser Appl. 29 (2017) 22005.

[80] X.P. Li, X.J. Wang, M. Saunders, A. Suvorova, L.C. Zhang, Y.J. Liu, M.H. Fang, Z.H. Huang, T.B. Sercombe, A selective laser melting and solution heat treatment refined Al–12Si alloy with a controllable ultrafine eutectic microstructure and 25% tensile ductility, Acta Mater. 95 (2015) 74–82.

[81] N.T. Aboulkhair, I. Maskery, C. Tuck, I. Ashcroft, N.M. Everitt, The microstructure and mechanical properties of selectively laser melted AlSi10Mg: The effect of a conventional T6-like heat treatment, Mater. Sci. Eng. A. 667 (2016) 139–146. https://doi.org/10.1016/j.msea.2016.04.092.

[82] N.T. Aboulkhair, I. Maskery, C. Tuck, I. Ashcroft, N.M. Everitt, On the formation of AlSi10Mg single tracks and layers in selective laser melting: Microstructure and nano-mechanical properties, J. Mater. Process. Technol. 230 (2016) 88–98.

[83] K. Kempen, L. Thijs, J. Van Humbeeck, J.-P.J.-P. Kruth, Mechanical Properties of AlSi10Mg Produced by Selective Laser Melting, Phys. Procedia. 39 (2012) 439–446. https://doi.org/10.1016/j.phpro.2012.10.059.

[84] Y. Ding, M. Trask, S. Chou, A. Walker, M. Brochu, J.A. Muñiz-Lerma, M. Trask, S. Chou, A. Walker, M. Brochu, Microstructure and mechanical property considerations in additive manufacturing of aluminum alloys, MRS Bull. 41 (2016) 745–751. https://doi.org/10.1557/mrs.2016.214.

[85] I. Yadroitsev, A. Gusarov, I. Yadroitsava, I. Smurov, Single track formation in selective laser melting of metal powders, J. Mater. Process. Technol. 210 (2010) 1624–1631.

[86] K. Kempen, L. Thijs, J. Van Humbeeck, J.-P.J.-P. Kruth, Processing AlSi10Mg by selective laser melting: parameter optimisation and material characterisation, Mater. Sci. Technol. 31 (2015) 917–923. https://doi.org/10.1179/1743284714Y.0000000702.

[87] Y. Huang, M.B. Khamesee, E. Toyserkani, A new physics-based model for laser directed energy deposition (powder-fed additive manufacturing): From single-track to multi-track and multi-layer, Opt. Laser Technol. 109 (2019) 584–599.

[88] M. Tang, P.C. Pistorius, S. Narra, J.L. Beuth, Rapid solidification: selective laser melting of AlSi10Mg, JOM. 68 (2016) 960–966. https://doi.org/10.1007/s11837-015-1763-3.

[89] A. Aversa, M. Moshiri, E. Librera, M. Hadi, G. Marchese, D. Manfredi, M. Lorusso, F.

Calignano, S. Biamino, M. Lombardi, Single scan track analyses on aluminium based powders, J. Mater. Process. Technol. 255 (2018) 17–25.

[90] W. Li, S. Li, J. Liu, A. Zhang, Y. Zhou, Q. Wei, C. Yan, Y. Shi, Effect of heat treatment on AlSi10Mg alloy fabricated by selective laser melting: Microstructure evolution, mechanical properties and fracture mechanism, Mater. Sci. Eng. A. 663 (2016) 116–125. https://doi.org/10.1016/j.msea.2016.03.088.

[91] X. Wang, L. Li, J. Qu, W. Tao, Microstructure and mechanical properties of laser metal deposited AlSi10Mg alloys, Mater. Sci. Technol. 35 (2019) 2284–2293.

[92] N. Ramesh, Structure-Process-Property Relationships for LENS® and SLM Processed AlSi10Mg Alloys and the Effect of Heat Treatment, UC Irvine, 2018. https://escholarship.org/uc/item/8s14j0sn.

[93] ASTM International, Standard Test Methods for Density of Compacted or Sintered Powder Metallurgy (PM) Products Using Archimedes' Principle, Astm B962-13. i (2013) 1–7. https://doi.org/10.1520/B0962-13.2.

[94] D. Da Buchbinder, H.B. Schleifenbaum, S. Heidrich, W. Meiners, J. Bültmann, High power Selective Laser Melting (HP SLM) of aluminum parts, Phys. Procedia. 12 (2011) 271–278. https://doi.org/10.1016/j.phpro.2011.03.035.

[95] B. Chen, Y. Yao, X. Song, C. Tan, L. Cao, J. Feng, Microstructure and mechanical properties of additive manufacturing AlSi10Mg alloy using direct metal deposition, Ferroelectrics. 523 (2018) 153–166.

[96] Y. Gao, J. Zhao, Y. Zhao, Z. Wang, H. Song, M. Gao, Effect of processing parameters on solidification defects behavior of laser deposited AlSi10Mg alloy, Vacuum. 167 (2019) 471–478.

[97] F. Lv, L. Shen, H. Liang, D. Xie, C. Wang, Z. Tian, Mechanical properties of AlSi10Mg alloy fabricated by laser melting deposition and improvements via heat treatment, Optik (Stuttg). 179 (2019) 8–18.

[98] E. Louvis, P. Fox, C.J. Sutcliffe, Selective laser melting of aluminium components, J. Mater. Process. Technol. 211 (2011) 275–284.

[99] A. Khajepour, E. Toyserkani, S. Corbin, Laser cladding, (2004).

[100] U.S. Bertoli, A.J. Wolfer, M.J. Matthews, J.-P.R. Delplanque, J.M. Schoenung, On the limitations of volumetric energy density as a design parameter for selective laser melting, Mater. Des. 113 (2017) 331–340.

[101] U. De Oliveira, V. Ocelik, J.T.M. De Hosson, Analysis of coaxial laser cladding processing conditions, Surf. Coatings Technol. 197 (2005) 127–136.

[102] J.C. Haley, J.M. Schoenung, E.J. Lavernia, Observations of particle-melt pool impact events in directed energy deposition, Addit. Manuf. 22 (2018) 368–374.

[103] S.A. Khairallah, A. Anderson, Mesoscopic simulation model of selective laser melting of stainless steel powder, J. Mater. Process. Technol. 214 (2014) 2627–2636.

[104] D. Bourell, J.P. Kruth, M. Leu, G. Levy, D. Rosen, A.M. Beese, A. Clare, Materials for additive manufacturing, CIRP Ann. 66 (2017) 659–681.

[105] B. Zheng, Y. Zhou, J.E. Smugeresky, J.M. Schoenung, E.J. Lavernia, Thermal behavior and microstructural evolution during laser deposition with laser-engineered net shaping: Part I. Numerical calculations, Metall. Mater. Trans. A. 39 (2008) 2228–2236.

[106] D. Marla, U. V Bhandarkar, S.S. Joshi, Models for predicting temperature dependence of material properties of aluminum, J. Phys. D. Appl. Phys. 47 (2014) 105306.

[107] G. Ran, J.E. Zhou, Q.G. Wang, Precipitates and tensile fracture mechanism in a sand cast A356 aluminum alloy, J. Mater. Process. Technol. 207 (2008) 46–52.

[108] B. Suárez-Peña, J. Asensio-Lozano, Microstructure and mechanical property developments in Al–12Si gravity die castings after Ti and/or Sr additions, Mater. Charact. 57 (2006) 218–226. https://doi.org/10.1016/j.matchar.2006.01.015.

[109] F. Trevisan, F. Calignano, M. Lorusso, J. Pakkanen, A. Aversa, E.P. Ambrosio, M. Lombardi, P. Fino, D. Manfredi, On the Selective Laser Melting (SLM) of the AlSi10Mg Alloy: Process, Microstructure, and Mechanical Properties, Materials (Basel). 10 (2017) 76.

[110] K. V Yang, P. Rometsch, T. Jarvis, J. Rao, S. Cao, C. Davies, X. Wu, Porosity formation mechanisms and fatigue response in Al-Si-Mg alloys made by selective laser melting, Mater. Sci. Eng. A. 712 (2018) 166–174.

[111] K.G. Prashanth, S. Scudino, J. Eckert, Defining the tensile properties of Al-12Si parts produced by selective laser melting, Acta Mater. 126 (2017) 25–35.

[112] D.D. Gu, W. Meiners, K. Wissenbach, R. Poprawe, Laser additive manufacturing of metallic components: materials, processes and mechanisms, Int. Mater. Rev. 57 (2012) 133–164.

[113] A. Singh, A. Ramakrishnan, D. Baker, A. Biswas, G.P. Dinda, Laser metal deposition of nickel coated Al 7050 alloy, J. Alloys Compd. 719 (2017) 151–158.

[114] J.H. Martin, B.D. Yahata, J.M. Hundley, J.A. Mayer, T.A. Schaedler, T.M. Pollock, 3D printing of high-strength aluminium alloys, Nature. 549 (2017) 365. https://doi.org/10.1038/nature23894.

[115] W.H. Kan, Y. Nadot, M. Foley, L. Ridosz, G. Proust, J.M. Cairney, Factors that affect the properties of additively-manufactured AlSi10Mg: Porosity versus microstructure, Addit. Manuf. 29 (2019) 100805.

[116] P. Kiani, A.D. Dupuy, K. Ma, J.M. Schoenung, J.M.S. Parnian Kiani, Alexander D. Dupuy, Kaka Ma, Directed energy deposition of AlSi10Mg: Single track nonscalability and bulk properties, Mater. Des. (2020) 108847. https://doi.org/10.1016/j.matdes.2020.108847.

[117] R. Sreenivasan, A. Goel, D.L. Bourell, Sustainability issues in laser-based additive manufacturing, Phys. Procedia. 5 (2010) 81–90. https://doi.org/10.1016/j.phpro.2010.08.124.

[118] M. Baumers, C. Tuck, R. Hague, I. Ashcroft, R. Wildman, A comparative study of metallic additive manufacturing power consumption, in: Solid Free. Fabr. Symp., 2010: pp. 278–288.

[119] F. Le Bourhis, O. Kerbrat, J.-Y. Hascoet, P. Mognol, F. Le Bourhis, O. Kerbrat, J.-Y. Hascoet, P. Mognol, F. Le, B. Olivier, J.H.P. Mognol, F. Le Bourhis, O. Kerbrat, J.-Y. Hascoet, P. Mognol, Sustainable manufacturing: evaluation and modeling of environmental impacts in additive manufacturing., Int. J. Adv. Manuf. Technol. 69 (2013) 1927–1939. https://doi.org/10.1007/s00170-013-5151-2.

[120] C. Katinas, W. Shang, Y.C. Shin, J. Chen, Modeling particle spray and capture efficiency for direct laser deposition using a four nozzle powder injection system, J. Manuf. Sci. Eng. 140 (2018).

[121] J.A. Slotwinski, E.J. Garboczi, P.E. Stutzman, C.F. Ferraris, S.S. Watson, M.A. Peltz, Characterization of metal powders used for additive manufacturing, J. Res. Natl. Inst. Stand. Technol. 119 (2014) 460.

[122] L. Cordova, M. Campos, T. Tinga, Revealing the effects of powder reuse for selective laser melting by powder characterization, Jom. 71 (2019) 1062–1072.

[123] H. Asgari, C. Baxter, K. Hosseinkhani, M. Mohammadi, On microstructure and mechanical properties of additively manufactured AlSi10Mg_200C using recycled powder, Mater. Sci. Eng. A. 707 (2017) 148–158.

[124] F. Del Re, V. Contaldi, A. Astarita, B. Palumbo, A. Squillace, P. Corrado, P. Di Petta, Statistical approach for assessing the effect of powder reuse on the final quality of AlSi10Mg parts produced by laser powder bed fusion additive manufacturing, Int. J. Adv. Manuf. Technol. 97 (2018) 2231–2240.

[125] A.H. Maamoun, M. Elbestawi, G.K. Dosbaeva, S.C. Veldhuis, Thermal post-processing of AlSi10Mg parts produced by Selective Laser Melting using recycled powder, Addit. Manuf. 21 (2018) 234–247.

[126] U. Tradowsky, J. White, R.M. Ward, N. Read, W. Reimers, M.M. Attallah, Selective laser melting of AlSi10Mg: Influence of post-processing on the microstructural and tensile properties development, Mater. Des. 105 (2016) 212–222.

[127] P. Kiani, U. Scipioni Bertoli, A.D. Dupuy, K. Ma, J.M. Schoenung, A Statistical Analysis of Powder Flowability in Metal Additive Manufacturing, Adv. Eng. Mater. (n.d.). https://doi.org/10.1002/adem.202000022.

[128] E. Santecchia, S. Spigarelli, M. Cabibbo, Material Reuse in Laser Powder Bed Fusion: Side Effects of the Laser—Metal Powder Interaction, Metals (Basel). 10 (2020) 341.

[129] J.C. Haley, B. Zheng, U.S. Bertoli, A.D. Dupuy, J.M. Schoenung, E.J. Lavernia, Working distance passive stability in laser directed energy deposition additive manufacturing, Mater. Des. 161 (2019) 86–94.

[130] Z. Luo, Y. Zhao, A survey of finite element analysis of temperature and thermal stress fields in powder bed fusion additive manufacturing, Addit. Manuf. 21 (2018) 318–332.

[131] S.J. Wolff, H. Wu, N. Parab, C. Zhao, K.F. Ehmann, T. Sun, J. Cao, In-situ high-speed X-ray imaging of piezo-driven directed energy deposition additive manufacturing, Sci. Rep. 9 (2019) 1–14.

[132] Y.C. Shin, N. Bailey, C. Katinas, W. Tan, Predictive modeling capabilities from incident powder and laser to mechanical properties for laser directed energy deposition, Comput. Mech. 61 (2018) 617–636.

[133] A.T. Sutton, C.S. Kriewall, M.C. Leu, J.W. Newkirk, Powder characterisation techniques and effects of powder characteristics on part properties in powder-bed fusion processes, Virtual Phys. Prototyp. 12 (2017) 3–29.

[134] B. Sartin, T. Pond, B. Griffith, W. Everhart, L. Elder, E. Wenski, C. Cook, D. Wieliczka, W. King, A. Rubenchik, 316L powder reuse for metal additive manufacturing, in: Proc. 28th Annu. Int. Solid Free. Fabr. Symp., 2017: pp. 351–364.

[135] V. Seyda, N. Kaufmann, C. Emmelmann, Investigation of aging processes of Ti-6Al-4 V powder material in laser melting, Phys. Procedia. 39 (2012) 425–431. https://doi.org/10.1016/j.phpro.2012.10.057.

[136] A. du Plessis, I. Yadroitsava, I. Yadroitsev, Effects of defects on mechanical properties in metal additive manufacturing: A review focusing on X-ray tomography insights, Mater. Des. 187 (2020) 108385.

[137] J.M.S. Parnian Kiani, Alexander D. Dupuy, Kaka Ma, Directed energy deposition of AlSi10Mg: Single track nonscalability and bulk properties, (n.d.).

[138] N. Guo, M.C. Leu, Additive manufacturing: technology, applications and research needs, Front. Mech. Eng. 8 (2013) 215–243.

[139] N. Kaufmann, M. Imran, T.M. Wischeropp, C. Emmelmann, S. Siddique, F. Walther, Influence of process parameters on the quality of aluminium alloy EN AW 7075 using selective laser melting (SLM), Phys. Procedia. 83 (2016) 918–926.

[140] D. Svetlizky, B. Zheng, T. Buta, Y. Zhou, O. Golan, U. Breiman, R. Haj-Ali, J.M. Schoenung, E.J. Lavernia, N. Eliaz, Directed energy deposition of Al 5xxx alloy using Laser Engineered Net Shaping (LENS®), Mater. Des. (2020) 108763.

[141] L. Jiang, H. Wen, H. Yang, T. Hu, T. Topping, D. Zhang, E.J. Lavernia, J.M. Schoenung, Influence of length-scales on spatial distribution and interfacial characteristics of B4C in a nanostructured Al matrix, Acta Mater. 89 (2015) 327–343.

[142] G. Lucadamo, N.Y.C. Yang, C. San Marchi, E.J. Lavernia, Microstructure characterization in cryomilled Al 5083, Mater. Sci. Eng. A. 430 (2006) 230–241.

[143] A. Aversa, G. Marchese, M. Lorusso, F. Calignano, S. Biamino, E.P. Ambrosio, D. Manfredi, P. Fino, M. Lombardi, M. Pavese, Microstructural and mechanical characterization of aluminum matrix composites produced by laser powder bed fusion, Adv. Eng. Mater. 19 (2017) 1700180.

[144] Q. Han, R. Setchi, F. Lacan, D. Gu, S.L. Evans, Selective laser melting of advanced Al-Al2O3 nanocomposites: Simulation, microstructure and mechanical properties, Mater. Sci.

Eng. A. 698 (2017) 162–173.

[145] O. Torabi, R. Ebrahimi-Kahrizsangi, Synthesis of B4C, Al2O3, and AlB12 reinforced Al matrix nano composites via mechanochemical method, J. Compos. Mater. 46 (2012) 2227–2237.

[146] K. Kalaiselvan, N. Murugan, S. Parameswaran, Production and characterization of AA6061–B4C stir cast composite, Mater. Des. 32 (2011) 4004–4009.

[147] I. Topcu, H.O. Gulsoy, N. Kadioglu, A.N. Gulluoglu, Processing and mechanical properties of B4C reinforced Al matrix composites, J. Alloys Compd. 482 (2009) 516–521.

[148] F. Tang, X. Wu, S. Ge, J. Ye, H. Zhu, M. Hagiwara, J.M. Schoenung, Dry sliding friction and wear properties of B4C particulate-reinforced Al-5083 matrix composites, Wear. 264 (2008) 555–561.

[149] L. Zhang, Z. Wang, Q. Li, J. Wu, G. Shi, F. Qi, X. Zhou, Microtopography and mechanical properties of vacuum hot pressing Al/B4C composites, Ceram. Int. 44 (2018) 3048–3055.

[150] A.P. Newbery, S.R. Nutt, E.J. Lavernia, Multi-scale Al 5083 for military vehicles with improved performance, Jom. 58 (2006) 56–61.

[151] J. Ye, B.Q. Han, Z. Lee, B. Ahn, S.R. Nutt, J.M. Schoenung, A tri-modal aluminum based composite with super-high strength, Scr. Mater. 53 (2005) 481–486.

[152] M. Ghayoor, S.B. Badwe, H. Irrinki, S. V Atre, S. Pasebani, Water Atomized 17-4 PH Stainless Steel Powder as a Cheaper Alternative Powder Feedstock for Selective Laser Melting, in: Mater. Sci. Forum, Trans Tech Publ, 2018: pp. 698–703.

[153] H. Yang, L. Jiang, M. Balog, P. Krizik, J.M. Schoenung, Reinforcement size dependence of load bearing capacity in ultrafine-grained metal matrix composites, Metall. Mater. Trans. A. 48 (2017) 4385–4392.

[154] J. Ciurana, L. Hernandez, J. Delgado, Energy density analysis on single tracks formed by selective laser melting with CoCrMo powder material, Int. J. Adv. Manuf. Technol. 68 (2013) 1103–1110.

[155] R. Li, Y. Shi, Z. Wang, L. Wang, J. Liu, W. Jiang, Densification behavior of gas and water atomized 316L stainless steel powder during selective laser melting, Appl. Surf. Sci. 256 (2010) 4350–4356. https://doi.org/10.1016/j.apsusc.2010.02.030.

[156] M.J. Tobar, J.M. Amado, J. Montero, A. Yáñez, A Study on the Effects of the Use of Gas or Water Atomized AISI 316L Steel Powder on the Corrosion Resistance of Laser Deposited Material, Phys. Procedia. 83 (2016) 606–612. https://doi.org/10.1016/j.phpro.2016.08.063.

[157] A.J. Pinkerton, L. Li, Direct additive laser manufacturing using gas-and water-atomised H13 tool steel powders, Int. J. Adv. Manuf. Technol. 25 (2005) 471–479. https://doi.org/10.1007/s00170-003-1844-2.

[158] M.H. Farshidianfar, A. Khajepour, A.P. Gerlich, Effect of real-time cooling rate on microstructure in laser additive manufacturing, J. Mater. Process. Technol. 231 (2016) 468–478.

[159] T. Mukherjee, H.L. Wei, A. De, T. DebRoy, Heat and fluid flow in additive manufacturing—Part I: Modeling of powder bed fusion, Comput. Mater. Sci. 150 (2018) 304–313.

[160] Y. Li, D. Gu, Parametric analysis of thermal behavior during selective laser melting additive manufacturing of aluminum alloy powder, Mater. Des. 63 (2014) 856–867. https://doi.org/10.1016/j.matdes.2014.07.006.

[161] D. Dai, D. Gu, Influence of thermodynamics within molten pool on migration and distribution state of reinforcement during selective laser melting of AlN/AlSi10Mg composites, Int. J. Mach. Tools Manuf. 100 (2016) 14–24.

[162] Z. Zhang, K. Fortin, A. Charette, X.-G. Chen, Effect of titanium on microstructure and fluidity of Al–B 4 C composites, J. Mater. Sci. 46 (2011) 3176–3185.

[163] T. Mukherjee, H.L. Wei, A. De, T. DebRoy, Heat and fluid flow in additive manufacturing–Part II: Powder bed fusion of stainless steel, and titanium, nickel and aluminum base alloys, Comput. Mater. Sci. 150 (2018) 369–380.

[164] H.L. Wei, J.W. Elmer, T. DebRoy, Origin of grain orientation during solidification of an aluminum alloy, Acta Mater. 115 (2016) 123–131.

[165] H.L. Wei, J.W. Elmer, T. DebRoy, Three-dimensional modeling of grain structure evolution during welding of an aluminum alloy, Acta Mater. 126 (2017) 413–425.